12-2-2019

Impact of Mixer Design on Lean Direct Injection Combustion

Xiao Ren
University of Connecticut - Storrs, xiao.ren@uconn.edu

Recommended Citation

Ren, Xiao, "Impact of Mixer Design on Lean Direct Injection Combustion" (2019). *Doctoral Dissertations*. 2376.
https://opencommons.uconn.edu/dissertations/2376

Impact of Mixer Design on Lean Direct Injection Combustion

Xiao Ren, PhD

University of Connecticut, 2019

In an effort to reduce the environmental impact of aviation, lean-dome combustion concepts such as lean direct injection (LDI) are being pursued for their potential to achieve very low emissions. However, low-emissions potentials may be accompanied by operability challenges. LDI combustion utilizes multi-point mixers to achieve both low NOx emissions and satisfactory combustion stability. Since the performance of LDI directly depends on the design parameters of each single LDI mixer, a series of fundamental investigations into lean-dome-relevant pilot combustor devices are conducted herein. A single LDI mixer typically uses swirlers with converging venturi and diverging flare to generate swirling flows, which facilitate fuel and air mixing in the combustor dome. This dissertation aims to investigate the impact of LDI mixer design parameters, including swirler vane angle, flare, and relative swirling direction between the inner and outer swirlers, on single-mixer LDI combustion under varying test conditions. The flow fields, flame structures and responses, radical distributions, emissions, and lean blowout (LBO) limits of methane-fueled LDI combustion are investigated with varying mixer design parameters. Experimentally, a test system of single-mixer LDI combustion has been designed and built to investigate different mixer designs via advanced optical diagnostics, including particle image velocimetry, broadband flame imaging, chemiluminescence imaging, and OH-planar laser induced florescence, to obtain high fidelity data of flow/flame fields, emissions, and operability. Compared against experimental data, the best practices of meshing and turbulence and combustion modeling have been established for Computational Fluid Dynamics (CFD) simulations of LDI. Reasonable agreement between experimental and CFD result has been achieved for flow characteristics and flame structure/response/dynamics. Based on the present results, larger swirler vane angle lowers the LBO limits but produces higher NOx levels. Removing flare reduces NOx emissions at a cost of worsening operability. Counter-swirling forms a stronger shear layer than the co-swirling case. Furthermore, these results are discussed to identify possible research directions for optimizing LDI designs for reduced NOx emissions while maintaining or improving operability relative to current rich-dome combustion technology.

Impact of Mixer Design on Lean Direct Injection Combustion

Xiao Ren

B.Eng., Beihang University, Beijing, China, 2013

A Dissertation
Submitted in Partial Fulfillment of the
Requirements for the Degree of
Doctor of Philosophy
at the
University of Connecticut

2019

APPROVAL PAGE

Doctor of Philosophy Dissertation

Impact of Mixer Design on Lean Direct Injection Combustion

Presented by

Xiao Ren, B. Eng.

Major Advisor ____

Chih-Jen Sung

Associate Advisor ____

Baki M. Cetegen

Associate Advisor ____

Xinyu Zhao

Associate Advisor ____

Bryan W. Weber

Associate Advisor ____

Francesco Carbone

University of Connecticut
2019

Acknowledgements

This thesis is a summary of my research over the past six years. It’s not an easy task to complete and I couldn’t have accomplished so much without the help of many generous people. Therefore, I would like to acknowledge all of them for being supportive and helpful with my work and my life.

To begin with, I would like to my advisor, Dr. Chih-Jen Sung, for his constant support, insightful guidance and incredible patience with my research. And I would also like to thank him for sharing his extensive knowledge and passionate attitude for combustion research with me. Without his encouragement, I could not make such progress.

Next, I would like to acknowledge and thank my committee members, Profs. Baki Cetegen, Xinyu Zhao, Bryan Weber, and Francesco Carbone for their support with my Ph.D. research. I appreciate their suggestions on my proposed study, which have helped me polish my thesis and make it a much better story.

Then I would like to thank our collaborator, Dr. Hukam Mongia, for his invaluable input and advice on gas turbine combustion.

Moreover, I would like to thank all my lab colleagues, both past and present, Dr. Xin Hui, Dr. Kyle Brady, Dr. Xin Xue, Dr. Goutham Kukkadapu, Dr. Pradeep Singh, Dr. Nick Curtis, Dr. Ossama Mannaa, Justin Bunnell, Kyle Twarog, Mengyuan Wang, Ruozhou Fang, Peter Vannorsdall, and Bhushan Patil. It has been a great journey to meet and work with them.

Additionally, I would like to thank all my friends and colleagues from UCONN ME department and from Multi-Physics Computation Group of Argonne National Laboratory. Particularly, I would like to thank Drs. Sibendu Som, Prithwish Kundu and Chao Xu for giving me the opportunity to conduct an internship at ANL for half a year and sharing a lot of CFD experience with me. Besides, I gratefully acknowledge the computing resources provided on Bebop and Blues, high-performance computing clusters, operated by the Laboratory Computing Resource Center at Argonne National Laboratory.

In the end, I would like to thank my parents for always supporting me and believing in me so far for 29 years, and a special thank you goes to my girlfriend Xiao Liang for accompanying with me during my hardest time.

Table of Contents

List of Figures

List of Tables

List of Abbreviations

Airblast	airblast type mixer
AMR	adaptive mesh refinement
a.u.	arbitrary unit
CAEP	Committee on Aviation Environmental Protection
CCW	counter-clockwise
CFL	Courant-Friedrichs-Lewy
CNRZ	corner recirculation zone
CRZ	center recirculation zone
CW	clockwise
$EINO_x$	emission index of nitrogen oxides
FFT	fast Fourier transform
FGM	Flamelet Generated Manifold
FWHM	full width at half maximum
IAS	inner air swirler
ICAO	International Civil Aeronautics Organization
ISL	inner shear layer
LBO	lean blowout
LDI	lean direct injection
LES	Large Eddy Simulation
LOS	line-of-sight
LPP	lean premixed prevaporized
LTO	landing and take-off
MPI	message passing interface
NO_x	nitrogen oxides
OAS	outer air swirler
OEM	Original Engine Manufacturer
OPR	overall pressure ratio
PLIF	planar laser induced fluorescence
PM	particulate matter
PISO	Pressure Implicit with Splitting of Operators
RANS	Reynolds-Averaged Navier-Stokes

RKE	realizable k-epsilon
RMS	root-mean-square
SGS	sub-grid scale
SMD	Sauter mean diameter
STD	standard deviation
SV-LDI	swirl-venturi LDI
TET	turbine entry temperature
TR-PIV	time-resolved particle image velocimetry
UHC	unburned hydrocarbons

List of Symbols

A_e	effective area
A_t	geometric area of venturi throat
D_f	diameter of flare exit
D_t	diameter of venturi throat
k	turbulent kinetic energy
$\dot{m}$	mass flow rate
ϕ	overall equivalence ratio
Re	Reynolds number
R_h	radii of swirler’s inner boundary
R_n	radii of swirler’s outer boundary
SN	swirl number
θ	swirler vane angle
t_{res}	residence time
U	mean axial velocity
V	mean radial velocity
U_t	mean axial velocity magnitude at venturi throat
x	axial axis
y	radial axis
x_{vc}	length of venturi
x_f	length of flare
ρ	air density
Δ_n	grid size of the n^{th} level of mesh refinement with respect to the base grid size Δ_0
ΔP	pressure drop across burner

CHAPTER 1 INTRODUCTION

1.1 Background

Air travel has become one of the major transportation methods. The fast growth of travel demands, particularly in the developing nations worldwide, lead to higher air travel demand in the coming decades [1]. The convenience of air travel, at the same time, also causes concerns to human health and environment from the aircraft gas turbine combustion (GTC) pollutants, i.e. CO, CO_2, unburned hydrocarbons (UHC), particulate matters (PM), nitrogen oxides (NO_x, comprising NO and NO_2), etc. CO and CO_2 are important factors of global warming. UHC and PM worsen ground level air quality, which induces serious health issues especially on the lung [2]. NO_x is one of the major causes of photochemical fog and destroys ozone [3]. The ozone layer protects the ecosystem by shielding the ultraviolet radiations [4]. At lower altitudes, NO_x is part of the reaction chain that results in smog and acid rain [5]. The environmental issues resulted from these emissions have caused a lot of troubles globally. Reducing the emission levels is one of the major research directions for aircraft GTC.

The goal of reducing emission levels of CO, CO_2, UHC, and PM can be accomplished by increasing combustion efficiency and reducing specific fuel consumption, which typically requires operating at high pressure ratios thus leading to high combustor inlet temperatures and peak operating temperatures [6]. While this approach improves the cycle efficiency, the higher inlet pressures and temperatures further elevate peak operating temperatures, leading to increased production of thermal NO_x. Committee on Aviation Environmental Protection (CAEP) has conducted a comprehensive prediction of future emission trends, which indicates that global aircraft NO_x emissions below 3000 feet will increase from 0.25 million metric tons (Mt) in 2006, as the baseline, to between 0.52 million Mt and 0.72 million Mt in 2036 [7]. Therefore, much attention has been paid to regulate NO_x emissions.

The International Civil Aeronautics Organization (ICAO) has established a series of emissions regulations since 1986, which cover the take-off, climb, descent, and taxiing/ground idle phases of the engine operation, the so-called landing and take-off (LTO) cycle [8]. As the influence of NO_x emissions becomes more severe, the subsequent ICAO meetings adopted more stringent standards for NO_x regulations, i.e. CAEP/2 in 1993, CAEP/4 in 1999, CAEP/6 in 2005, and CAEP/8 in 2011. Using CAEP/6 as reference, the LTO NO_x reduction goals for mid-term and long-term are stated by ICAO [9]: 45% reduction of CAEP/6 for 2016 and 60% reduction of CAEP/6 for 2026, respectively. These more and more stringent regulations drive the industry to develop low emission GTC technologies for aero-engines, which at the same time are required to meet other stringent design requirements, such as combustion efficiency and operability limits.

Several low emission combustion strategies for modern aero-engines have been developed to mitigate the production of NO_x while maintaining the high temperatures required to reduce other emissions. These strategies fall into two broad categories: lean-front-end (lean dome) and rich-front-end (rich dome) combustors. Lean-front-end combustors operate fuel lean throughout the combustor. By lowering peak flame temperature, lean dome devices can potentially offer lower NO_x emissions than rich dome combustors. One major lean dome combustion technology is the Lean Premix Prevaporize (LPP) concept [10–14]. LPP is designed to supply the combustion zone with a well-premixed fuel and air mixture, and combust at a low equivalence ratio close to the lean blowout (LBO) limit. To achieve the goals of low emissions, usually LPP combustor consists of three main regions [15]. The first region is for the preparation of homogenous lean fuel-air mixture, where fuel injects, vaporizes, and mixes with air. The premixing and pre-vaporization region is one of the design challenges for LPP that the long preparation time for fuel vaporization and fuel-air mixing might cause auto-ignition when mixing at high inlet air temperatures and pressures. The second region is the part for lean combustion that is usually stabilized by recirculation zone and produces very low NO_x. Then, in the third region, air dilutes the combustion products. For LPP combustors, the NO_x reduces as the overall equivalence ratio drops closer to lean blowout (LBO). LPP has the potential to produce low NO_x emissions.

Rich-front-end combustors include the widely used rich burn-quick quench-lean burn (RQL) strategy [16–18]. As conceptually depicted in Figure 1-1, RQL uses a rich-burning zone to initiate the combustion, a quick quench by air directed around the main fuel/air mixers to oxidize CO, hydrogen and hydrocarbon intermediates, and a final lean-burn zone to simultaneously minimize NO_x and smoke emissions. The technology applications of RQL includes TALON family (TALON I, II, and X) from Pratt & Whitney (PW), and Trent 1000 from Rolls-Royce (RR). It is reported that for main Original Engine Manufacturers (OEMs) the recent in-service RQL combustors produce similar NO_x results in terms of emission index of NO_x ($EINO_x$) over various operational pressure ratios (OPRs) [19], which is feasible for CAEP/6 standard. Due to the rich combustion zone, RQL has inherently satisfactory ignition and lean blowout performance. The wide operational range in additional to good emission performance makes RQL advantageous, since the requirements of safety, relight capability, operability etc. are considered as high priorities in GTC [2].

Although these two technologies have thus far been sufficient to reduce NO_x emissions [20], as the ICAO emissions standards – via CAEP limits – become increasingly stringent, at the aforementioned higher operating pressures and temperatures RQL and LPP concepts have faced a number of challenges. For instance, LPP concepts have been found to be prone to auto-ignition

[20], instability [21–23], and flashback [24] problems at high pressure and temperature conditions, limiting their operational range. Controlling smoke/soot emissions and avoiding near-stoichiometric conditions can be difficult in RQL concept combustors; the latter issue is particularly so when balanced with the need for optimized dome cooling [2]. RQL combustor has multiple combustion sections, which would lead to more complex aircraft design given the required length and weight restrictions [25].

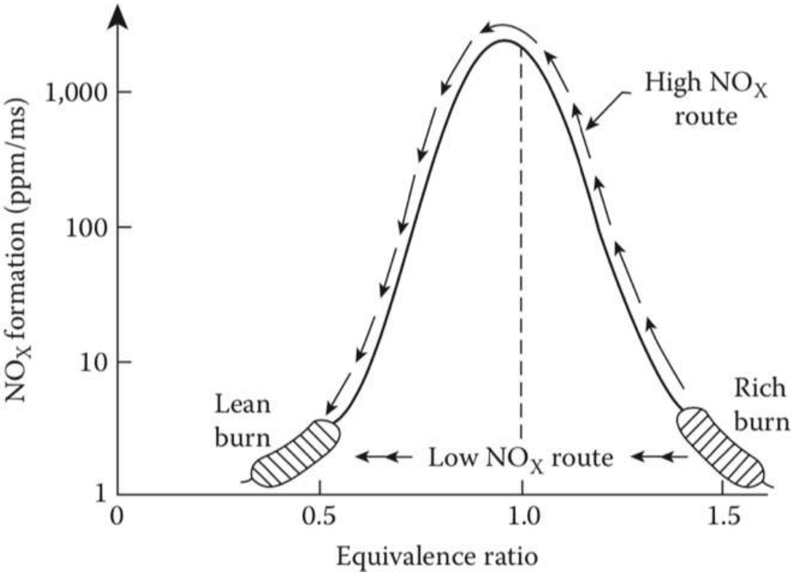

Figure 1-1. Schematics of RQL working principle and NO_x formation routes [15].

Recently, the Lean Direct Injection (LDI) combustion concept was proposed [26] to achieve low NO_x emissions as well as good combustion operability without the need for separate premixing chamber, thereby mitigating limitations found with LPP-based designs while maintaining an overall fuel-lean architecture. In the LDI combustion, air and liquid fuel are injected and mixed inside the combustor, which is likely to be more compact and lighter than LPP. Since the LDI relies on vaporization of the fuel followed by rapid mixing with the air, regions of locally higher equivalence ratio are possible when using a conventional single mixer to mix large amount of air and fuel, leading to local hot spots and high production of NO_x. In order to obtain sufficiently mixing conditions without premixing chamber, a major branch of LDI concepts utilized multipoint fuel-injection, multi-burning zone method, as shown in Figure 1-2, to obtain uniformly lean-mixer combustion and low NO_x formation.

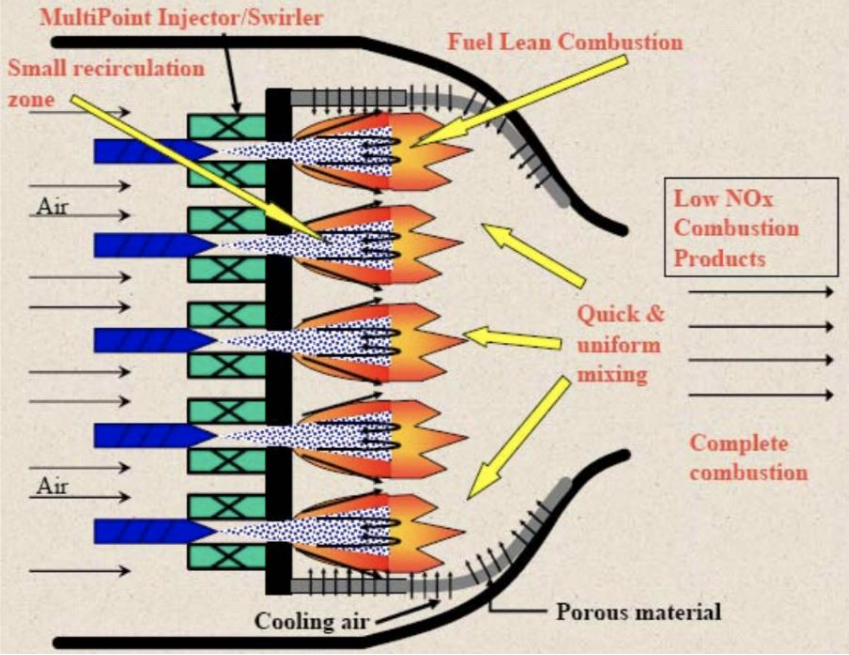

Figure 1-2. Multipoint fuel-injection, multi-burning zone LDI combustor [27].

Since then, LDI with small, multi-point, independently-fueled swirl injectors arranged in various patterns has been widely studied, as it facilitates tailoring the specific design for emissions reduction throughout the flight profile, from low-power ground idle to full-power take-off conditions [26,28,29]. Tacina et al. [27] studied the first generation swirl-venturi LDI (SV-LDI-1) design comprised of nine identical fuel/air mixers at the same exit plane. Each fuel/air mixer consisted of a simplex fuel injector and an air passage with an axial air swirler followed by a converging-diverging venturi-flare section. The authors reported that reducing the swirler angle reduced NO_x emissions, however combustor operability suffered [27]. The second generation of swirl-venturi LDI (SV-LDI-2) [30–33] was developed to improve the low power operational range and further reduce NO_x emissions. New features of the single element injector included airblast injectors with inner and outer air swirlers in place of the original simplex injectors with a single swirler [30]. In this fuel injection method, the inner swirling air flow assists fuel atomization and facilitates mixing of the air and fuel. In addition, in the SV-LDI-2 designs, the size of each fuel/air mixer varies, and may be in-plane with the dome or recessed, as shown in Figure 1-3. The pilot swirler for all three configurations used a relatively larger vane angle (57°) in an effort to improve low power operation. All main stages (noted as m1, m2, and m3 in Figure 1-3) for the three configurations employed a swirler vane angle of 45° to reduce the emissions. The injectors for m1 and m2/m3 were simplex and airblast, respectively, which was thought to maintain the operability at low power while reducing emissions at high power. By employing airblast tip injectors and a pilot fuel/air mixer, the SV-LDI-2 configurations were shown to increase the operating range and combustion efficiency at low power conditions and improve upon overall NO_x emissions relative to the SV-LDI-1 designs [30,31].

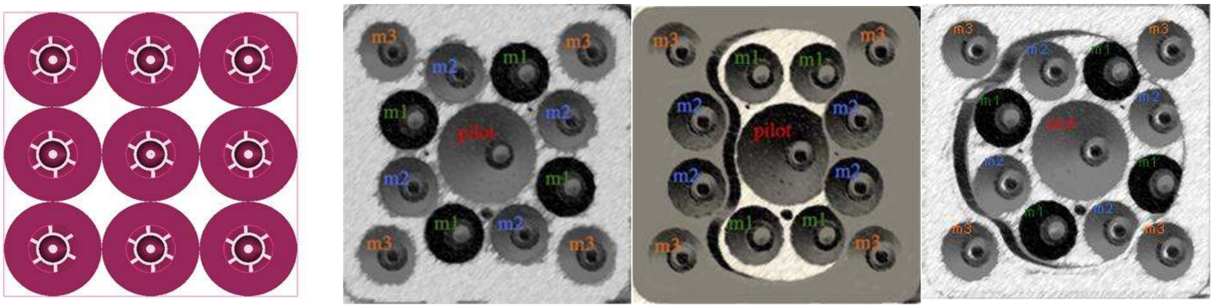

SV-LDI-1 SV-LDI-2

Figure 1-3. Injector arrangement of SV-LDI-1 [27], and SV-LDI-2 [30].

Although significant effort has gone into the investigation of injector-to-injector interactions for multiplex fuel injectors, the fundamental behavior of the individual LDI swirl injector is critical to understanding and predicting the performance of the system as a whole. Fu et al. [34] explored the impact of axial swirler vane angle on an LDI-type injector, demonstrating the presence of a center recirculation zone stabilized at the injector exit only for strongly swirled cases with vane angles exceed 55°. For weakly swirled designs, only small corner recirculation zones were observed. Cai et al. [35] studied the behavior and structure of the fuel spray in a similar configuration with a 60° vane angle, using two-component phase Doppler measurements. Villalva-Gomez et al. [36,37] used OH planar laser induced fluorescence (PLIF) measurements to characterize the flame structure in an industry-developed LDI injector, while Li et al. [38] explored a novel LDI concept swirl injector based upon injection of fuel through a porous media wall. Yi and Santavicca [39] meanwhile studied combustion instabilities using a single LDI-type injector, observing self-excited instabilities but no vortex shedding. Others have sought to explore the LDI concept numerically. El-Asrag et al. [40] demonstrated the importance of radiation effects on fuel spray, finding that failing to include radiation caused an over-prediction in spray evaporation rates, with commensurate impacts to computed local mixture fractions, combustion heat release rates, and emissions indices. Li et al. [41] used an realizable k-epsilon (RKE) Reynolds-Averaged Navier-Stokes (RANS) model to simulate a hydrogen-fueled LDI injector with a 23-step finite rate chemical mechanism, in which the pressure drops, total temperatures, and NO emissions indices were discussed for various operating conditions. Patel and co-workers [42,43] examined an LDI-type fuel injector with Large Eddy Simulation (LES), demonstrating that the inclusion of a droplet breakup model primarily impacted the fuel evaporation near the injector exit, while time-averaged results with and without a breakup model were similar further downstream. Furthermore, the authors were able to capture unsteady features such as the precessing vortex core [42].

The above-mentioned studies indicate that specific design features of the LDI air swirler/fuel injector assemblies are critical to the combustor performance. Although significant research efforts have been made for the development of LDI combustion, there remains much uncertainty regarding the practical impacts of specific design features of LDI swirl injectors. Previous multi-point LDI studies have demonstrated overall test outcomes like emission index, combustion efficiency, and combustor operability, but have very limited results regarding the details of flow and flame fields from various LDI mixer designs. The foregoing investigations of single-point LDI mixer have reported effects of some design features on LDI performance. However, under reacting conditions, high quality datasets of flow and flame structures, and emission distributions are still meager, especially for SV-LDI-2. Furthermore, under most circumstances, only one of design features was explored for the same LDI configuration, thereby missing the information regarding how LDI combustion is impacted by multiple mixer design aspects. Additionally, there is a need of specific analysis that assesses the capability of computational fluid dynamics (CFD) simulation tools with detailed data validation. Thus, systematically experimental and computational studies on the fundamental behavior of individual swirl-injector are necessary, which motivates a series of comprehensive studies of the second-generation SV-LDI configuration.

1.2 Objectives

The current dissertation covers fundamental investigations by both experiments and CFD simulations to understand the impacts of mixer designs on methane-fueled single-injector LDI performance. The key goals of experimental studies are to design and set up a new test system, and collect advanced diagnostic data for various SV-LDI-2 geometric design effects, including different outer air swirler (OAS) vane angles, inclusion or exclusion of the flare part, and two opposite rotation directions of OAS and inner air swirler (IAS), under various non-reacting and reacting conditions. The detailed fundamental single-cup experiments are conducted to collect high fidelity results, including velocity field, flame structures, and radical species distributions, as well as NO_x level and LBO limits. Meanwhile, the objectives of LDI simulations are to identify an accurate and cost-effective meshing strategy, and optimal turbulence and combustion models to predict flow, flame, and emission characteristics of LDI combustion. With extensive results from experiments and simulations, the impacts of swirler vane angle, flare geometry, and relative swirling direction between swirlers on flow and flame characteristics of LDI combustion are systematically analyzed, providing insights into the development of LDI combustors.

The mixer features of LDI studied herein include:

- OAS vane angles
- Venturi-flare geometry
- OAS/IAS rotation direction

The experimental measurements used in this thesis study include:

- Flow field measurements by time-resolved particle image velocimetry (TR-PIV)
- Radical field measurement by OH*/CH* chemiluminescence and OH-PLIF
- NO_x emission characterization by NO_2* chemiluminescence
- Flame response characterization by broadband flame imaging

The CFD simulations investigation herein includes:

- Grid independence study with different sizes of mesh grids
- Non-reacting flow field simulations with RANS and LES
- Reacting flow and flame field simulations with RANS- and LES-Flamelet Generated Manifold (FGM)

1.3 Organization of the Dissertation

Chapter 2 describes in detail the experimental setup and procedures applied in this thesis study, as well as the numerical setup to simulate the flow fields and flames of single SV-LDI-2 mixer configurations. Chapter 3 covers the study on the impact of OAS vane angle on LDI pilot mixer operability and emissions. Chapter 4 provides the experimental investigation of lean-dome high-airflow airblast pilot mixers' operability, emissions, and dynamics. Chapter 5 explores the meshing strategy and best practices of turbulence modeling to simulate non-reacting flows of counter- and co-swirling LDI configurations. Chapter 6 further evaluates the performance of FGM method on predicting reacting flows of LDI mixers and investigates the impact of OAS/IAS rotating direction on flames. Chapter 7 summarizes the findings of this dissertation and discusses the future research directions.

The work conducted during my thesis studies at University of Connecticut has contributed the following publications.

1. X. Ren, K. B. Brady, X. Xue, C. J. Sung, and H. C. Mongia, "*Experimental Investigation of Lean-dome High-airflow Airblast Pilot Mixers' Operability, Emissions, and Dynamics,*" under review.
2. X. Ren, K. B. Brady, X. Xue, C. J. Sung, and H. C. Mongia, *"An Experimental and CFD Study on Non-reacting Counter- and Co-swirling Flows in LDI,*" under preparation.
3. X. Ren, K. B. Brady, X. Xue, C. J. Sung, and H. C. Mongia, "*An Experimental and CFD Study on Reacting Counter- and Co-swirling Flows in LDI,*" under preparation.
4. X. Ren, X. Xue, K. B. Brady, C. J. Sung, and H. C. Mongia, "*The Impact of Swirling Flow Strength on Lean-Dome LDI Pilot Mixers Operability and Emissions*," Experimental Thermal and Fluid Science, 2019, p. 109840.
5. X. Ren, X. Xue, K. B. Brady, C. J. Sung, and H. C. Mongia, "*Lean-Dome Pilot Mixers' Operability Fundamentals*," Innovations in Sustainable Energy and Cleaner Environment (Ed.: A. Gupta, S. Aggarwal, etc.), *Springer*, 2020, pp. 387-409.

6. X. Ren, C. J. Sung, and H. C. Mongia, "*On Lean Direct Injection Research*," Energy for Propulsion: A Sustainable Technologies Approach (Ed.: A. Runchal, A. Gupta, A. Kushari, A. De, and S. Aggarwal), *Springer*, 2018, pp. 3-26.
7. X. Ren, X. Xue, K. B. Brady, C. J. Sung, and H. C. Mongia, "*Fundamental Investigations for Lowering Emissions and Improving Operability*," Propulsion and Power Research, 2018, 7(3), pp. 197-204.
8. X. Ren, X. Xue, C. J. Sung, K. B. Brady, H. C. Mongia, and P. Lee, "*The Impact of Venturi Geometry on Reacting Flows in a Swirl-venturi Lean Direct Injection Airblast Injector*," In 52nd AIAA/SAE/ASEE Joint Propulsion Conference 2016. AIAA2016-4650.
9. X. Ren, K. B. Brady, C. J. Sung, H. C. Mongia, and P. Lee, "*Impact of Air Swirler Rotation Direction on the Flow Field and Performance of a Lean Direct Injection Concept Fuel Injector*," 2016 Spring Technical Meeting Eastern States Section of the Combustion Institute. ESSCI2016-138IC-0077.

CHAPTER 2 EXPERIMENTAL AND NUMERICAL SPECIFICATIONS

2.1 Experimental Facility

2.1.1 Test facility

In order to facilitate various diagnostics for different single-cup SV-LDI-2 mixers, a new test setup has been designed and set up, as shown in Figure 2-1. From upstream to downstream, the setup consists of air and fuel tanks, flow control system, LDI burner, test section, and exhaust. The air is contained in a 400-gallon tank, which is pressured at 250 – 300 psi to provide air flow of ~6.5 g/s to run under standard temperature and pressure (STP) conditions for experimental duration up to 10 min. A CH_4 cylinder with 99.5% purity from Airgas Company is used to supply gaseous fuel. Orifices are used to control the mass flow rates of air and methane. All orifices are calibrated using the wet gas meter from Shinagawa Corporation (model: W-NK-5A). An in-house designed LDI burner is mounted on a three-axis machine table to facilitate its movement relative to the diagnostic setup. An exhaust hood with 2 feet by 2 feet area takes away all combustion gases from LDI burner exit. For laser diagnostics, safety shields are mounted along the laser beam.

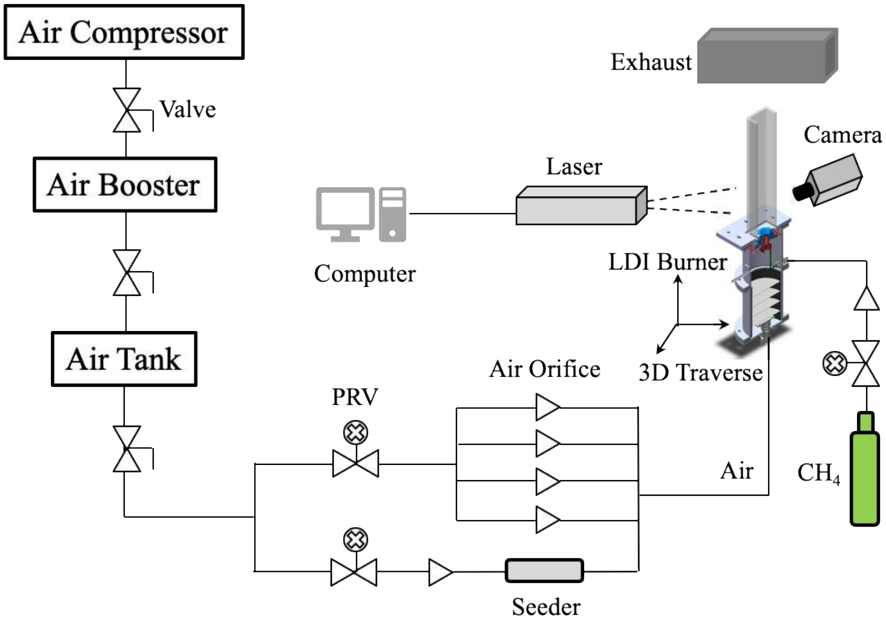

Figure 2-1. Schematic of test facility. “PRV” stands for pressure regulator valve.

2.1.2 Burner setup

The present LDI burner setup has been developed to investigate single-cup swirling flow/fuel injection systems in an optically-accessible environment under atmospheric pressure conditions. A diagram of the experimental apparatus is shown in Figure 2-2. The swirler entrance manifold measures 80 mm × 90 mm (diameter × length). A set of three stacked fine-mesh inserts (40 × 40 openings-per-inch) within the air inlet is designed to provide a uniform velocity profile to the entrance of the swirler manifold. The air inlet pressure (P_3) is measured in the entrance manifold 50 mm (L_{US}) upstream of the dump plate using an Omega PX303 pressure transducer with full scale accuracy of 0.25% and 0.01 Torr resolution. The air and methane mass flow metering is accomplished using a set of calibrated flow orifices. Gaseous fuel, i.e. methane, is used here to circumvent atomization complications of liquid fuel. The entire burner assembly is mounted to the dump plate such that the exit plane of the flare is flush with the dump plate surface. The test chamber – consisting of a 50.8 mm × 50.8 mm × 300 mm (interior dimensions) section constructed from quartz – is likewise secured to the dump plate, concentric with the swirler assembly.

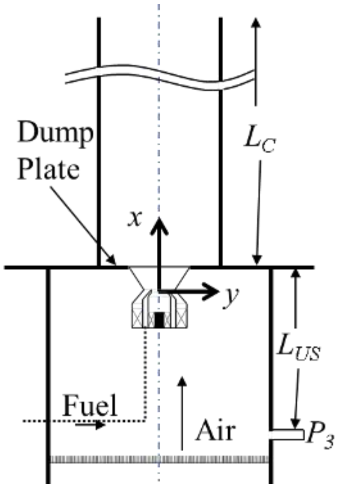

Figure 2-2. Schematic of the LDI experimental apparatus.

2.1.3 LDI-related configurations

A schematic of the single-element LDI injector used in this study is shown in Figure 2-3. It consists of a fuel tip with two concentric axial air swirlers; an inner air swirler (IAS) is contained within the airblast-type fuel tip, while the outer air swirler (OAS) is located between the fuel tip and the venturi inner wall. The venturi contracts to a throat diameter D_t=13.2 mm with a full cone angle of 120°, while the flare expands at a full-cone angle of 70°. The distance between the start of the venturi contraction and the throat is x_{vc}=5.8 mm, while the flare length is x_f=9.4 mm. The coordinate system for this study has its origin at the center of the venturi throat, with the positive x-direction in the bulk flow direction.

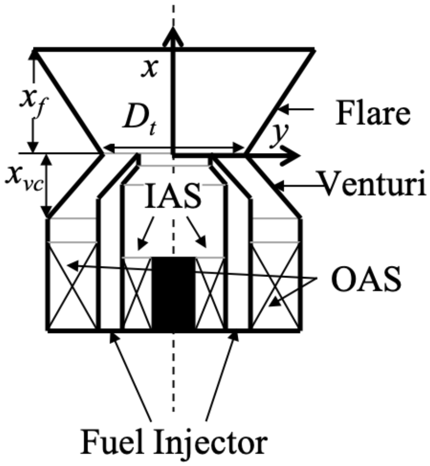

Figure 2-3. Schematic of the swirl-venturi LDI mixer.

The design features of LDI-related configurations that are investigated in current studies include the vane angle of OAS, the inclusion or removal of flare, and the relative rotating direction between swirling flows of IAS and OAS. The helical IAS vanes are fixed at a 60° counter-clockwise (CCW) rotation, while the helical OAS vanes have two angles: 60° or 45°, as exhibited in Figure 2-4. The angle of swirler blade is measured from the blade tail tip. For different blade vane angles, the length of blade is kept constant. Helical vanes are used for both swirlers as a consideration for smaller pressure drop [44] and larger reverse mass flows [45,46] compared to flat-vaned swirlers with the same angle.

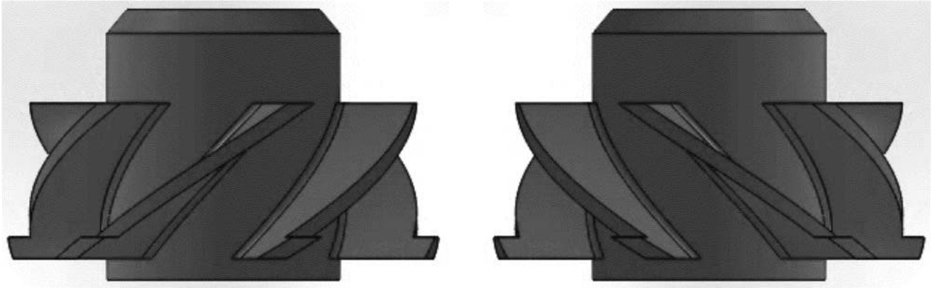

60˚-vane-CW OAS 60˚-vane-CCW OAS

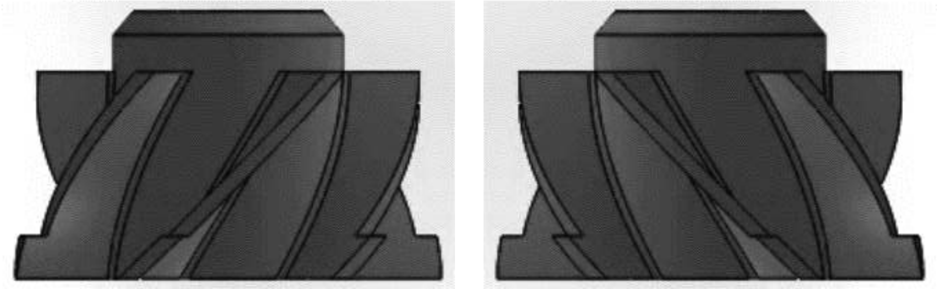

45˚-vane-CW OAS 45˚-vane-CCW OAS 60˚-vane-CCW IAS

Figure 2-4. Swirlers used in the current LDI related studies.

Another important feature in SV-LDI is the flare geometry. In this study, two cases are researched: with flare or without flare. Without flare, the configuration is named by “Airblast”, as its configuration with a converging venturi is quite similar to traditional airblast mixer [47]. With a diverging flare following a converging venturi, the configuration is named as “LDI”. The exit plane of the venturi or flare is flush with the dump plate in LDI or Airblast configuration. On the other hand, the mixers with flare is noted as swirl-venturi LDI (SV-LDI), following the nomenclature of NASA SV-LDI research, or simply as LDI. The schematics of SV-LDI and airblast mixers are depicted in Figure 2-5.

To emphasize on the interactions between swirling flows of IAS and OAS, two relative rotation directions of swirlers are mounted for current burner. For each OAS vane angle (60˚ or 45˚), the OAS has two options of rotation directions: clockwise (CW) or counter-clockwise (CCW) as shown in Figure 2-4, which is the rotation direction when looking from the upstream side. Meanwhile, the IAS vanes are fixed at a 60° CCW rotation. Thus, there are two relative swirling directions between the OAS and IAS flows, i.e. counter-swirling or co-swirling.

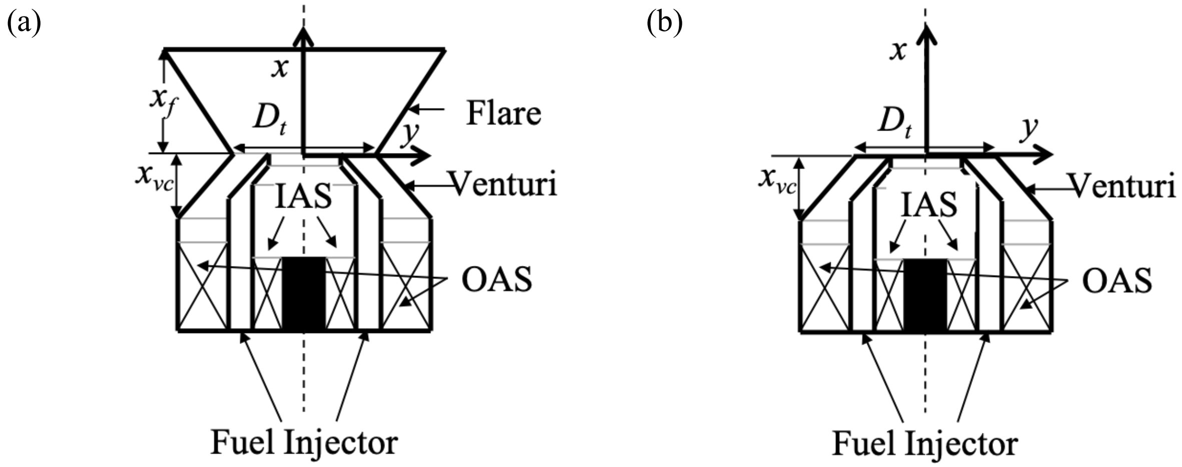

Figure 2-5. Schematics of (a) swirl-venturi LDI mixer, and (b) airblast mixer.

Table 2-1. Configuration specifications of swirlers and venturi-flare geometry used in the present fundamental research.

Configuration	Swirler (IAS/OAS)	Venturi-Flare Geometry	Relative Rotating Direction
LDI-60-CW	60˚CCW/60˚CW	With flare	Counter-swirling
LDI-60-CCW	60˚CCW/60˚CCW	With flare	Co-swirling
Airblast-60-CW	60˚CCW/60˚CW	Without flare	Counter-swirling
LDI-45-CW	60˚CCW/45˚CW	With flare	Counter-swirling
Airblast-45-CW	60˚CCW/45˚CW	Without flare	Counter-swirling

With all the three design variables of mixers, the LDI-related configurations are abbreviated by the information of flare ("LDI" as with flare and "Airblast" as without flare), OAS vane angle ("60" or "45"), and OAS/IAS relative rotation direction ("CW" for counter-swirling and "CCW" for co-swirling). To illustrate the effect of all three design features on LDI performance, total five LDI-related configurations, as listed in Table 2-1, are assembled and researched.

2.2 Experimental/Diagnostics Specifications

2.2.1 Lean blowout (LBO) test procedure

The operability of lean-dome burn is a critical design factor in LDI combustor. Here the LBO limits of single-cup LDI configurations are tested under 0.5 – 3 % pressure drop. For each LBO test, the flame is ignited at a relatively high overall equivalence ratio, ~ϕ=0.8. After the flame is steadily burning, the air flow rate is maintained at constant while the fuel flow rate is reduced gradually. At first, the fuel flow rate is reduced with large steps. When fuel flow rate is close to LBO limit (know from initial trials), it is reduced by small steps, which is less than 1 mg/s and no more than 0.004 change in overall equivalence ratio. The smallest step of fuel flow rate reduction is determined by the minimum rotating step of the pressure regulator valve and the diameter of the orifice used. After each step of reducing fuel flow rate, the flame is examined for about 10 – 20 sec to check whether the flame is able to sustain. Either flame extinction within chamber or flame fully moving out of chamber is treated as LBO. Since flame is fairly weak near the LBO, all the LBO tests are carried out without other light sources to better observe flame location. The LBO testing is repeated at least three times for every condition. The standard deviation of each test condition in the same LDI-related configuration is used as the error bar for plotting LBO as a function of pressure drop.

2.2.2 Time resolved particle image velocimetry (TR-PIV)

The measurements of the velocity field are made using a Dantec Dynamics two-dimensional TR-PIV system. All axial-radial velocity data presented in this study are collected with the laser sheet aligned with the center plane of the experiment, as demonstrated in Figure 2-6. The sheet thickness is approximately 1 mm. The laser repetition rate is set to 5 kHz and aluminum oxide seeding particles with 1 μm nominal mean diameter are used, based upon the recommendation of Melling [48] that seeding particle diameter should not exceed 1 μm to have sufficient frequency response at 10 kHz. Interrogation areas are set to 0.6 mm × 0.6 mm, with 50% overlap. Laser pulse delay times are set to approximately follow the "1/4 rule" – frame-to-frame particle movement of approximately 1/4 of the interrogation area dimensions – within the regions of interest. The capture area for the mean axial-radial velocity map (U-V) is 50 mm × 60 mm, focused on the area from the dump plate to 60 mm downstream. The 800 × 800-pixel camera is located at a distance of 0.6 m from the laser plane, with a 55 mm focal length Nikkor lens. The F-stop of lens is set at 5.6 for all test cases. A 532 nm bandpass filter is mounted in front of the camera lens to eliminate light sources not corresponding to the laser wavelength. For each test case, 5,000 image pairs are collected over a one second duration. Data processing is accomplished with the commercial software DynamicStudio.

The error in PIV measurement stems from two major parts: timing of the laser light sheet pulses and displacement estimation of the seeding particles. The full-scale accuracy of PIV given by Wernet [49] is shown below:

$$\frac{\sigma_u}{U} = \left[\left(\frac{\sigma_t}{T}\right)^2 + \left(\frac{\sigma_d}{D}\right)^2\right]^{1/2} \tag{2-1}$$

Here, σ_t is the discriminative minimum period between pulses, *T* is period between pulses, σ_d is discriminative minimum displacement, *D* is maximum displacement based on ¼ rule. For current tests, σ_t is in the range of 5 - 10 ns, and *T* is 200 μs. The timing error, $\sigma_t/T = 2.5\text{x}10^{-5}$ - $5\text{x}10^{-5}$, is therefore negligible. For optimally configured optical system, the correlation peak estimation error σ_d is around 0.1, while the maximum displacement is limited by correlation area size. For 16x16 pixel area, *D* is 4 without shifting. Hence, the displacement error, σ_d/D is 2.5%, which is approximately the full-scale accuracy of the current PIV measurements.

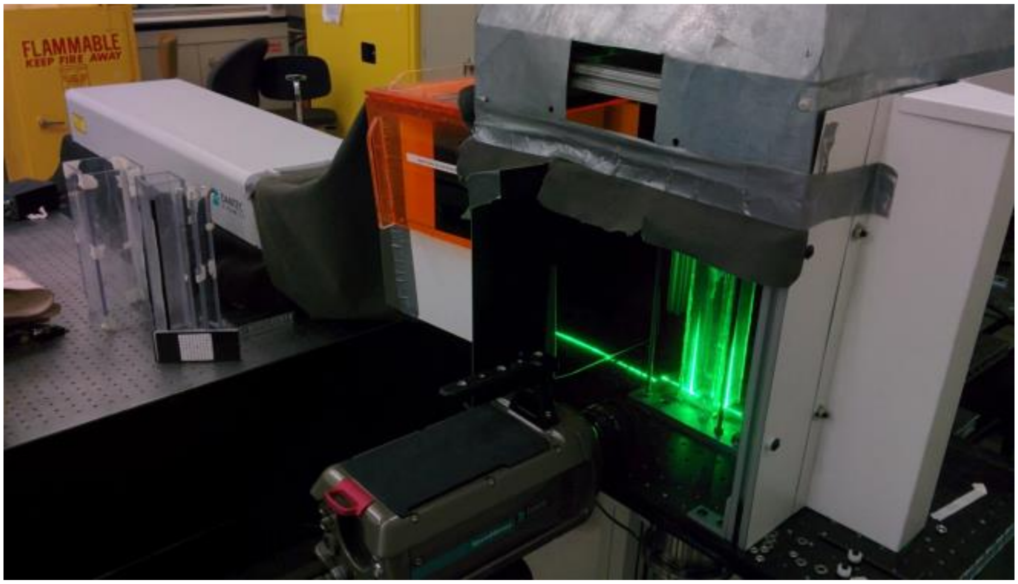

Figure 2-6. A picture of PIV test.

2.2.3 OH*, CH*, and NO_2* chemiluminescence measurements

The OH*, CH*, and NO_2* chemiluminescence are measured using a PI-MAX III intensified charge coupled device (ICCD) camera with 1024 × 256 pixels. The camera is located 1.8 m from chamber center axis. A Nikon 105 mm UV lens is mounted in front of camera with F-stop 4.5. The gain value is 15 with 100 ms exposure time. To compare differences caused by LDI-related mixers and various overall equivalence ratios, all camera settings are kept the same for all chemiluminescence tests. Species-specific bandpass filter for each radical is mounted in front of the lens: the bandpass filter used for OH* is 310±2 nm, with 10 nm full width at half maximum (FWHM), which is purchased from Newport Corporation, with part ID 10BPF10-310; CH* that used for is 430±2 nm with 10 nm FWHM (Newport, 10BPF10-430); NO_2* measurements use 750±10 nm, with 70 nm FWHM (Newport, 10BPF70-750), based upon the recommendation by Pearse and Gaydon [50] to monitor nitrogen dioxide (NO_2) emissions in the range of 608.8–851.5 nm. NO_2* is used here as a proxy indicator for the emission index of NO_x ($EINO_x$), which refers to the total production of nitric oxide (NO) and NO_2 per unit mass of fuel. Each data set is averaged over 100 consecutive individual images at 10 Hz to obtain a mean radical distribution. The 100 images are found to be sufficient to obtain averaged chemiluminescence distributions of current conditions. A 5 × 5 pixel^2 median filter is also applied to the image to reduce noise.

2.2.4 OH planar laser induced fluorescence (OH-PLIF)

The excitation of OH radicals requires activation through a specific laser wavelength. This is achieved via a laser system, which consists of a Nd:YAG laser (Continuum, Powerlite 8010) used to pump a dye laser unit (Continuum, ND6000), where Rhodamine 590 is circulated and exposed to the pump laser. The dye laser output has a wavelength of ~566 nm which is then frequency doubled to ~283 nm to excite the target absorption line of Q1(6). The laser beam is converted to a laser sheet with ~1 mm thickness and covers a 30 mm high region of flow beginning from the dump plate plane. To capture the OH-PLIF signal, a PI-MAX III ICCD camera is used, with mean image averaged from 50 background-subtracted images for each test condition. The camera is located 0.8 m from the chamber center axis. A Nikon 105 mm UV lens is mounted in front of camera with F-stop 4.5. The gain value is 60 with 80 ns exposure time after 70 ns delay. A bandpass filter is mounted in front of the lens, with a band center at 310±2 nm and 10 nm FWHM.

2.3 Numerical Specifications

2.3.1 Computational domain and mesh generation

The three-dimensional computational domain for LDI experiments consists of air inlet manifold, swirler-venturi assembly, and combustion chamber, as shown in Figure 2-7. The grids are generated by cut-cell Cartesian grid method [51,52], which allows the use of orthogonal grids by eliminating the need for the grid to be morphed with the geometry while precisely capturing the boundary shapes. The base grid size is Δ_0, which is applied to regions of air manifold or downstream of combustor, as outlined in Figure 2-7. To balance the computational cost and the need to resolve sufficient scales of turbulence, the fixed embedding is applied to better resolve the flows within swirlers and venturi with $\Delta_2=\Delta_0/2^2$ and near-dome region with $\Delta_1= \Delta_0/2^1$, as shown in the close-up look in Figure 2-7. Note that in Δ_n, n represents the level of mesh refinement with respect to the base grid size. In addition, to resolve the flow field, extra mesh resolution can be included during runtime via an adaptive mesh refinement (AMR) technique on the basis of local temperature and velocity gradients, which can be used to refine the mesh in the steepest gradient regions while coarsening the mesh in shallow gradient regions [51].

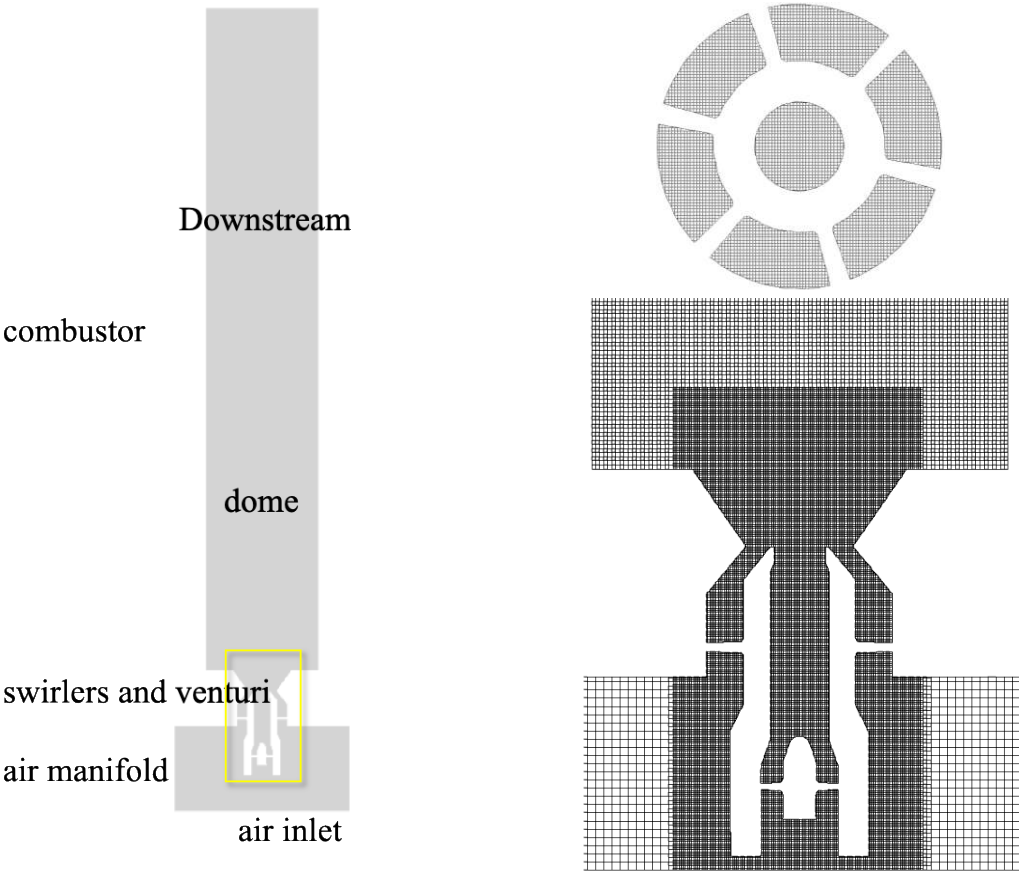

Figure 2-7. Computational domain (left) and grid distribution in horizontal cut of swirler (right top) and close-up look of swirler-venturi assemble (right bottom).

2.3.2 Turbulence modeling

For the three-dimensional computational investigations, the CONVERGE CFD code [51] is used with the Reynolds-Averaged Navier-Stokes (RANS) turbulence model or large eddy simulation (LES). For RANS modeling, Reynolds decomposition separates the flow properties as mean and fluctuating components, which on time-averaging yields the Reynolds-averaged equations as follows:

$$\frac{\partial \bar{\rho}}{\partial t}+\frac{\partial \bar{\rho}\overline{u_i}}{\partial x_i}=0 \tag{2-2}$$

and

$$\frac{\partial \bar{\rho}\overline{u_i}}{\partial t}+\frac{\partial \bar{\rho}\overline{u_i}\overline{u_j}}{\partial x_j}=-\frac{\partial \bar{p}}{\partial x_i}+\frac{\partial}{\partial x_j}\left[\mu\left(\frac{\partial \overline{u_i}}{\partial x_j}+\frac{\partial \overline{u_j}}{\partial x_i}\right)-\frac{2}{3}\mu\frac{\partial \overline{u_k}}{\partial x_k}\delta_{ij}\right]\frac{\partial^2 \overline{u_i}}{\partial x_j^2}-\frac{\partial \tau_{ij}}{\partial x_j} \tag{2-3}$$

Here, $\overline{u_i}$ and u_i' are the mean and fluctuating components of the velocity u_i in the x_i-direction, respectively, $\bar{\rho}$ is the mean density, $\bar{p}$ is the mean pressure and μ is the dynamic viscosity. The velocity fluctuations introduce additional stresses in the fluid, namely the Reynolds stresses, $\tau_{ij}=\rho\overline{u_i'u_j'}$, which need to be modeled to close the equations. Here, the standard *k*-*ε* (SKE) [53] turbulence closure model is considered to simulate the turbulent swirling flow in the RANS case, which offers the best data match of RANS models in predicting recirculation bubble of the swirl cup modeling [54].

The SKE model assumes the Reynolds stresses to be isotropic and solves for two addition equations, one for the kinetic energy k and another for the dissipation rate *ε*, as follows:

$$\frac{\partial}{\partial x_i}(\rho k u_i)=\frac{\partial}{\partial x_j}\left[(\mu+\frac{\rho C_\mu k^2}{\sigma_k \varepsilon})\frac{\partial k}{\partial x_j}\right]+G_k+G_b-\rho\varepsilon-Y_M+S_k \tag{2-4}$$

and

$$\frac{\partial}{\partial x_i}(\rho \varepsilon u_i)=\frac{\partial}{\partial x_j}\left[(\mu+\frac{\rho C_\mu k^2}{\sigma_k \varepsilon})\frac{\partial \varepsilon}{\partial x_j}\right]+C_{1\varepsilon}\frac{\varepsilon}{k}(G_k+C_{3\varepsilon}G_b)-C_{2\varepsilon}\rho\frac{\varepsilon^2}{k}+S_\varepsilon \tag{2-5}$$

Here, G_k is turbulent kinetic energy generated by the average velocity gradient. G_b is turbulent kinetic energy generated by buoyancy. Y_M represents the contribution of the fluctuating dilatation in compressible turbulence to the overall dissipation rate. S_k and S_ε are user-defined source terms. In SKE, the model constants have the following values, $C_{1\varepsilon} = 1.44$, $C_{2\varepsilon} = 1.92$, $C_{2\varepsilon} = -1$, $C_\mu = 0.09$, $\sigma_k = 1.0$, and $\sigma_\varepsilon = 1.3$.

In RANS, the entire spectrum of turbulent scales is modeled. However, in LES, the large scale eddies are solved directly and only the small scale eddies are modeled. LES uses a spatial filtering operation to separate the large scale and small scale eddies of the flow, resulting in filtered continuity, and momentum equations of the Favre averaged Navier-Stokes as follows:

Conservation of Mass:

$$\frac{\partial \bar{\rho}}{\partial t} + \frac{\partial \bar{\rho}\widetilde{u_i}}{\partial x_i} = 0 \qquad (2\text{-}6)$$

Conservation of Momentum:

$$\frac{\partial \bar{\rho}\widetilde{u_i}}{\partial t} + \frac{\partial \bar{\rho}\widetilde{u_i}\widetilde{u_j}}{\partial x_j} = -\frac{\partial \bar{P}}{\partial x_i} + \frac{\partial \overline{\sigma_{ij}}}{\partial x_j} - \frac{\partial \tau_{ij}}{\partial \mathrm{x_j}} \qquad (2\text{-}7)$$

Here $\overline{\sigma_{ij}}$ is the viscous stress tensor:

$$\sigma_{ij} = \mu\left(\frac{\partial u_i}{\partial x_j} - \frac{\partial u_j}{\partial x_\mathrm{i}}\right) + (\mu' - \frac{2}{3}\mu)(\frac{\partial u_k}{\partial x_k}\delta_{ij}) \qquad (2\text{-}8)$$

where the Favre average, ˜, is obtained from spatial filtering, $\tilde{\phi} = \overline{\rho\phi} \,/\, \overline{\rho}$. In the above equations, $\delta_{ij}$is the Kronecker delta. $\tau_{ij} = -\bar{\rho}(\widetilde{u_i' u_j'} - \widetilde{u_i'}\widetilde{u_j'})$ is the sub-grid tensor term, which is modelled using Dynamic Smagorinsky SGS model [55–57], or Dynamic Structure SGS with an additional transport equation for sub-grid kinetic energy [58], representing zero-equation or one-equation LES models, respectively. The impact of SGS models in LES on predicting LDI turbulent flows is explored.

The near-wall turbulence in RANS is modeled by the standard wall function, which makes use of the law-of-the-wall assumption for velocity in the log-law region of a turbulent boundary layer

[59]. The near-wall turbulence in LES is simulated by the Werner and Wengle wall model [60]. This model is based on the concept of velocity law-of-the-wall boundary condition, but does not require iterations, which is less computational expensive in LES applications. Since the major flow patterns in LDI are in the core of chamber, the effects of wall boundary conditions on LES results were not further explored in this thesis.

2.3.3 Combustion modeling

For a consideration of saving computational cost, Flamelet Generated Manifold (FGM) is used as combustion model, in which a low-dimensional manifold is formed from solutions of the so-called flamelet equations. Resulting from the full set of 3D transport equations [61], a set of 1D equations describes conservation of mass, species, and enthalpy in a flame adapted coordinate system. Neglecting the flame curvature, these equations can be described as follows:

$$\frac{\partial(\rho u)}{\partial s} = -\rho K \tag{2-9}$$

$$\frac{\partial(\rho u Y_i)}{\partial s} = \frac{1}{Le_i}\frac{\partial}{\partial s}\left(\frac{\lambda}{C_p}\frac{\partial Y_i}{\partial s}\right) + \dot{\omega}_i - \rho K Y_i, i = 1, 2, \dots\dots\dots, N_s - 1 \tag{2-10}$$

$$\frac{\partial(\rho u h)}{\partial s} = \frac{\partial}{\partial s}[\frac{\lambda}{C_p}\frac{\partial h}{\partial s} + \sum_{i=1}^{N_s} h_i \frac{\lambda}{C_p}(\frac{1}{Le_i} - 1)\frac{\partial Y_i}{\partial s}] - \rho K h \tag{2-11}$$

where u, s, K, ρ, h, Y_i, $\dot{\omega}_i$, C_p, λ, and Le_i are the velocity, spatial coordinate perpendicular to the flame front, flame stretch rate, mixture density, enthalpy, mass fraction of species, chemical production rate, specific heat at constant pressure, thermal conductivity, and Lewis number [61], respectively. In LDI combustion, the air and fuel streams are injected separately from air swirlers and fuel injector tip, respectively. Thus, the flame is considered as a diffusion flame. In order to build the look-up table of diffusion flame, the above equations are solved for a planar opposed-flow diffusion flame at constant pressure. For a two-dimensional manifold, sets of opposed-flow diffusion flamelets are calculated for varying strain rate. Zero strain rate is the lowest strain rate, which represents chemical equilibrium. There exists a limit of strain rate where diffusion flamelet extinguishes. Consequently, time-dependent flamelet solutions [51] are used beyond the extinction strain rate. FGM simplifies the chemistry into two scalars, the mixture fraction, Z, and the reaction progress variable, c. A look-up table is generated based on these scalars in addition to enthalpy, and the variance of Z (Z''^2). The reaction progress variable, c, is defined as the sum of the product mass fractions normalized by their equilibrium values, shown as below:

$$c = \frac{\sum \beta_k Y_k}{\sum \beta_k \, Y_k^{eq}} \tag{2-12}$$

where Y_k denotes specie mass fraction and β_k represents weighting factor for k^{th} species. β_k equals to 1 for CO and CO_2, and 0 for all other species. In this study, the reaction progress equals:

$$c = \frac{Y_{\mathrm{CO}} + Y_{\mathrm{CO2}}}{Y_{\mathrm{CO}}^{eq} + Y_{\mathrm{CO2}}^{eq}} \tag{2-13}$$

Therefore, c increases monotonically from unburned (c=0) to burned (c=1) regions of flame.

Full kinetics flamelet solutions are obtained by means of a specialized 1D flame code built in CONVERGE CFD [51], coupled with the GRI-Mech 3.0 mechanism [62], which consists of 325 elementary reactions and 53 species. For turbulence-chemistry interaction (TCI), the general methodology of FGM used in this work requires additional equations in the CFD solver. The 1D diffusion flamelet uses a beta function for Z probability density function (PDF) and delta functions for the PDFs of c, h, Z''^2. More details can be found in the reference [51].

2.3.4 Numerical setup

The finite volume based compressible flow solver CONVERGE [51] is employed for this study. A second-order-accurate spatial discretization scheme is used for the governing conservation equations. For LES, a fully-implicit first-order-accurate time integration scheme is used to maintain numerical stability. The transport equations are solved using the Pressure Implicit with Splitting of Operators (PISO) method [63]. Variable time-step is automatically calculated for each time-step, with minimum as 10^{-8} s and maximum as 10^{-5}s. The temporal resolution is sufficiently accurate, which is guided by maximum convection Courant-Friedrichs-Lewy (CFL) number, the speed of sound CFL number, and the diffusive CFL number. The turbulence statistics collection starts at two flow-through time after flow field initialization. To get converged turbulence statistics, the data are collected over more than three flow-through time in LES cases. The flow-through time is defined by dividing the combustor volume over the volumetric flow rate. The calculations are run in parallel on distributed memory machines using the Message Passing Interface (MPI).

2.4 Data Normalization

When presenting the results in the following discussions, the axial distance (x) and radial distance (y) are normalized by the venturi throat diameter, D_t, while all axial-radial velocity components are normalized by the characteristic velocity magnitude, U_t, based on the mean axial velocity magnitude at the venturi throat area, defined as follows:

$$U_t = \frac{\dot{m}}{\rho_{air} A_t} \tag{2-14}$$

Here, $\dot{m}$ is the total mass flow rate, ρ_{air} is the air density, and A_t is the area of venturi throat. In addition, all turbulent kinetic energy results are scaled by $U_t^2/2$.

CHAPTER 3 THE IMPACT OF SWIRLING FLOW STRENGTH ON LDI PILOT MIXERS' OPERABILITY AND EMISSIONS

3.1 Introduction

In a fundamental sense, the LDI concept encompasses any fuel injection device intended to operate under lean-dome conditions without the aid of premixing/pre-vaporizing chambers or other devices. As a result, the LDI concept relies upon rapid fuel vaporization and subsequent fuel/air mixing to achieve sufficiently well-mixed conditions prior to combustion; this reliance furthermore implies that the specific design features of the LDI air swirler/fuel injector are critical to the combustor performance of this concept.

Although significant effort has gone into the investigation of injector-to-injector interactions for multiplex fuel injectors, the fundamental behavior of the individual swirl injector is critical to understanding and predicting the performance of the system as a whole. The effect of swirler vane angle (swirl strength) has been studied for various combustion applications [64–67]. Alkabie and Andrews [64] studied the effect of radial swirler vane angle on extinction, combustion efficiency, and NOx emissions in a range of 0–60˚. It was found that reducing the vane angle from 60˚ to 20˚ significantly reduced NO_x emissions. However, the lean blowout equivalence ratio increased dramatically when the vane angle was reduced from 60˚ to 45˚. Comparing to swirlers with the vane angles of 15˚, 30˚, and 60˚, Raj and Ganesan [65] found that a 45˚ vane swirler produced the best swirl flow field characteristics in the aspects of recirculation zone dimension and pressure drop, which aided fuel/air mixing for complete combustion. Pourhoseini and Asadi [66] demonstrated for industrial burners that an optimum swirler angle exists exhibiting both high combustion efficiency and low CO and NO emissions. Wang et al. [67] reported that ground ignition performance of a 30˚ vane case was improved over that of a 20˚ vane case for the main stage of an LPP combustor due to an improved fuel-air distribution around the ignitor tip.

However, the study of swirl strength influence for single-element LDI swirler is limited. Fu et al. [34] explored the impact of axial swirler vane angle on an LDI-type injector, demonstrating the presence of a center recirculation zone (CRZ) stabilized at the injector exit only for strong swirler cases with vane angles exceeding 55˚. For weak swirler designs, only small corner recirculation zones (CRNZs) were observed. Yi and Santavicca [39] used CH* chemiluminescence to study flame structure for stable and unstable conditions using a single LDI-type injector. Villalva-Gomez and co-authors [36,37] used particle image velocimetry (PIV), OH* chemiluminescence, OH planar laser-induced fluorescence (OH-PLIF) measurements to characterize the flame structure in an industry-developed LDI injector.

Despite the efforts such as the above-mentioned studies, there remains much uncertainty regarding the practical impacts of specific design features of LDI swirl injectors. Given the prior research indicating that features such as the swirl vane angle significantly impact non-reacting flow field structure and spray dynamics, it is critical to future injector design efforts to understand the specific impact of each geometry choice within the LDI design. As a result, the present study represents a first step in a continuing effort to explore these individual impacts, using various non-intrusive diagnostics to develop a robust understanding of geometric design effects on LDI swirl injector performance.

This chapter investigates the outer air swirler (OAS) vane angle impact on lean blowout (LBO) limits, flame behaviors, and NO_x emissions with a counter-rotating axial-axial LDI swirler concept, including a 60˚ clockwise vane OAS (LDI-60-CW) configuration and a 45˚ clockwise vane OAS (LDI-45-CW) configuration, while keeping the same inner air swirler (IAS) of 60˚ counter-clockwise vane angle. These two configurations serve as baseline geometries for the following studies which will investigate the impact of various LDI-relevant swirler geometry features. To this end, key non-reacting and reacting flow field features are identified and characterized using time-resolved PIV (TR-PIV) technique. The flame features of each flow field are also presented and discussed by chemiluminescence/PLIF results.

3.2 Experimental Description and Conditions

For the present study, helical 60° or 45° OAS vanes are installed with a clockwise (CW) rotation direction (looking from the upstream side), while the IAS vanes are fixed at a 60° counter-clockwise (CCW) rotation, forming a counter-swirling shear flow between the IAS and OAS. There are two swirl-venturi LDI configurations that are studied in current chapter to investigate the impact of OAS swirler vane angle on LDI performance, i.e. LDI-60-CW configuration and LDI-45-CW configuration.

The present experimental investigations are focused on obtaining and comparing the velocity field and radical distributions for two LDI configurations with different counter-rotating OAS vane angles. Comparisons are made between the resultant velocity and/or radical fields to establish the interaction between the flow field and the reaction zone under various operating conditions. As will be made evident in due course, the flame response as one progresses from "high" equivalence ratio (e.g., ϕ=0.85) – though still fuel lean – towards LBO changes significantly for each LDI configuration, and moreover shows significant differences as a function of OAS vane angle. As a result, in order to assess the differences between the two OAS configurations and analyze their performance differences, a series of test conditions are chosen that capture representative flame structures as each configuration approaches LBO. To provide a direct comparison between the two OAS vane angles, overlapping test conditions are also chosen where possible for the LDI-60-CW and LDI-45-CW configurations.

Table 3-1 summarizes the operating conditions for each of the experimental cases. It should be noted that while it is recognized by the authors that Reynolds number (*Re*) will impact fuel/air mixing and subsequent combustion, in the present test matrix the air flow – which makes up at least 95% of the total mass flow rate – is kept constant, such that Reynolds number is approximately constant. The air flow rate is kept at a constant 6.633 g/s, which corresponds to a pressure drop across the swirler of 3% for the LDI-60-CW non-reacting flow case. The Reynolds number based on the volumetric flow rate and the venturi throat diameter for each test condition is estimated as 35,000 by the following formula:

$$Re = \frac{\rho_{air} U_t D_t}{\mu_{air}} \tag{3-1}$$

Here, ρ_{air}, D_t, and μ_{air} are air density, venturi throat diameter and air dynamic viscosity, respectively. U_t is the characteristic velocity magnitude as calculated by Eq. 2-16.

Table 3-1. Test conditions of LDI-60-CW and LDI-45-CW configurations.

Case number	Case name	Configuration	Flow rates (g/s)		Overall Equivalence ratio
			Air	Fuel	(ϕ)
1	LDI-60-CW, ϕ=0.85	LDI-60-CW	6.633	0.327	0.85
2	LDI-60-CW, ϕ=0.65	LDI-60-CW	6.633	0.251	0.65
3	LDI-60-CW, ϕ=0.62	LDI-60-CW	6.633	0.239	0.62
4	LDI-60-CW, ϕ=0.57	LDI-60-CW	6.633	0.220	0.57
5	LDI-60-CW, cold	LDI-60-CW	6.633	0	0
6	LDI-45-CW, ϕ=0.85	LDI-45-CW	6.633	0.327	0.85
7	LDI-45-CW, ϕ=0.80	LDI-45-CW	6.633	0.308	0.80
8	LDI-45-CW, ϕ=0.70	LDI-45-CW	6.633	0.269	0.70
9	LDI-45-CW, ϕ=0.65	LDI-45-CW	6.633	0.251	0.65
10	LDI-45-CW, ϕ=0.62	LDI-45-CW	6.633	0.239	0.62
11	LDI-45-CW, cold	LDI-45-CW	6.633	0	0

As shown in Table 3-1, there are four reacting conditions for the LDI-60-CW configuration, which represent four different flame structures with 60° OAS. As shown later, the LDI-45-CW configuration exhibits only one type of flame structure. Five reacting conditions are tested to observe the responses as the flame of the LDI-45-CW configuration approaches lean blowout limit. To compare directly between the two OAS vane angles, three reacting conditions and a non-reacting (cold) condition are identical for both LDI configurations.

3.3 Results and Discussion

3.3.1 Flame responses and LBO limits

As is evident from the mean flame images presented in Figure 3-1, at 3% pressure drop, several different flame modes are apparent as overall equivalence ratio is reduced towards LBO. It is noted that the origin of the coordinate system is located at the center of the venturi throat. In addition, the configuration of the swirl-venturi LDI mixer is shown in Figure 3-1 to help visualize the flame and flow fields. For the LDI-60-CW configuration, at a relatively high overall equivalence ratio of ϕ=0.85, a vigorously-burning flame is anchored at the venturi exit, with burning zones in both the corner recirculation zones (CNRZs) and center recirculation zone (CRZ), where the mean axial velocities are in the negative x-direction (as also shown by mean axial velocity contours later in Figure 3-4). It should be mentioned that due to their small size and location near the chamber corners, the CNRZs in the LDI-60-CW configuration are not clearly captured by the current PIV results. However, a zoomed-in test intended to characterize the flow field near the chamber corner, which is not shown here, captures the CNRZ in the LDI-60-CW configuration. The most intense burning region appears to be the low velocity region just outside the CRZ at 2–4 D_t downstream of the dump plane. As overall equivalence ratio is reduced to ϕ=0.65, the CNRZ flames disappear and the overall flame structure appears similar, while the flame extends further downstream relative to the LDI-60-CW, ϕ=0.85 case. As equivalence ratio is further reduced (LDI-60-CW, ϕ=0.62), the flame weakens further and detaches from the venturi flare, instead anchoring within the tail of the CRZ near the axial centerline. Finally, as the equivalence ratio approaches LBO, the flame weakens and spreads further downstream until flame lift-off is observed (LDI-60-CW, ϕ=0.57). Further reductions in overall equivalence ratio beyond this point result in the flame exiting the chamber (i.e., LBO).

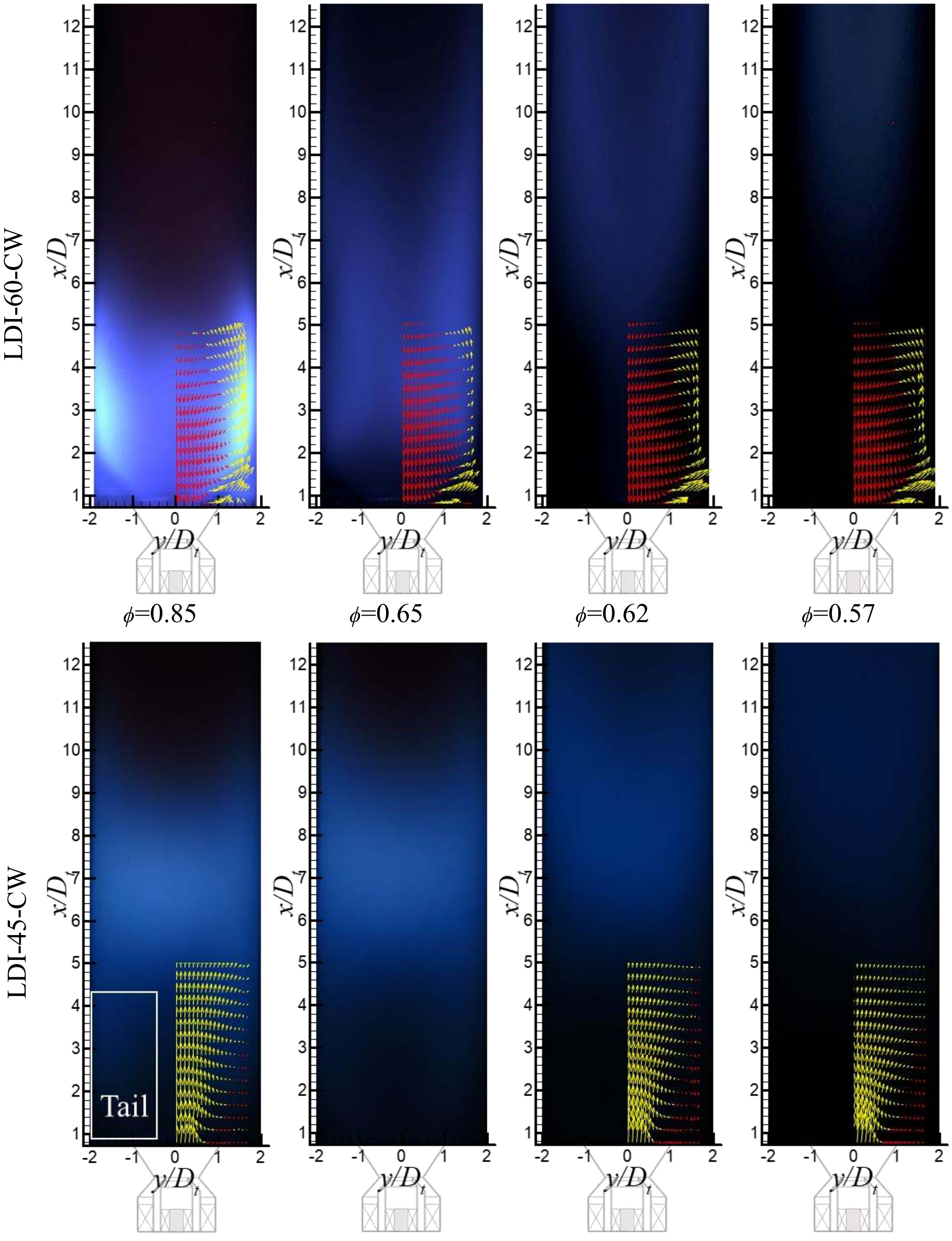

ϕ=0.85 ϕ=0.65 ϕ=0.62 ϕ=0.57

ϕ=0.85 ϕ=0.80 ϕ=0.70 ϕ=0.65

Figure 3-1. Flame structure variations at 3% pressure drop as approaching LBO for LDI-60-CW (top) and LDI-45-CW (bottom), represented by averaged direct flame images and mean *U*-*V* vector maps. Yellow vectors represent positive mean axial velocities, and red vectors show negative mean axial velocities. (Note: the velocity measurement for the LDI-45-CW, ϕ=0.80 case was not conducted.) The text box "Tail" represents the flame tail.

Figure 3-1 also illustrates the flame location variations as a function of overall equivalence ratio for the LDI-45-CW configuration. The LDI-45-CW configuration exhibits very different flame structure from the LDI-60-CW configuration; specifically, under high equivalence ratio conditions the flame does not anchor at the venturi flare but instead is lifted at some distance downstream of the dump plane, with no particular coherent structure. As equivalence ratio is lowered for this configuration, no dramatic structural changes are observed visually, but instead the flame weakens, elongates, and stabilizes further downstream. Figure 3-2 further shows consecutive flame images of the LDI-45-CW, ϕ=0.70 case, representative of the LDI-45-CW flames. Instead of being steadily anchored at one location, the flame exhibits substantial movement both axially and radially. In particular, the flame within the corner zones appears to rotate circumferentially around chamber, resulting in the two “tails” of flame reaching down towards the dump plane in the mean image for the LDI-45-CW, ϕ=0.85 case in Figure 3-1. It is also observed during experiments that the flame movement becomes more vigorous at lower overall equivalence ratios.

Figure 3-3 plots the LBO limits of each configuration as a function of overall pressure drop. While following a roughly similar increasing trend as pressure drop increases, the LDI-60-CW configuration consistently blows out at lower overall equivalence ratios. Taken together with the visual flame observations of Figures 3-1 and 2, the greater OAS vane angle – and thus more highly-swirling flow – of the LDI-60-CW configuration results in a flame that is better anchored to the dump plane and exhibits improved LBO performance relative to the LDI-45-CW configuration.

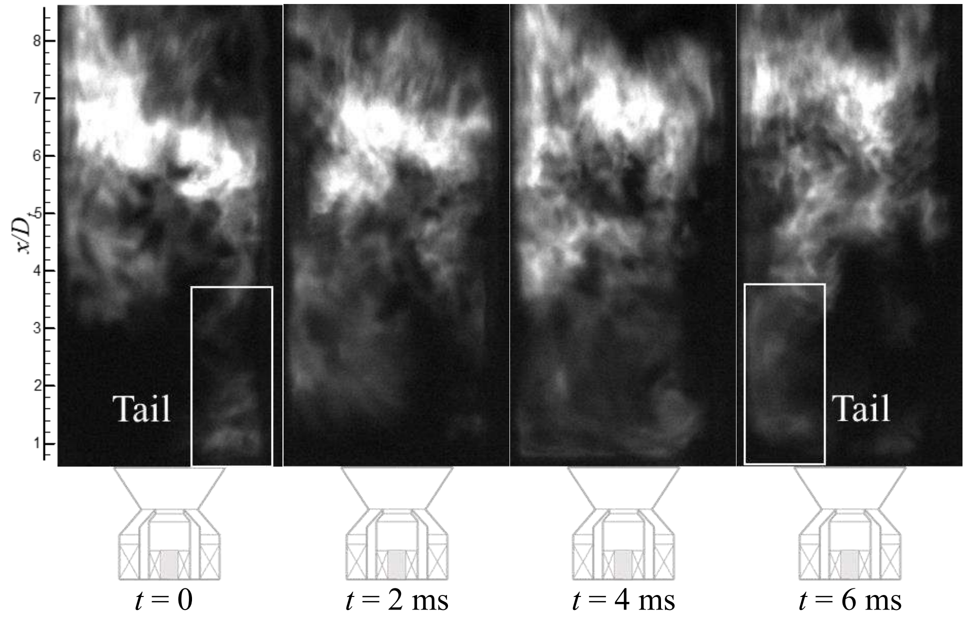

Figure 3-2. Consecutive flame direct images of LDI-45-CW, ϕ=0.70. The text box “Tail” represents the flame tail.

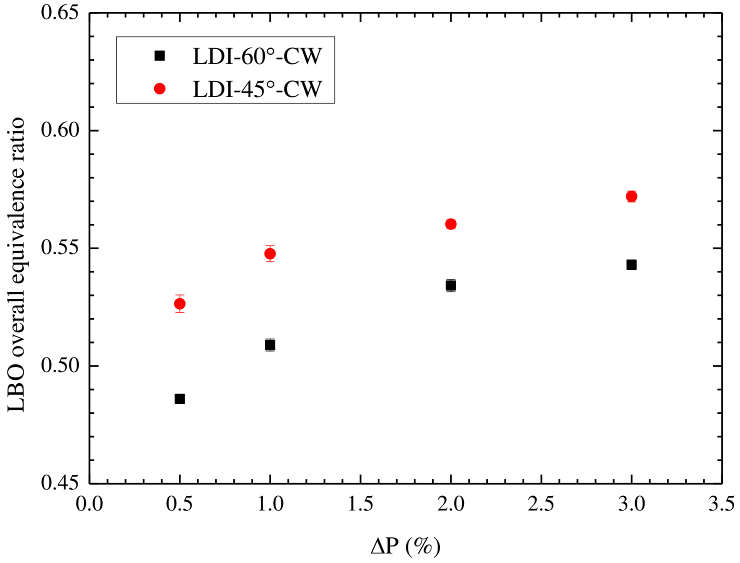

Figure 3-3. Impacts of OAS vane angle on lean blowout limits. The error bars represent the standard deviation at each LBO test condition.

To help explain the source of the differences between the two configurations in reacting flows, the mean axial velocity contours obtained from TR-PIV measurements are presented in Figure 3-4. For the 3% pressure drop condition, the axial velocity contours in the LDI-60-CW configuration exhibit a strong center recirculation zone near the venturi exit that convects burned products upstream towards the venturi flare. For LDI-45-CW, no such CRZ is found in the flow field. Instead, the axial velocity at the exit of the venturi is strongly positive; this feature is termed a swirling jet hereafter. This swirling jet has a maximum mean axial velocity at the flare exit, which progressively weakens as the flow moves downstream. Additionally, this flow results in corner recirculation zones – which are both smaller and weaker compared to the CRZ – at the dump plane corners of the combustion chamber. As overall equivalence ratio decreases, the size of the CNRZs tends to shrink, thus providing even less opportunity for combustion.

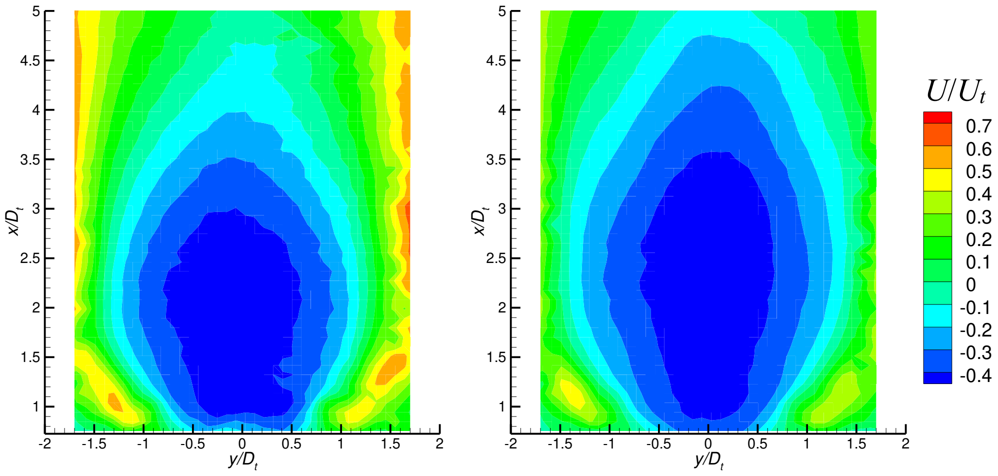

LDI-60-CW, ϕ=0.85 LDI-60-CW, ϕ=0.65

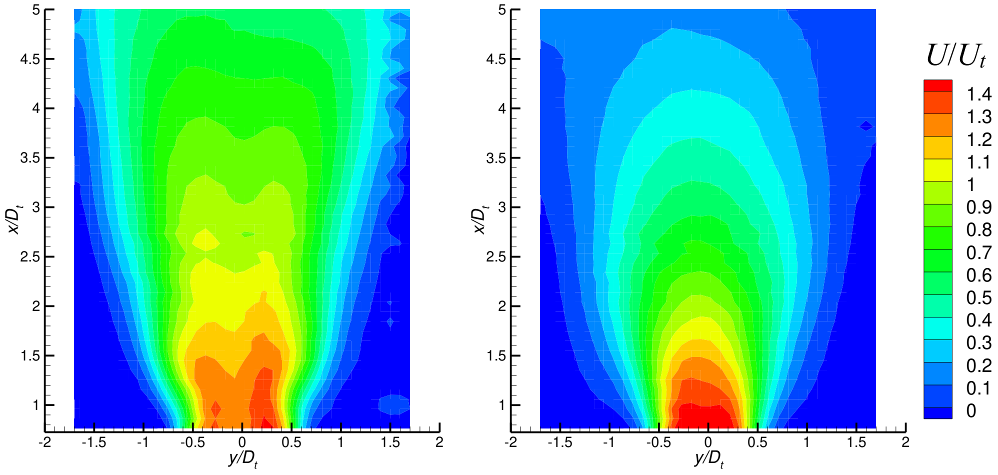

LDI-45-CW, ϕ=0.85 LDI-45-CW, ϕ=0.65

Figure 3-4. Mean reacting flow fields of LDI-60-CW (top) and LDI-45-CW (bottom) at 3% pressure drop.

It is clear from the above results that the degree of swirl is responsible for the disparate flame response and velocity field results between the LDI-60-CW and LDI-45-CW configurations. Swirl Number (*SN*) is routinely used to characterize swirl strength, and represents a non-dimensional ratio between the axial fluxes of angular and axial momenta, as shown in Eq. 3-2:

$$SN = \frac{\int \rho W U r \, \mathrm{dA}}{R \int \rho \, U^2 \mathrm{dA}} \tag{3-2}$$

where W is the mean tangential velocity, r is the radial direction, and R is the radius of the swirler outer boundary. Due to the difficulty in accurately measuring the velocity field at the flare exit, the *SN* based on the flow through the OAS or IAS is estimated from the simplified *SN* equation expressed below,

$$SN = \frac{2}{3}\left[\frac{1-(R_h/R_n)^3}{1-(R_h/R_n)^2}\right]\tan\theta \tag{3-3}$$

where θ is the swirler vane angle and R_h and R_n are the radii of swirler's inner and outer boundaries, respectively. Based on the current swirler's geometry, the LDI-60-CW configuration's OAS has a *SN* valued at 1.41, while the LDI-45-CW configuration's OAS has a *SN* valued at 0.82. The same IAS is used in both LDI configurations, and it has a *SN* valued at 1.30. While it is important to note that the IAS swirling direction is the opposite of the OAS swirling direction, since the air flow through the OAS is approximately three times that through the IAS, the overall swirl strength will be dominated by the OAS, and thus swirl strength of the total flow here is compared by the *SN* of the OAS. As such, the LDI-60-CW configuration exhibits an overall swirl strength nearly twice that of the LDI-45-CW configuration. Gicquel et al. pointed out that when swirling strength is sufficiently large, vortex breakdown occurs, resulting in an adverse pressure gradient and a CRZ [68], which is consistent with the phenomenology observed in the LDI-60-CW configuration. Conversely, with weaker swirl strength only long, weak CNRZs are formed at corners of the combustion chamber near the dump plane from the secondary flows induced by the high-speed swirling jet.

In addition to velocity field information, Figure 3-5 plots and compares the OH-PLIF signal distributions in the two LDI configurations, at the condition of ϕ=0.65. In the LDI-60-CW configuration, the reaction zone closely follows the geometry of the CRZ. Moreover, OH radicals are present within the CRZ, and are especially strong in the surrounding high shear regions where the recirculated product gas in the CRZ meets fresh reactants. In contrast, the LDI-45-CW configuration shows only weak OH-PLIF signal within the CNRZs for the same equivalence ratio condition.

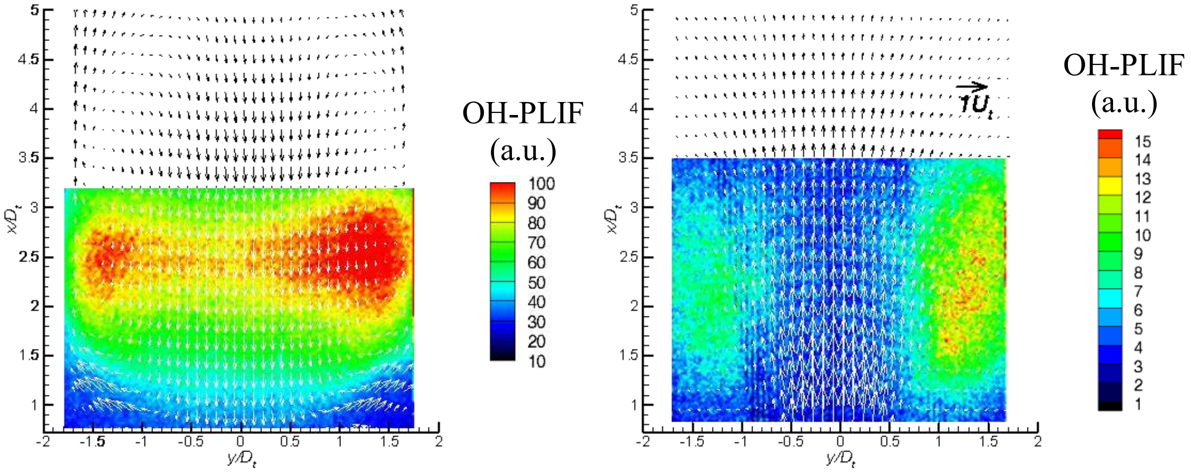

LDI-60-CW, ϕ=0.65 LDI-45-CW, ϕ=0.65

Figure 3-5. Comparison of OH-PLIF contours and mean *U*-*V* vector maps between LDI-60-CW (left) and LDI-45-CW (right) at the same conditions of 3% pressure drop and ϕ=0.65. The units of OH-PLIF signal intensity are arbitrary units (a.u.).

The purpose of visualizing radical species distributions in the present work is to provide a basis for qualitative comparisons between cases and between the mean velocity field structure and the resultant overall flame structure. Due to the relatively large size of the flame in the present experiment, the full flame structure cannot be captured from a single frame of OH-PLIF measurement due to limited laser power. As a result, OH* and CH* chemiluminescence images are used instead in the remainder of this discussion to characterize the flame structure and reaction intensity.

OH* and CH* chemiluminescence measurements are performed to better delineate overall reaction zones and compare reaction intensity amongst the various test cases. Time-averaged radical fields are overlaid with the mean axial-radial velocity vectors in Figure 3-6. As was observed from the visual flame images, in the LDI-60-CW configuration the CRZ results in a reaction zone anchored to the venturi flare. Specifically, at high overall equivalence ratios (ϕ=0.85), high radical concentrations are observed in the high shear/low velocity region between the CRZ and CNRZs in the region between x/D_t=0–4, where unburned reactants exiting the flare meet hot recirculated gases. As overall equivalence ratio drops (ϕ=0.62) however, the heat release in the region between x/D_t=0–4, where high shear region is located, is apparently insufficient to sustain reactions in this zone. As a result, the flame stabilizes downstream in the low velocity, post-CRZ region, remaining anchored to the low-velocity downstream tail of the CRZ.

In contrast, the LDI-45-CW flames are consistently stabilized far downstream of the swirling jet, where expansion of the jet and the resultant reduced velocity allow a flame to be sustained. As the flame weakens when the overall equivalence ratio approaches LBO (ϕ=0.65), the reduction in reactivity necessitates a stabilization point further downstream at a region where mean velocity is lower. Recalling the unsteadiness of the flames for this configuration (cf. discussion of Figure 3-2), such behavior can be explained by the lack of a well-defined, steady aerodynamic stabilization feature (e.g., the CRZ). For this configuration, the flame location is dictated purely by a local balance between flame propagation and the velocity of the turbulent, swirling jet flow; as a direct result it is unsurprising that the flame location demonstrates unsteadiness commensurate with the unsteadiness of the underlying turbulent flow.

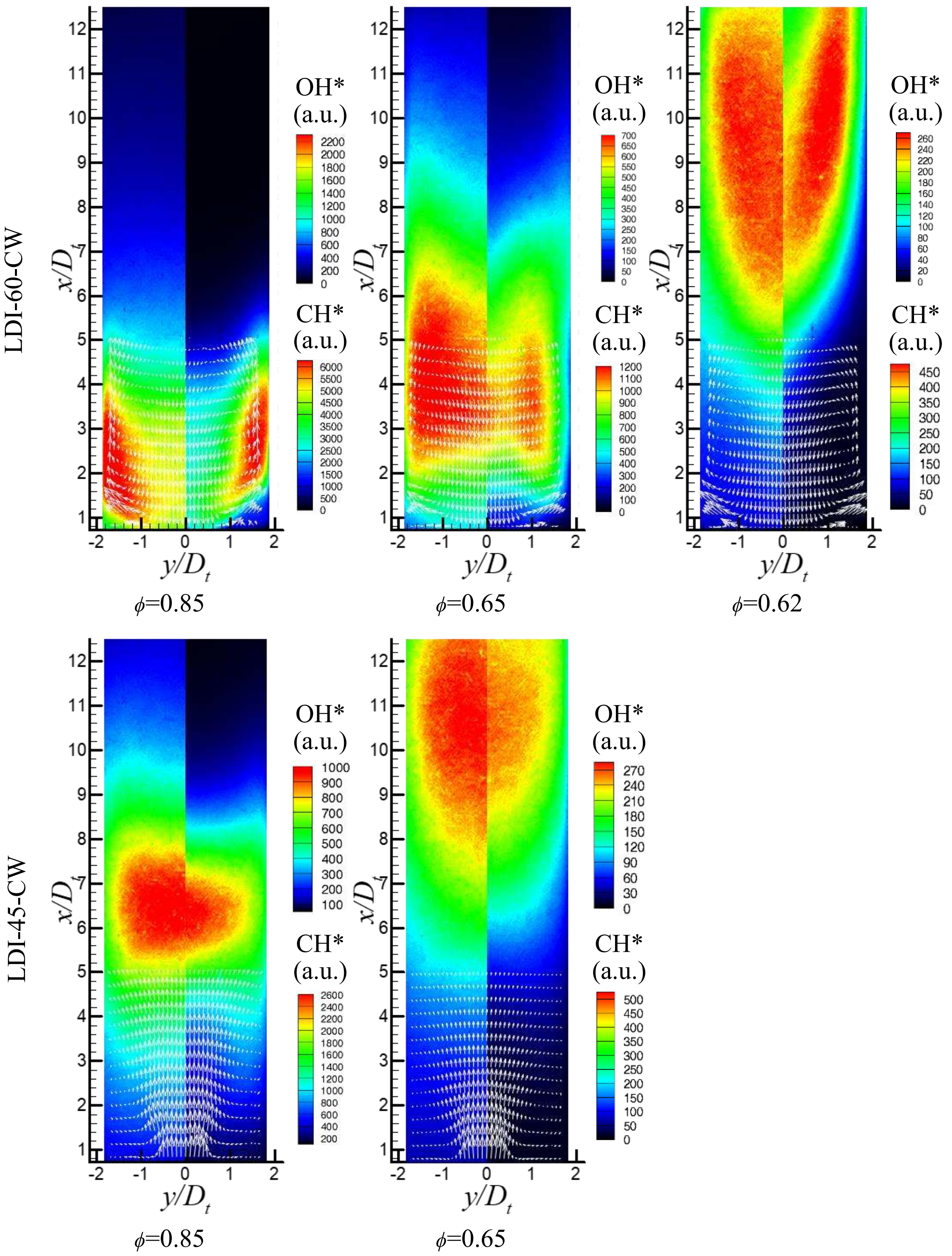

Figure 3-6. Time-averaged OH* (left) and CH* (right) overlaid with mean velocity vectors at 3% pressure drop and varying overall equivalence ratios for the LDI-60-CW (top) and LDI-45-CW (bottom) configurations. The units of OH* and CH* signal intensities are arbitrary units (a.u.).

From these mean velocity vectors and radical contours shown in Figure 3-6, it is also apparent why the LDI-60-CW and LDI-45-CW configurations exhibit different LBO limits. Whereas the flame may remain at least partially anchored by minor recirculation within the low-velocity tail of the CRZ in the LDI-60-CW configuration, in the LDI-45-CW configuration the lack of a steady stabilization feature implies stabilization solely by the aforementioned flame propagation/local velocity balance, and thus higher LBO limits. This difference in flame stabilization mechanism is more apparent when comparing the mean centerline axial velocity profiles shown in Figure 3-7 as a function of overall equivalence ratio. While the CRZ weakens for the LDI-60-CW configuration as equivalence ratio drops due to the reduction in thermal expansion – and the commensurate velocity gains – near the CRZ base, a negative velocity is nonetheless maintained along the axial centerline for a substantial distance from the dump plane, only reaching a stagnation condition ~5 D_t downstream. In contrast, the LDI-45-CW configuration exhibits solely positive velocity along the centerline, decreasing steadily as distance from the dump plane increases. The lack of recirculation of burned products in the LDI-45-CW implies that the flame location is determined almost entirely by local flame propagation, and as a result the flame may only exist in the low velocity regions far downstream of the dump plane, with only minor anchoring at elevated equivalence ratios associated with the low-velocity CNRZs.

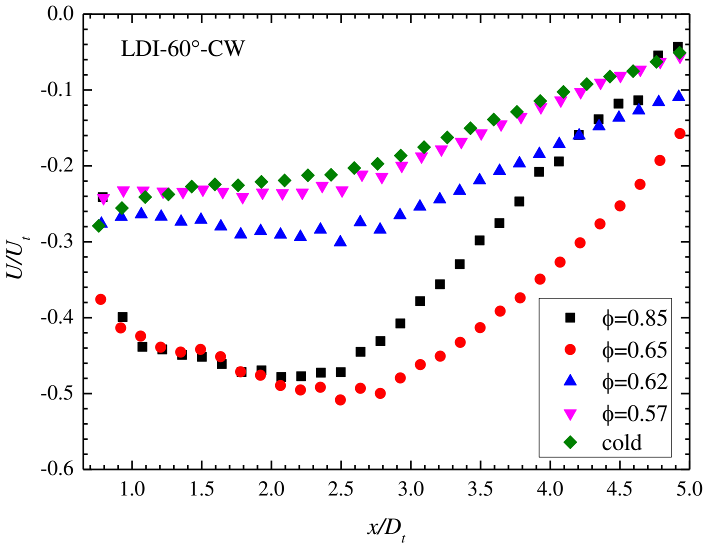

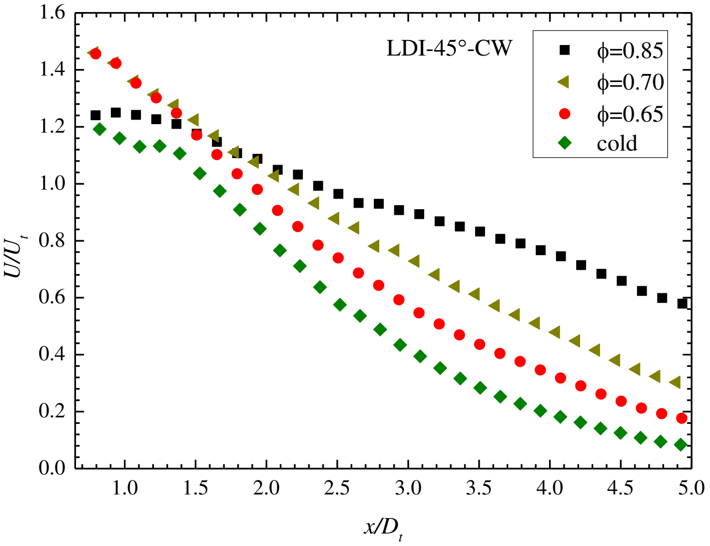

Figure 3-7. Centerline mean axial velocity profiles of LDI-60-CW (top) and LDI-45-CW (bottom) at 3% pressure drop and varying overall equivalence ratios.

3.3.2 Unsteadiness in flow field and flame structure

One potentially important feature of a given flow field that impacts both mixing and flame stabilization is the level of turbulence experienced. Figure 3-8 compares the scaled turbulent kinetic energy (TKE) of the non-reacting (cold) flow fields for the LDI-60-CW and LDI-45-CW configurations. It is worth noting that, given the two-dimensional nature of the TR-PIV measurements, the out-of-plane velocity fluctuation is not captured. While it is recognized that the out-of-plane velocities may be significant in a swirling flow, the magnitude of the differences between the two cases is sufficiently large that it is presumed the out-of-plane fluctuations are unlikely to alter the comparison seen here. Specifically, the highest (two-dimensional) scaled TKE in the LDI-60-CW configuration is found to be ~0.1, located between the shear layers and the dump plane. In contrast, the scaled TKE (*k*) in CRZ is an order of magnitude lower at 0.02 or less. Comparing this plot to the results of Figure 3-6, it is apparent that for the LDI-60-CW case the flame is stabilizing in a region of very low scaled TKE. Observing the results for the swirling jet of the LDI-45-CW configuration, much higher scaled TKE levels (on the order of 0.2–0.3) are observed in the near-dome region, and over a much larger spatial region, reaching ~5 D_t downstream before the TKE dissipates to the maximum levels observed in the LDI-60-CW configuration. Although the low-TKE zones are located in the CNRZs, these regions are quite small relative to the volume contained within a typical CRZ.

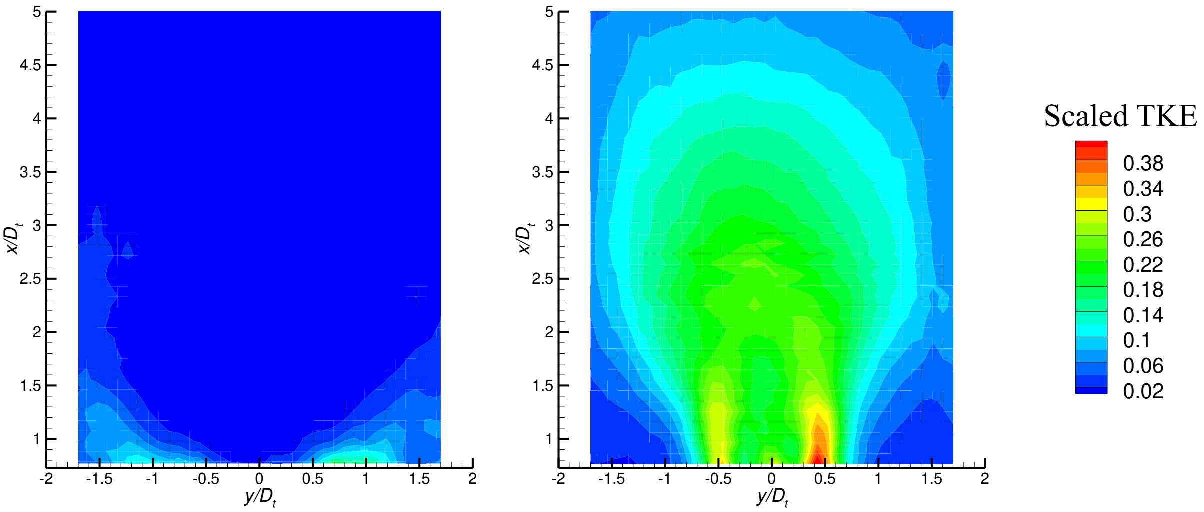

LDI-60-CW, cold

LDI-45-CW, cold

Figure 3-8. Scaled TKE contours of LDI-60-CW, cold (left) and LDI-45-CW, cold (right) cases at 3% pressure drop.

Figures 3-9 and 10 compare the standard deviation of flame intensity (left halves) with scaled TKE (right halves) for two overall equivalence ratios for the LDI-60-CW and LDI-45-CW configurations, respectively. In these plots, as the exposure time varies between the various tests due to large luminosity differences between the cases, all values are linearly scaled to a 1 ms exposure time – i.e. a 0.5 ms exposure time case is scaled by multiplying a factor of 2. In both figures, it is apparent that most of the flame fluctuations occur in regions where the scaled TKE is low – within the CRZ for the LDI-60-CW cases and after expansion of the swirling jet in the LDI-45-CW cases. This may suggest that, in conjunction with the high velocities in these regions, the high turbulence levels inhibit flame stabilization. In addition, as overall equivalence ratio drops in both Figures 3-9 and 10 the fluctuation in flame intensity also drops, likely indicative of the reduced heat release as the fuel-air mixture becomes leaner. This difference is most dramatic in the LDI-60-CW cases, where the standard deviation of intensity drops by a factor of ~5, despite their very close overall equivalence ratios (ϕ=0.65 and 0.62) when the flame transitions from a flare-stabilized flame to a CRZ tail-stabilized flame. In contrast, for the LDI-45-CW cases with a larger difference in overall equivalence ratio, ϕ=0.7 versus 0.65, the disparity in flame intensity standard deviation is approximately a factor of two, dropping from a maximum of ~0.8 for ϕ=0.7 to ~0.4 for ϕ=0.65.

It is worth noting that one area not explored experimentally in the present work that may be improved by regions of high TKE is liquid droplet breakup and vaporization. Airblast swirl injectors – such as those used in the present study – rely upon high shear in order to drive sufficiently fast fuel droplet breakup, and thus the regions of high TKE near the dump plane for the LDI-45-CW configuration may be more beneficial for liquid-fueled operation. Conversely, the lower levels of TKE in the LDI-60-CW configuration may aid in flame stabilization but provide little help in the breakup and vaporization of liquid fuel, suggesting that a tradeoff may exist between improved fuel atomization and enhanced flame stabilization. This hypothesis will be explored in future work.

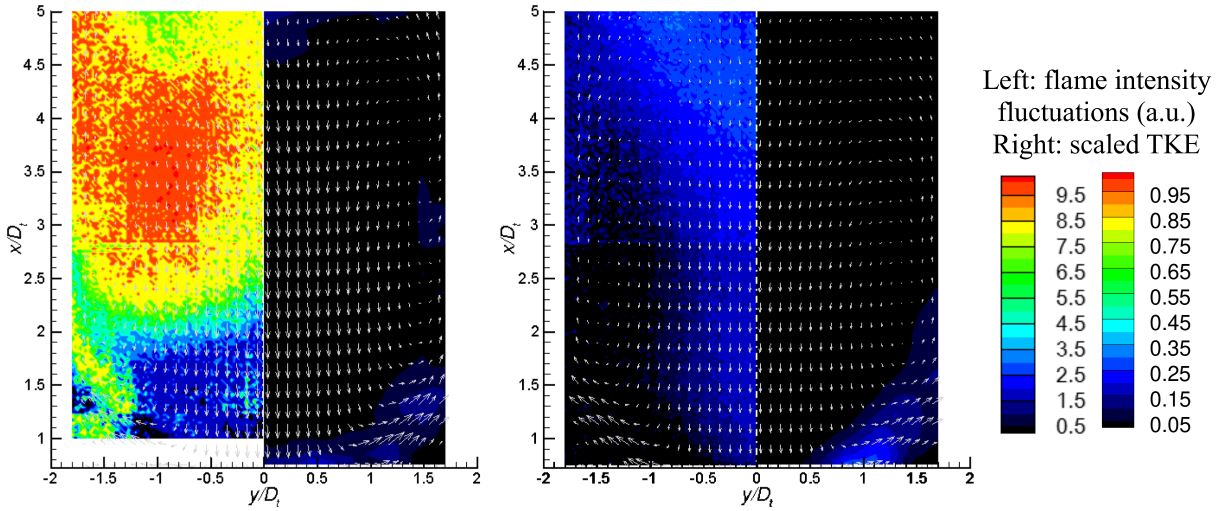

LDI-60-CW, ϕ=0.65 LDI-60-CW, ϕ=0.62

Figure 3-9. Flame intensity fluctuations (left halves) and scaled TKE (right halves) overlapped by mean *U*-*V* vectors for LDI-60-CW, ϕ=0.65 and ϕ=0.62 cases at 3% pressure drop. The units of flame intensity fluctuations are arbitrary units (a.u.).

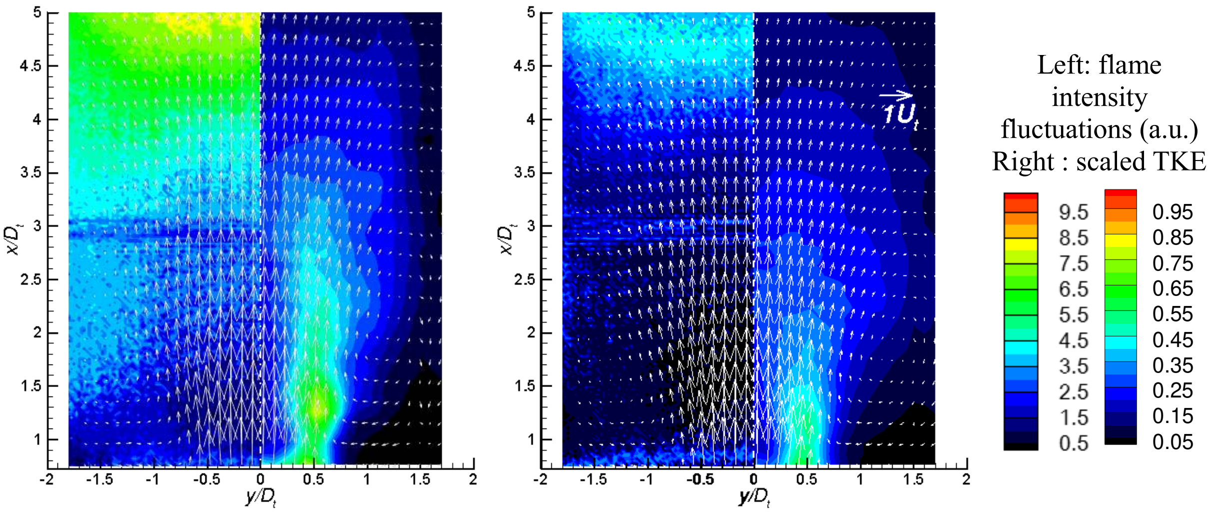

LDI-45-CW, ϕ=0.70 LDI-45-CW, ϕ=0.65

Figure 3-10. Flame intensity fluctuations (left halves) and scaled TKE (right halves) overlapped by mean *U*-*V* vectors for LDI-45-CW, ϕ=0.70 and ϕ=0.65 cases at 3% pressure drop. The units of flame intensity fluctuations are arbitrary units (a.u.).

3.3.3 NO_2* chemiluminescence comparison

The LDI concept is, at its core, concerned with reducing NO_x emissions while maintaining or exceeding the combustion efficiency and operability performance of existing fuel injection designs.

As a result, an effort has been made here to qualitatively identify differences in NO_x production as a function of both operating conditions and OAS vane angle. In the present effort, NO_2* chemiluminescence is used as a proxy for overall NO_x production, recognizing that while this method does not allow for a quantitative measurement of NO_x from each configuration, it does provide spatial distribution information valuable to the present analysis.

Figure 3-11 compares NO_2* distributions from the two LDI configurations at ϕ=0.65 and ϕ=0.62 conditions for 3% pressure drop. It is immediately apparent that the LDI-60-CW, ϕ=0.65 case – corresponding to a venturi flare-anchored flame – produces comparatively the most NO_2*, with significant chemiluminescence along the axial centerline starting within the CRZ at 0.5 D_t downstream of the dump plane and continuing downstream to 11–12 D_t. This distribution corresponds to the interior of the CRZ and the low velocity regions immediately following it, suggesting that the CRZ, while providing a strong anchoring location for the flame, also locally provides sufficient residence time for thermal NO_x to develop. As overall equivalence ratio drops to ϕ=0.62, the flame stabilization location moves downstream to the low-velocity region immediately following the CRZ – a "lifted" flame – and the overall NO_2* signal drops by almost half. In fact, despite a slightly different flame structure, the LDI-60-CW, ϕ=0.62 case and the LDI-45-CW, ϕ=0.65 and 0.62 cases exhibit roughly similar NO_2* signal, suggesting similar overall NO_x production. The lifted-flames of the LDI-45-CW, ϕ=0.65 and 0.62 cases themselves are also remarkably similar in form, although the LDI-45-CW, ϕ=0.62 case shows 10–20% lower peak values relative to the LDI-45-CW, ϕ=0.65 case due to lower overall equivalence ratio and thus reduced bulk flame temperatures. Taken together, the results of Figure 3-11 suggest that, regardless of specific OAS angle, NO_x production within the LDI configuration may be largely driven by the flame primary zone location relative to long residence time streamlines. This further indicates that operability and NO_x emissions may be in direct competition, requiring conscious design tradeoffs for practical LDI applications.

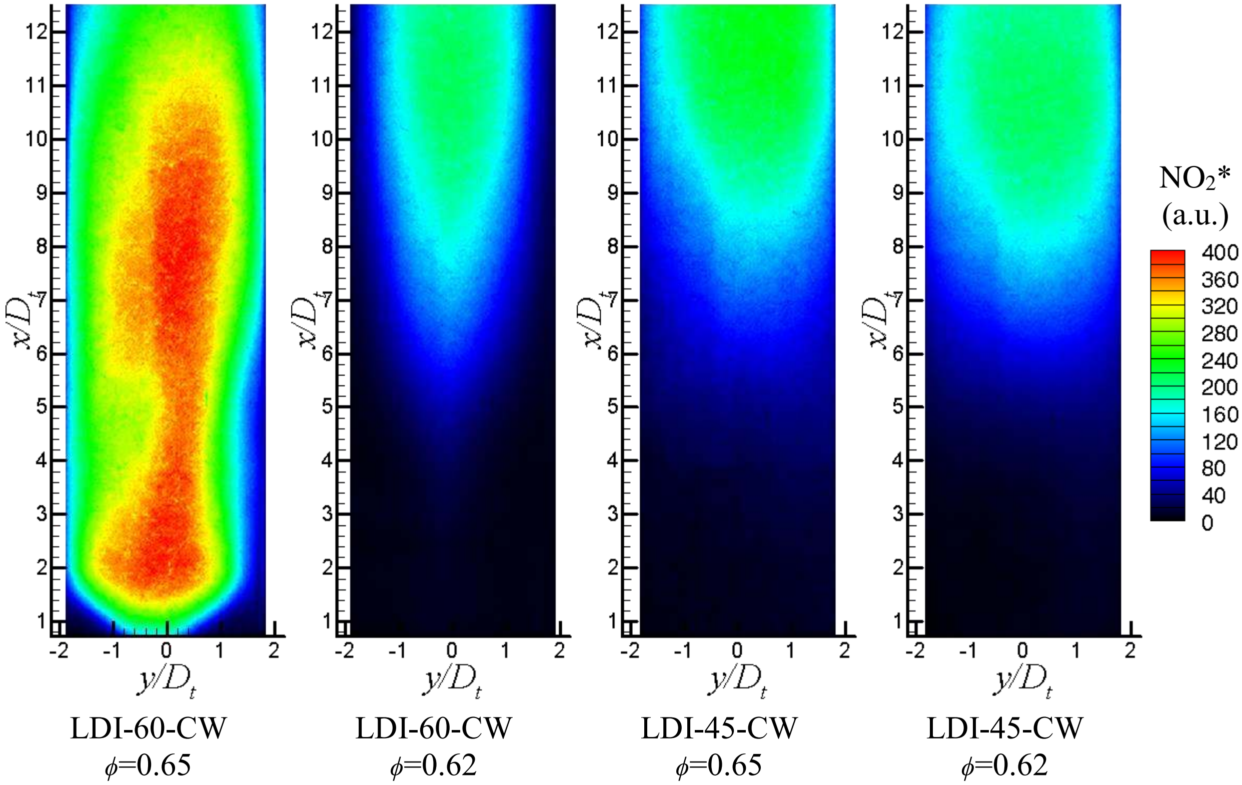

LDI-60-CW ϕ=0.65 LDI-60-CW ϕ=0.62 LDI-45-CW ϕ=0.65 LDI-45-CW ϕ=0.62

Figure 3-11. Comparison of NO_2* chemiluminescence contours at 3% pressure drop and varying overall equivalence ratios. The units of NO_2* signal intensity are arbitrary units (a.u.).

3.4 Concluding Remarks

A systematic fundamental research effort has been carried out using advanced diagnostic techniques to provide insights into the impact of outer air swirler vane angle on the flame response, lean blowout limits, and NO_x emission levels for a representative LDI configuration. As would be expected, the swirl strength as a function of swirler vane angle plays an important role in determining the LDI performance. The creation of strong or weak swirl flow via variation of the OAS vane angle demonstrates that increasing tangential velocities creates a center recirculation zone (CRZ) that aids in stabilization of the flame. The presence of this CRZ promotes flame stabilization near the swirler dump plane, while its absence results in a detached flame located well downstream of the venturi flare. Moreover, the reverse flow inherent to the CRZ assists the LDI-60-CW configuration in terms of lower LBO limits relative to the LDI-45-CW configuration. Commensurate with the observations by Tacina et al. [33], reducing the OAS vane angle to 45° in the LDI-45-CW flame results in apparently much lower NO_x emissions. This is likely due to overall shorter residence times and stronger TKE near dome region. Similar results may be obtained under lower overall equivalence ratio operating conditions for the LDI-60-CW configuration, where the flame becomes lifted from the venturi flare. Taken together, these observations suggest that a fundamental design tradeoff may exist between low NO_x emissions and overall operability. As a result, optimization of the OAS vane angle is likely necessary to maintain sufficient swirl number to generate a CRZ for improved operability and meanwhile minimizing overall CRZ residence time for emissions reduction.

CHAPTER 4 THE IMPACT OF FLARE SECTION ON LDI PILOT MIXERS' OPERABILITY, EMISSIONS, AND DYNAMICS

4.1 Introduction

The demand for improved thermal efficiency and thrust in aero engines results in increased overall pressure ratio (OPR) and commensurately higher turbine entry temperature (TET). However, these higher OPRs and TETs have the side effect of increased production of thermal NO_x due to the higher peak operating temperatures achieved. To meet the stringent aviation NO_x emission standards, the lean combustion technologies for gas turbine engines have been proposed, such as lean direct injection (LDI). The LDI combustion was found to significantly reduce NO_x productions by using swirl injectors and operating at lean conditions throughout combustors.

A series of studies investigating such multi-point designs have been conducted to demonstrate the impacts of swirler vane angle, injector configuration, and multi-point layout on the operability [27], emissions [27,30,31], spray and flame structure [32], and combustion dynamics [33]. Test results showed that optimizing the swirler-venturi injector configuration could influence LDI operability and emissions significantly, indicating that the specific design features of the LDI air swirler/fuel injector assemblies are critical to the combustor performance. Thus, systematic studies on the fundamental behavior of the individual swirl-injector are necessary to understand and predict the performance of the system as a whole, motivating a series of comprehensive studies of the second generation SV-LDI configuration.

Each second generation SV-LDI configuration consists of an airblast injector, axial swirlers, and a venturi. The converging-diverging venturi combined with the swirlers is designed to optimize atomization performance via aerodynamic breakup. Specifically, the converging section of the venturi assists atomization of the fuel by increasing the speed of the air stream near the fuel tip, while its diverging section – also referred to as a flare – is designed to recover pressure head and enhance fuel-air mixing. In general, the addition of a venturi to a simple swirl injector has been shown to improve atomization and reduce NOx emissions [69]. Im et al. [70] parametrically examined the venturi diverging angle effect on the spray with various swirler vane angles, showing that the interaction between swirler and venturi impacts the resulting spray angles and Sauter mean diameter (SMD) distributions. Wang et al. [71] reported the effect of flare diverging angle on spray structure using a dual-swirler cup, demonstrating that with a larger flare expansion angle, thinner films were formed near the venturi exit and a stronger interaction between the counter-rotating air flows was observed. Li et al. [38] studied the influence of flare height on droplet size distribution using a novel dual-phase airblast injector, but found no significant effect on SMD distribution.

In addition to the venturi's impact on atomization, varying the venturi geometry will also alter the aerodynamics of the flow and thus the nature of the swirling flow field downstream of the venturi. Wang et al. [72] indicated that the flare can influence both the air flow and the spray in that the larger expansion angle contributes to a larger recirculation zone, relatively lower reverse flow velocity, wider droplet dispersion, and larger droplet size distribution. Similarly, Estefanos et al. [73] experimentally investigated the effect of the flare expansion angle on the non-reacting swirling flow. With larger flare angles, both the length and width of the center recirculation zone (CRZ) increased, while the length of the corner recirculation zone (CNRZ) decreased.

In addition to the steady characteristics of the swirling flow and resultant flame structure, the dynamic features of the LDI swirl injector are also critical to overall operability, since inherent flow oscillations are both common and potentially limiting in a practical combustion device [74]. Moreover, these fluctuations may vary for different swirler and combustor configurations or operating conditions such as equivalence ratio, inlet temperature, and pressure. For example, low frequency (<50 Hz) instabilities can occur at lean conditions near lean blowout, while high-frequency (>250 Hz) instabilities are typically caused by the interactions between acoustic disturbances and flame evolution [74–76], and can be relevant for both low- and high-power conditions. Frequency analysis based on time resolved diagnostics are therefore widely employed to explore the combustion instability characteristics of swirling flames, e.g., [77]. Yi and Santavicca [78] carried out a study of combustion instabilities in a liquid-fueled LDI combustor with a frequency analysis based on high-speed pressure measurements and chemiluminescence imaging, showing that two modes of combustion instability could be excited simultaneously. The venturi divergence angle has also been demonstrated [73] to exert significant influence on instabilities in the non-reacting swirling flow, with strong flow instability observed near the unstable shear layers created by the CRZ and CNRZ; the dominant frequency found in this study was slightly lower for the 30.9˚ flare angle than those of 35.9˚ and 40.9˚ flares tested. Such venturi geometry-related instabilities in non-reacting swirling flow can reasonably be expected to lead to similar unstable features in the reacting swirling flow and flames, thus motivating the study of such effects in the present work. Although efforts to describe these effects exist in the literature, the importance of the flare effects on both the swirling flow and resultant flame behavior is still limited [73]. Moreover, the practical impacts of the venturi on SV-LDI injectors at various levels of swirl strength are not well understood.

This chapter aims to address these questions by investigating the performance of LDI-based injectors with and without a flare section on LBO limits, flame behaviors, NO_x emissions, and reacting flow dynamics. In particular, the impact is studied for “weak” and “strong” swirl strength cases by varying OAS vane angle between 45˚ and 60˚, while maintaining IAS vane angle at 60˚ in a counter-rotating configuration. Key non-reacting and reacting flow field features are mapped and characterized using TR-PIV, and important flame features of each flow field are identified by broadband flame and chemiluminescence imaging.

4.2 Experimental Methods

4.2.1 Test facility and injectors

Figure 4-1 shows the geometric structure of the single-element SV-LDI and airblast configurations studied in present work, respectively. For the present study, a counter-rotating swirling flow between IAS and OAS passages is formed by installing 45˚/60˚ OAS vanes at a clockwise (CW) rotation direction, while the IAS vanes are fixed at 60˚ with a counter-clockwise (CCW) rotation. The four configurations used in the present fundamental study are summarized in Table 4-1.

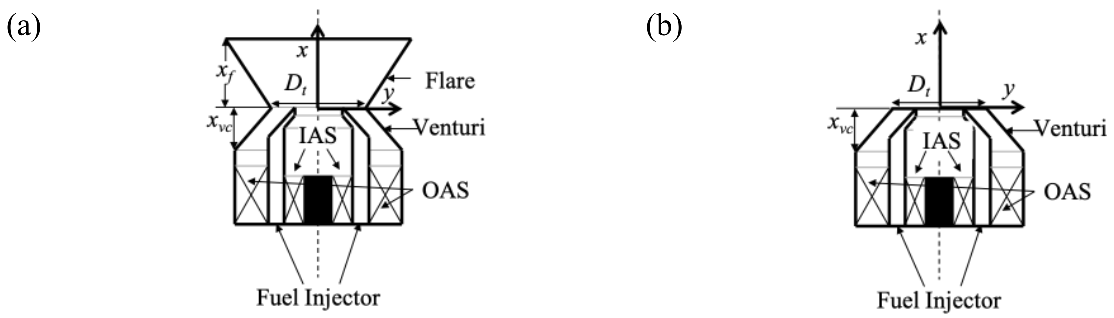

Figure 4-1. Schematics of (a) swirl-venturi LDI mixer, and (b) airblast mixer.

Table 4-1. Configuration specifications of swirlers and venturis here.

Configuration	Swirler (IAS/OAS)	Venturi Geometry
LDI-60-CW	60˚CCW/60˚CW	With flare
Airblast-60-CW	60˚CCW/60˚CW	Without flare
LDI-45-CW	60˚CCW/45˚CW	With flare
Airblast-45-CW	60˚CCW/45˚CW	Without flare

4.2.2 Measurement techniques and operating conditions

Multiple measurement techniques are employed in this work to compare the flow field, flame structure, and emissions performance for the four LDI/Airblast configurations. A two-dimensional

TR-PIV system is used to obtain axial-radial velocity data with the laser sheet aligned with the center plane of the burner. To delineate the reaction regions and qualitatively compare flame intensity and NO_x emissions, OH^*, CH^*, and NO_2^* chemiluminescence signals are imaged using a PI-MAX III ICCD camera, paired with a Nikon 105 mm UV lens. For each test, species-specific bandpass filters are mounted to collect the specific signals. NO_2^* is used here as a proxy indicator for the NO_x emission index, which is the total production of nitric oxide (NO) and NO_2 per unit mass of fuel consumption. For each test case, 100 consecutive individual images at a 10 Hz frame rate are averaged to obtain mean radical distributions. Furthermore, the mean chemiluminescence images are background corrected with the correspondingly filtered average image of the non-reacting flow, correcting for most background luminosity. A 5×5 pixel^2 median filter is also applied to the image to reduce noise.

In order to assess the differences between the LDI and Airblast configurations, as well as analyze their differing performances with altered OAS vane angles, a series of test conditions are chosen that capture representative flame structures as each configuration approaches LBO. Table 4-2 summarizes the operating conditions for each of the experimental cases. In the present work, the total mass flow rate and *Re* are kept approximately constant for each test cases. The air mass flow rate for a pressure drop across the swirler of 3% is kept constant at 6.633 g/s. As such, the *Re* based on the volumetric flow rate and the venturi throat diameter for each test condition is estimated as 35,000. To provide a direct comparison amongst different configurations, at least three reacting conditions and a non-reacting (cold) condition are identical for each of the mixer configurations.

Table 4-2. Test conditions of all four LDI and Airblast configurations.

Configuration	Air flow rate (g/s)	Overall equivalence ratio (ϕ)
Airblast-60-CW	6.633	0, 0.65, 0.68, 0.70, 0.80, 0.85
Airblast-45-CW	6.633	0, 0.65, 0.68, 0.70, 0.80, 0.85
LDI-60-CW	6.633	0, 0.57, 0.62, 0.65, 0.68, 0.70, 0.85
LDI-45-CW	6.633	0, 0.65, 0.68, 0.70, 0.80, 0.85

4.3 Results and Discussion

4.3.1 Flame responses and LBO limits

Figure 4-2 presents and compares mean flame images from the Airblast-60-CW and LDI-60-CW configurations as a function of overall equivalence ratio at 3% pressure drop. It should be mentioned that the origin of the coordinate system is located at the center of the venturi throat for each configuration. In addition, the schematic of the corresponding mixer is shown in each figure throughout this thesis to aid in visualization of the flame structure and flow field. As is immediately evident, the flame structures change dramatically when the flare is removed. For the LDI-60-CW configuration, at ϕ=0.85 the flame is well-defined and seated on the venturi flare. As equivalence ratio is lowered, the flame weakens and elongates downstream, ultimately lifting off the dump plate and stabilizing further downstream as LBO is approached.

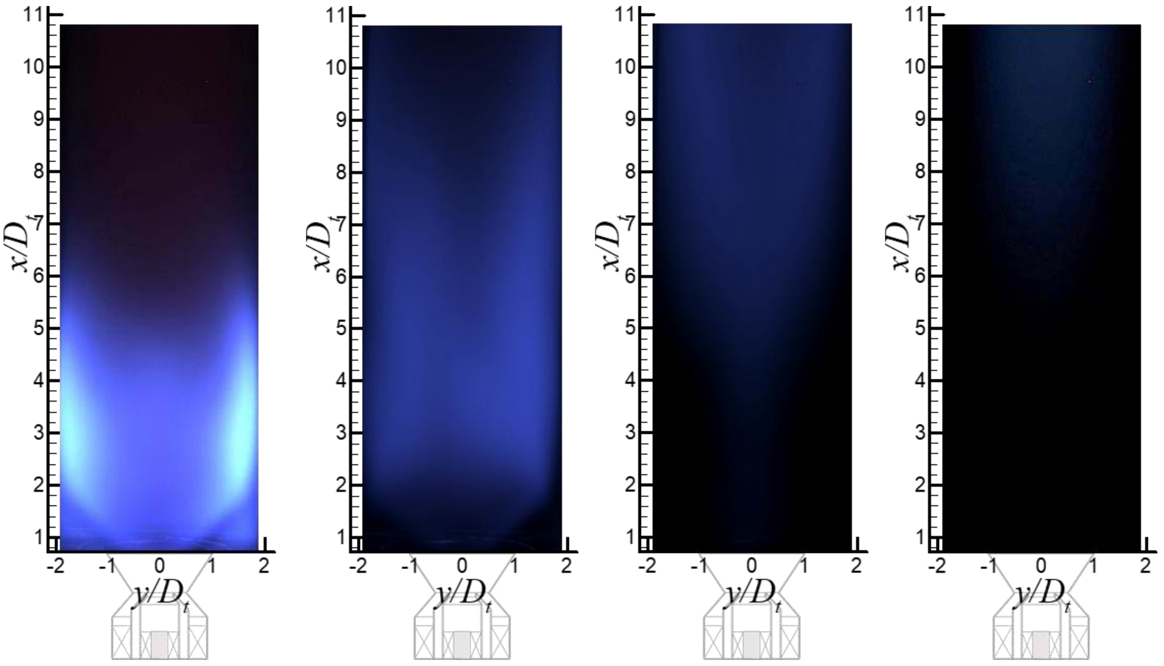

LDI-60-CW ϕ=0.85 | LDI-60-CW ϕ=0.65 | LDI-60-CW ϕ=0.62 | LDI-60-CW ϕ=0.57

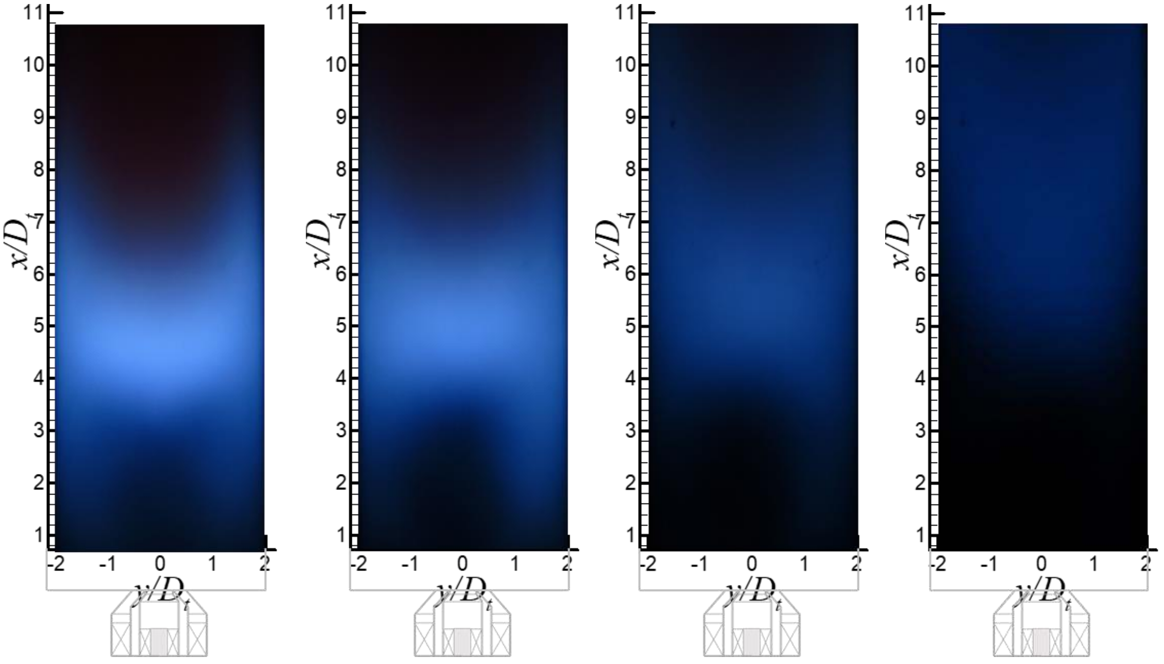

Airblast-60-CW ϕ=0.85 | Airblast-60-CW ϕ=0.80 | Airblast-60-CW ϕ=0.70 | Airblast-60-CW ϕ=0.65

Figure 4-2. Flame structure variations at 3% pressure drop as approaching LBO for LDI-60-CW (top) and Airblast-60-CW (bottom), represented by averaged mean direct flame images.

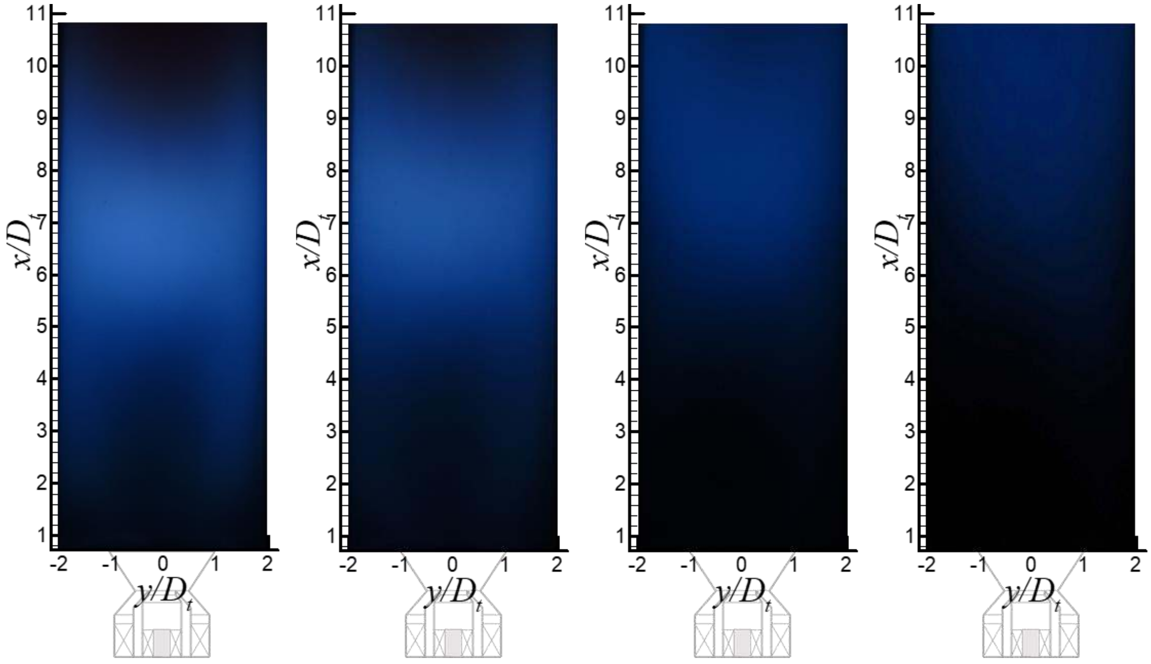

LDI-45-CW ϕ=0.85 | LDI-45-CW ϕ=0.80 | LDI-45-CW ϕ=0.70 | LDI-45-CW ϕ=0.65

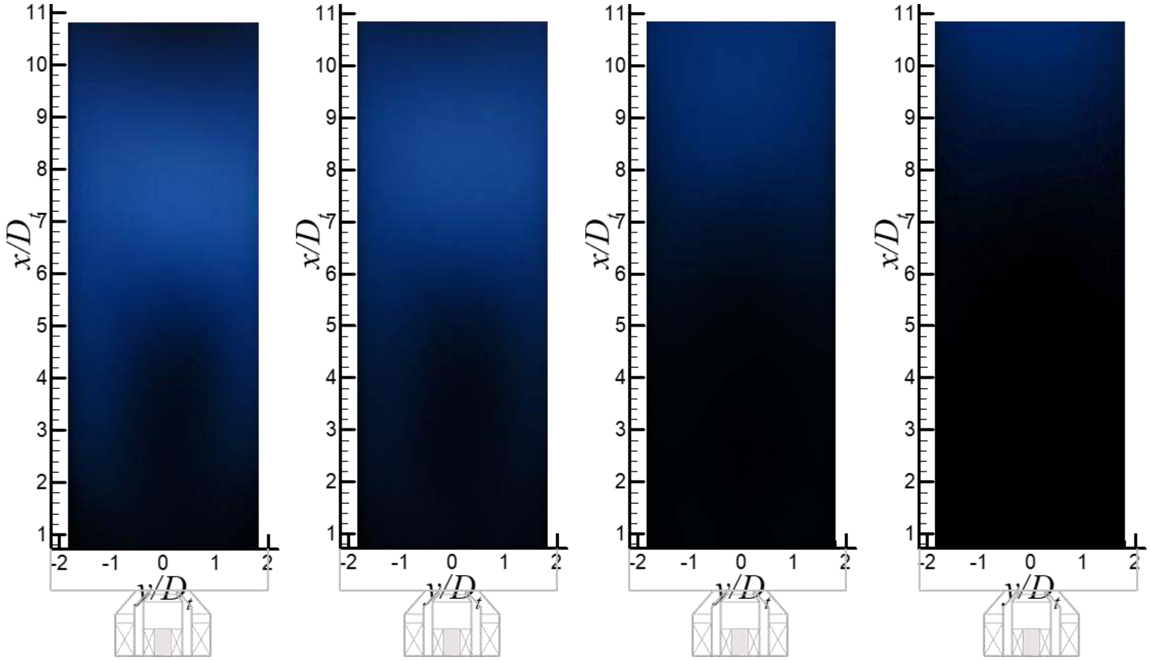

Airblast-45-CW ϕ=0.85 | Airblast-45-CW ϕ=0.80 | Airblast-45-CW ϕ=0.70 | Airblast-45-CW ϕ=0.65

Figure 4-3. Flame structure variations at 3% pressure drop as approaching LBO for LDI-45-CW (top) and Airblast-45-CW (bottom), represented by averaged mean direct flame images.

In contrast, the Airblast-60-CW configuration does not result in a seated flame at ϕ=0.85, and thus does not transition between burning modes as does the comparable LDI configuration. Instead, the flame largely maintains its general shape and weakens, elongates, and stabilizes progressively further downstream as overall equivalence ratio is lowered.

For the 45˚ OAS configurations, as shown by mean flame images in Figure 4-3, the removal of the flare section does not appear to significantly alter the mean flame structure. The flame from the LDI-45-CW configuration burns more vigorously and closer to the dump plate than the flame in the Airblast-45-CW case for the same overall equivalence ratio condition, however in terms of overall flame shape the two configurations result in largely the similar structure.

To better compare the flame locations in the Airblast-60-CW, LDI-45-CW, and Airblast-45-CW configurations, a flame boundary can be defined by using an appropriate threshold – chosen here as 40% of the maximum CH^* signal intensity in each test case – which delineates a flame region similar to that would be observed visually from broadband imagery, as shown in Figure 4-4. Moreover, Figure 4-5 plots the liftoff heights of the flames for ϕ=0.63–0.85, in which the flame liftoff height is defined by the axial location of the lower flame boundary at the chamber centerline relative to the dump plate. As would be expected, as equivalence ratio is lowered, the liftoff height increases and the flame progressively weakens until LBO is reached. In addition, the Airblast-60-CW case exhibits the lowest liftoff height, followed by the LDI-45-CW case, with the Airblast-45-CW configuration showing both the largest liftoff height and by far the greatest liftoff height sensitivity to the equivalence ratio variation. Specifically, removing the flare for the 45˚ OAS vane angle configurations (Airblast-45-CW vs. LDI-45-CW) results in 0.3–2 D_t greater flame liftoff height for the range of ϕ=0.63–0.85, with the largest disparities seen for ϕ=0.7 and below. When the OAS vane angle is increased, for the same overall equivalence ratios the Airblast-60-CW flames locate 1–3 D_t nearer to the dump plate and are more compactly- and vigorously-burning than the corresponding flames of the Airblast-45-CW cases.

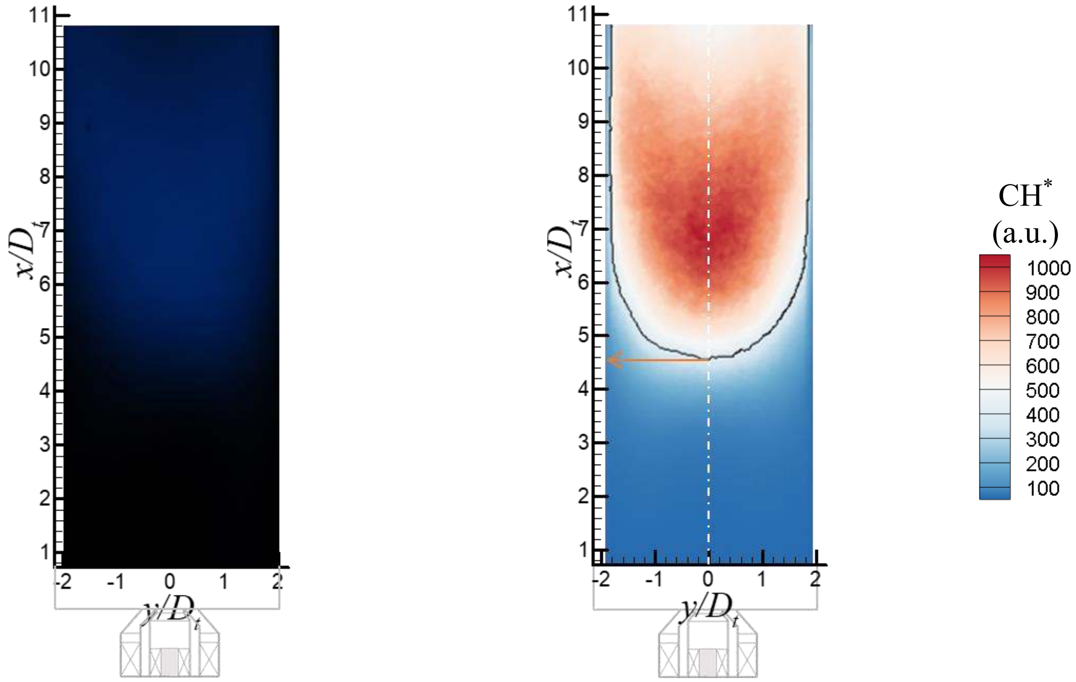

(a) Broadband image (b) CH^* chemiluminescence

Figure 4-4. Flame liftoff height definition from Airblast-60-CW, ϕ=0.65, at 3% pressure drop. CH^* signal is in arbitrary units (a.u.).

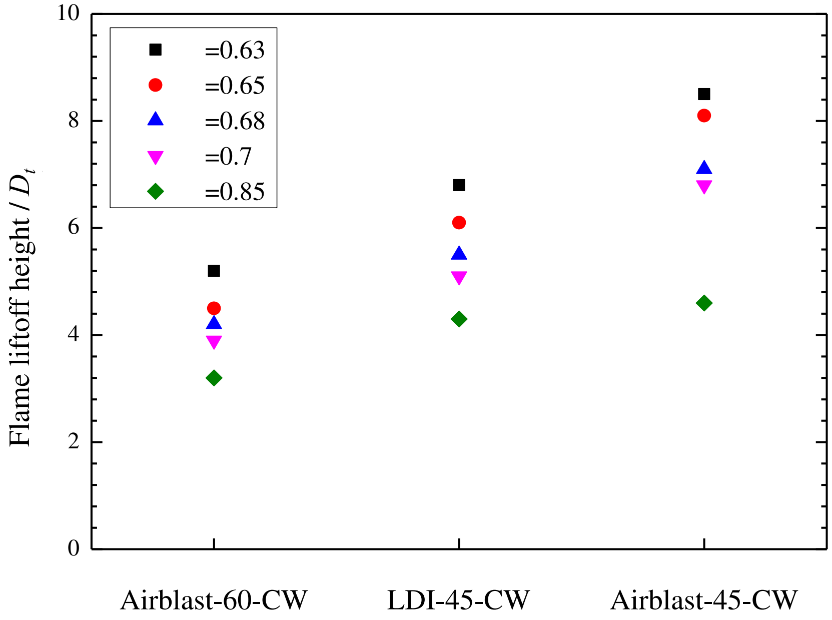

Figure 4-5. Flame liftoff height variation with overall equivalence ratio at 3% pressure drop.

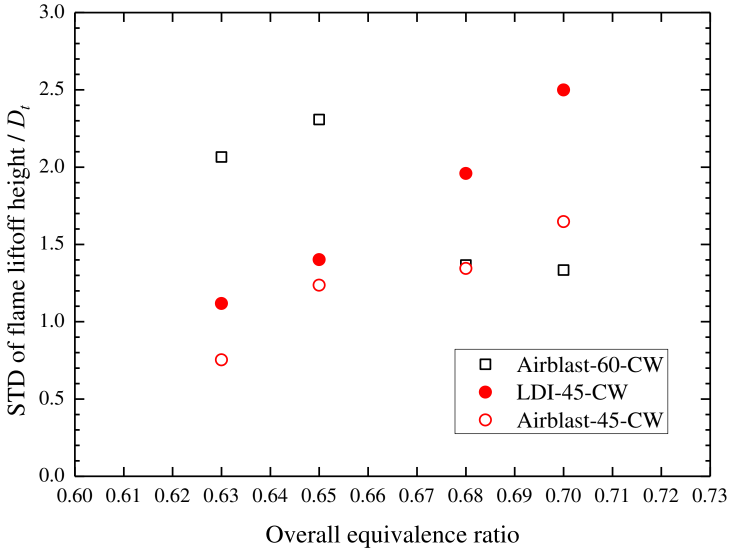

Figure 4-6. Standard deviations of flame liftoff height at 3% pressure drop and varying overall equivalence ratios.

The standard deviations (STDs) of flame liftoff height in the Airblast-60-CW, LDI-45-CW, and Airblast-45-CW configurations, under ϕ=0.63–0.7, are also obtained from CH* chemiluminescence tests, as shown in Figure 4-6. The STDs are in the range of 0.7–2.5 D_t, demonstrating the unsteadiness of flames in these three configurations. At lower equivalence ratios, i.e. ϕ=0.63 and 0.65, the Airblast-60-CW configuration exhibits the greatest flame liftoff height fluctuations amongst these three configurations. However, at higher equivalence ratios, i.e. ϕ=0.68 and 0.7, the STDs of flame liftoff height in the Airblast-60-CW configuration decrease, falling to levels similar to the Airblast-45-CW case. Comparing the two 45-CW configurations, the LDI configuration exhibits greater unsteadiness relative to its airblast counterpart, with the disparity growing as equivalence ratio increases. It is not clear from the present dataset what is driving the differences in unsteadiness between the various configurations; this subject therefore merits further investigation.

Similar to the unsteadiness observed in the flame base locations, the flare geometry also has an impact on overall flame intensity steadiness, as shown in Figure 4-7 by way of mean-normalized standard deviation of broadband imaging signals for each of the four geometries. Due to the flame anchoring on the venturi flare for the LDI-60-CW configuration, the flame in this case exhibits a normalized standard deviation of flame intensity almost half that of the other three cases. In addition, a region of very low unsteadiness exists close to the dump plate and within the interior of the V-shaped flame root evident for the LDI-60-CW configuration shown in Figure 4-2. Interestingly, the removal of the flare feature from this configuration results in the highest peak levels of unsteadiness observed for the Airblast-60-CW configuration. Finally, for both of the 45° OAS cases a relatively low unsteadiness core region exists near the dump plate and extending 4–5 D_t downstream, suggestive of a flow structure not immediately apparent in the mean flame images. The preceding discussion therefore strongly implicates the swirler geometry in impacting flame stability; this subject is explored in more detail in Section 4.3.3.

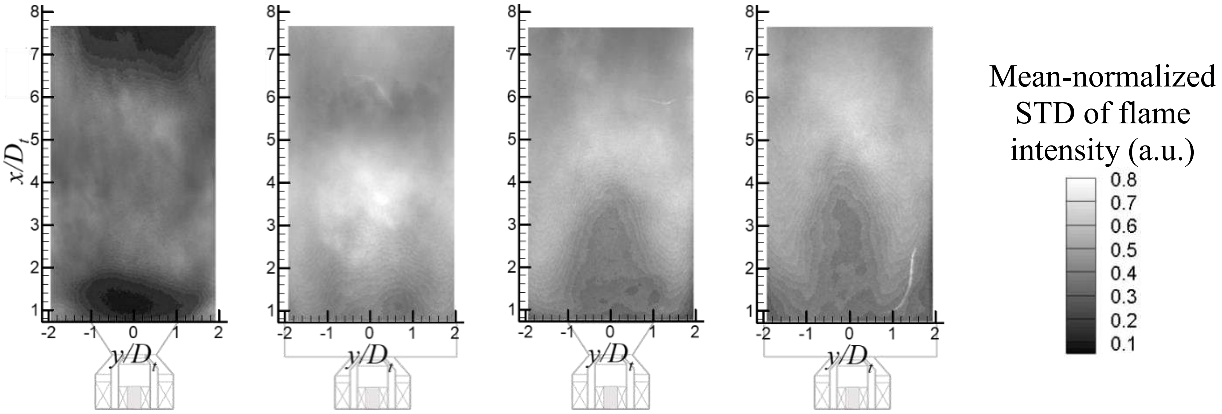

LDI-60-CW Airblast-60-CW LDI-45-CW Airblast-45-CW

Figure 4-7. Mean-normalized standard deviation of flame broadband imaging signals at 3% pressure drop and ϕ=0.70. The mean-normalized STD of flame intensity is in arbitrary units (a.u.).

In addition to the aforementioned flame liftoff height and flame unsteadiness, the venturi flare and OAS vane angle also exert noticeable effects on LBO limits, as shown in Figure 4-8, where the LBO limits of the four configurations are plotted and compared as a function of overall pressure drop across the swirl assembly. It is seen that the LDI-60-CW configuration consistently blows out at the lowest overall equivalence ratios, between ϕ=0.44 and ϕ=0.54, ~10% lower than those of the other three configurations, which as a group range in LBO from ϕ~0.53 at 0.5% pressure drop to

ϕ~0.57 at 3% pressure drop. Amongst this latter group, the Airblast-45-CW configuration exhibits the highest LBO limits across all tested pressure drop conditions, though it is only slightly higher than those for the LDI-45-CW and Airblast-60-CW cases. These latter two cases are highly similar across the pressure drop range tested. Taken together, these results suggest that removing the flare section or reducing the OAS vane angle worsens LBO limits, and that – similar to the observations of steady-state burning shown in Figures 4-2 and 3, liftoff height in Figure 4-5, and flame unsteadiness in Figure 4-7 – the LDI-60-CW configuration exhibits significantly different limit flame behavior relative to the other three configurations.

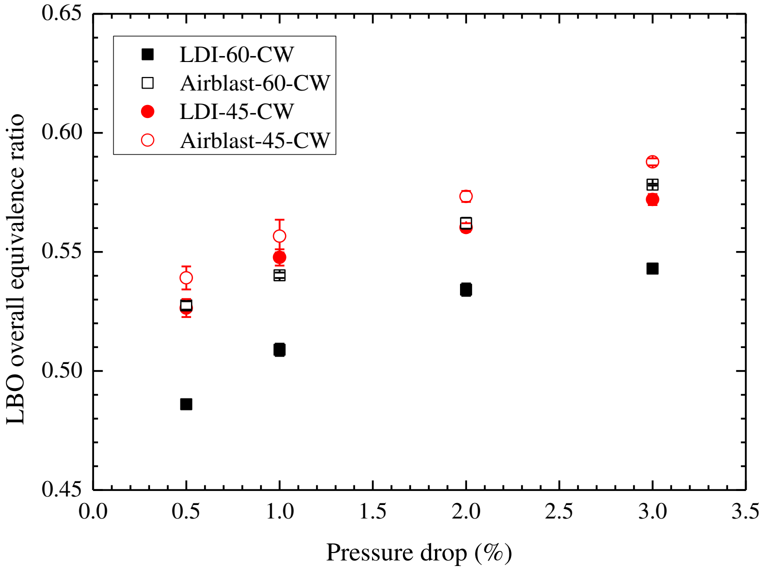

Figure 4-8. Impacts of flare and OAS vane angle on lean blowout limits.

As shown in Figure 4-9 for a pressure drop of 3% and ϕ=0.65, these differences are readily attributable to the disparate nature of the mean reacting flow field. While the LDI-60-CW case exhibits a large center recirculation zone (CRZ) with negative axial velocity along the axial centerline immediately following the venturi flare, the flow field of the Airblast-60-CW, Airblast-45-CW, and LDI-45-CW configurations are characterized by a swirling jet flow with small corner recirculation zones (CNRZs). The presence of this CRZ explains the anchoring of the flame to the dump plate – and associated reduced unsteadiness – as well as the noticeably lower LBO limits observed for the LDI-60-CW case relative to the other three configurations. The recirculation of hot product gases all the way to the interior of the venturi flare in the LDI-60-CW configuration will tend to promote both ignition and flame propagation, whereas the swirling jet flow found in the Airblast-60-CW, LDI-45-CW, and Airblast-45-CW cases have no such stabilization mechanisms. Moreover, Figure 4-9 also helps explain the more minor differences in flame structure, location, steadiness, and LBO performance between the other three designs. The dashed red lines in Figure 4-9 represent the tangent lines to the 0.1 U_t contour at an axial location of 0.8 D_t downstream of the dump plate. As is readily apparent, the LDI-45-CW and Airblast-60-CW configurations exhibit similar degrees of expansion (60˚ and 54˚, respectively) after exiting the flare, and noticeably more than is observed for the Airblast-45-CW case (31˚). The substantially greater expansion angle associated with the LDI configuration presumably results from the Coanda effect – the pressure difference between core flow and solid surface side makes jet flows deviate towards nearby solid surfaces [79,80] – due to the gentler expansion of the swirl flow through the flare feature relative to the airblast configuration. Referring back to Figure 4-8, this expansion angle correlates well with the relative ranking in terms of LBO performance. Specifically, the two configurations exhibiting similar expansion angles also exhibit similar LBO equivalence ratios, while the shallower expansion of the Airblast-45-CW case results in slightly higher LBO limits. The reason for this is relatively straightforward: faster expansion results in a shorter and weaker swirling jet flow emanating from the injector, such that the flame may stabilize closer to the swirler exit. As the axial component of the jet flow strengthens, the flame can only stabilize further downstream in lower velocity regions, thus promoting blowout.

It should be mentioned that the reacting flow and flame structures of these four configurations fueled by Jet-A were also tested, but not shown here, exhibiting the similar mean flow field structures as those fueled by methane. In addition, for liquid fuel combustion, the removal of the flare causes the disappearance of CRZ in the 60˚-OAS configuration as well.

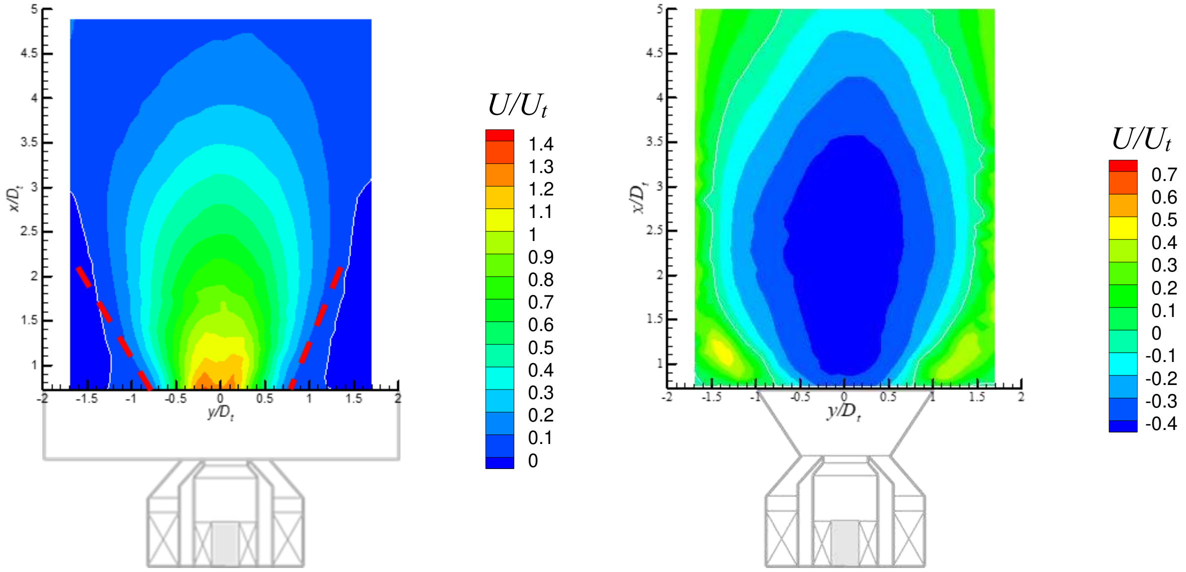

Airblast-60-CW, ϕ=0.65

LDI-60-CW, ϕ=0.65

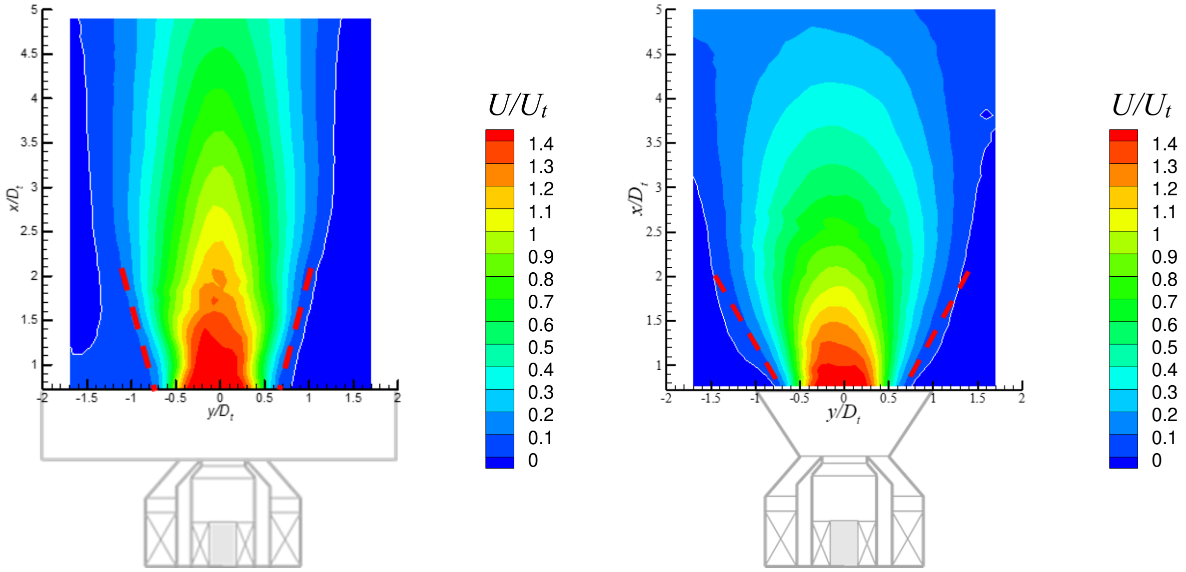

Airblast-45-CW, ϕ=0.65

LDI-45-CW, ϕ=0.65

Figure 4-9. Mean reacting flow fields of Airblast-60-CW (top left), LDI-60-CW (top right), Airblast-45-CW (bottom left), and LDI-45-CW (bottom right), at 3% pressure drop and ϕ=0.65. Red dash lines depict the tangential lines of 0.1 U_t contours at x=0.8 D_t, while white solid lines delineate the circulation zones.

In addition, the axial velocity profiles along the centerline at 3% pressure drop and ϕ=0.65, shown in Figure 4-10, demonstrate that the axial velocity rank from high to low follows the sequence of Airblast-45-CW, LDI-45-CW, Airblast-60-CW, and LDI-60-CW. As might be expected from a phenomenological point of view, this ordering correlates well with the flame liftoff height results in Figure 4-5. Perhaps more interesting, however, is the degree of similarity between the Airblast-60-CW and LDI-45-CW configurations. While the Airblast-60-CW design achieves its jet expansion purely by imparting tangential velocity to the flow, the LDI-45-CW achieves a similar effect with the addition of the flare feature, suggesting that the two configurations represent alternative paths to a similar end. From an operability perspective this observation implies that, in addition to the improved total pressure recovery that a flared exit should provide, lower swirler pressure loss may be achievable through the use of an LDI-type flare in lieu of greater OAS vane angle.

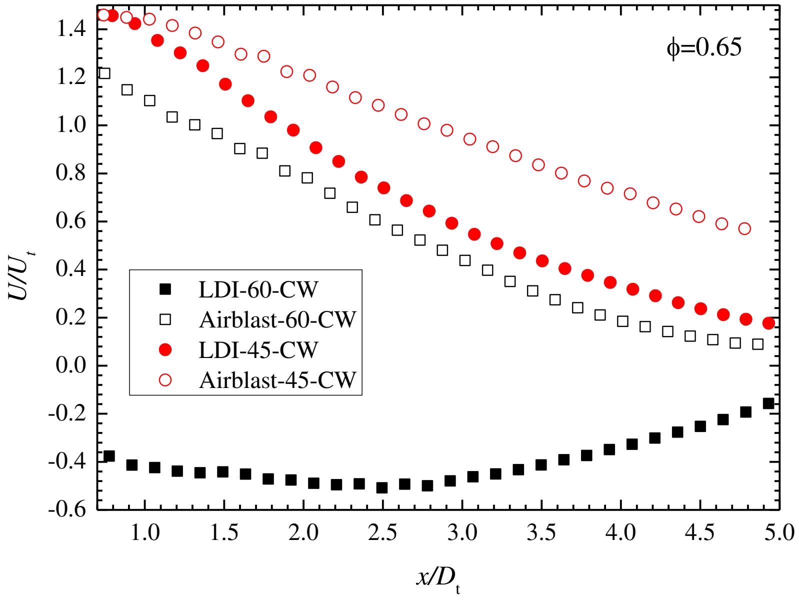

Figure 4-10. Centerline mean axial velocity profiles of four selected configurations at 3% pressure drop and ϕ=0.65.

The impact of the flare is in many ways even more apparent when comparing the Airblast-60-CW and LDI-60-CW configurations; simply by removing the flare section, the flow transitions from one dominated by a large CRZ to one characterized by a swirling jet flow, with commensurate flame structure impacts as demonstrated in Figures. 4-2 and 3. As noted by Syred and Beer [81], the formation of a CRZ is related to developing sufficient swirl strength to generate vortex breakdown. Clearly then, the removal of the flare section significantly weakens overall swirling strength to the point that vortex breakdown no longer occurs to form a CRZ. As the swirl number (defined in Eq. 3-2) relates to the impact of venturi flare, for a given vane configuration tangential velocities are essentially fixed; the addition or removal of a flare section will alter this motion very little. However, due to the Coanda effect combined with the inertial forces associated with rotation, flow passing through the venturi will tend to expand radially, reducing axial velocity. As a result, the angular momentum (numerator of Eq. 3-2) remains roughly constant, while the axial momentum (denominator of Eq. 3-2) is reduced, thereby increasing *SN* and promoting swirling jet expansion, as well as pushing the flow towards vortex breakdown and the accompanying CRZ.

4.3.2 Chemiluminescence comparison of reaction zone and NO_2^* emissions

In order to delineate high-temperature and reaction zones, OH^* and CH^* chemiluminescence, as line-of-sight (LOS) measurements, are performed in an effort to better understand the flame stabilization amongst the various test configurations. These two excited species are chosen as, in general, they are reasonable markers for high-temperature and high-heat release regions. Mean intensity contours for $\phi = 0.68$ are presented and compared in Figure 4-11, with representative OH^* regions and CH^* regions delineated by 60% and 40% maximum intensity contours, respectively. In OH^* contours, the reference maximum intensity is set by the LDI-60-CW case, to aid in representing a comparable “high temperature zone” across the four configurations. For the CH^*

results, the reference intensity is set by the maximum CH* intensity in each test case to outline the reaction zone.

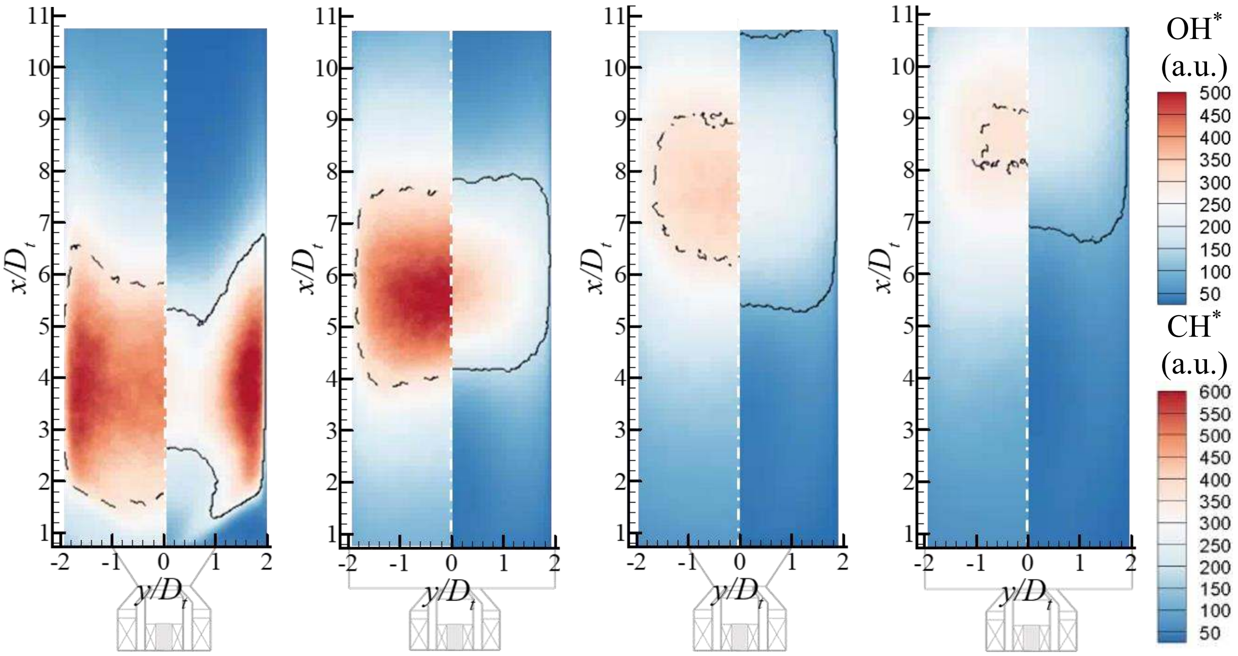

LDI-60-CW Airblast-60-CW LDI-45-CW Airblast-45-CW

Figure 4-11. Mean OH* (left halves) and CH* (right halves) at 3% pressure drop and ϕ=0.68. Dash lines are iso-contours of 60% of the maximum OH* signal intensity in the LDI-60-CW, ϕ=0.68 case; solid lines are iso-contours of 40% of the maximum CH* signal intensity in each test case. OH* and CH* signal intensities are in arbitrary units (a.u.).

As was observed from the visual flame images, in the Airblast-60-CW, Airblast-45-CW, and LDI-45-CW configurations the swirling jet flows result in a reaction zone stabilized downstream from the dump plate, where expansion of the jet and the resultant reduced velocity allow a flame to be sustained. For this type of flow, the flame location is dictated purely by a local balance between the flame propagation speed and the velocity of the turbulent, swirling jet flow. In contrast, the LDI-60-CW configuration stabilizes the flame much closer to the dump plate as a result of the presence of the CRZ. However, observing the OH* and CH* iso-contours in Figure 4-11 illustrates two important trends at play. First, for both 60° OAS cases the reaction zones defined by the CH* chemiluminescence are relatively localized when compared to the 45° OAS cases, which in addition to being of overall lower intensity are also more axially distributed. Second, observing the OH^* results in Figure 4-11 from left to right – the results being arranged in flame liftoff height order, similar to LBO rankings – it is evident that as the reaction zone extends and moves farther downstream, both the intensity and size of the high-temperature region delineated by the OH^* iso-contour decrease dramatically. Taken together these observations suggest that the more diffuse heat release regions of the lower swirl number (i.e. lifted flame) cases lead to overall lower peak temperatures and smaller peak temperature regions.

The above observation is particularly relevant in light of the focus of the LDI concept, namely reducing NO_x emissions while maintaining or enhancing the combustion efficiency and operability performance of existing fuel injection designs. In the present study an effort has been made to qualitatively identify differences in NO_x production as a function of both venturi flare geometry and OAS vane angle. To this end, NO_2^* chemiluminescence is used as a proxy for overall NO_x production, recognizing that while this method does not allow quantitative measurement of NO_x from each configuration, it does provide spatial distribution information valuable to the present analysis. Figure 4-12 compares NO_2^* distributions from all four configurations for ϕ=0.68 and 3% pressure drop. In each test case, the iso-contour of 60% of the maximum NO_2^* signal intensity is used to represent “high NO_x formation region”. It is immediately apparent that the LDI-60-CW configuration results in a much larger volume of NO_2^* emissions, beginning near the dump plate and continuing through almost the entire flametube. The other three configurations – lacking a CRZ – only begin to show NO_2^* emissions much further downstream, approximately 1–2 D_t beyond the onset of the OH^* chemiluminescence shown in Figure 4-11. As the thermal NO_x generation mechanism is a function of both the temperature and residence time within high-temperature regions, the results of Figure 4-11 become critical, in that as swirl number decreases the size and intensity of the high-temperature region decrease, with both factors inhibiting the NO_x

formation. The tests in the thesis are carried out under atmospheric conditions. As indicated by Tacina et al. [30], NO_x generally increases as inlet pressure increases.

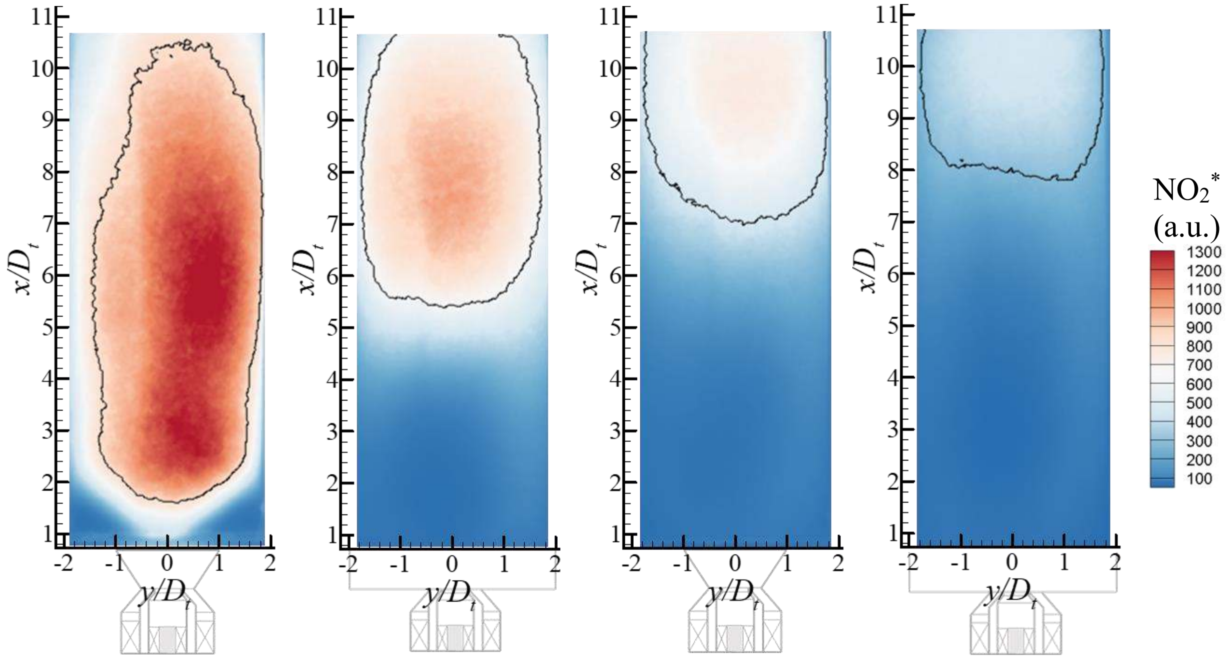

LDI-60-CW Airblast-60-CW LDI-45-CW Airblast-45-CW

Figure 4-12. NO_2^* chemiluminescence contours of four configurations at 3% pressure drop and ϕ=0.68. Solid lines are iso-contours of 60% of the maximum NO_2^* signal intensity in each test case. NO_2^* signal intensities are in arbitrary units (a.u.).

While the relative peak temperatures can to a certain extent be qualitatively compared via the proxy of OH^* chemiluminescence in Figure 4-11, a representative residence time, t_{res}, can be derived from mean axial velocity distribution along centerline, within the TR-PIV test range, 0.75–5 D_t, as

$$t_{res} = \sum \frac{\Delta x_i}{U_i} \tag{4-1}$$

where Δx_i is the axial location increment and U_i is the local mean axial velocity. Due to the complexity of the recirculating flow field for the LDI-60-CW case, only the residence times in the three configurations with swirling jet flow are formulated using Eq. 4-2, under cold and reacting conditions, as shown in Figure 4-13. The results demonstrate that the representative residence times of the various configurations rank from high to low in the sequence of Airblast-60-CW, LDI-45-CW, and Airblast-45-CW, a ranking consistent with the expected swirl strength from each case based on the flare/OAS geometry as well as the observed NO_2^* results in Figure 4-12.

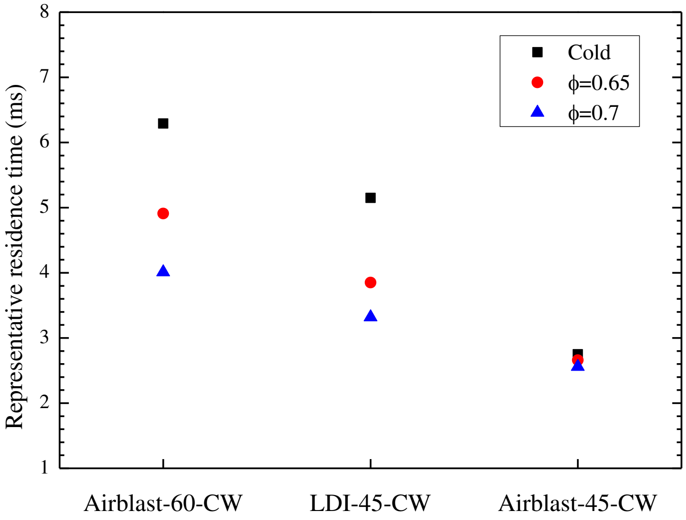

Figure 4-13. Representative residence times of three configurations with swirling jet flow.

Taken together, the results of Figures 4-11–13 suggest that the primary reaction zone effect of decreasing swirl strength – via venturi flare or OAS vane angle – is to decrease the size and intensity of the high-temperature region through a more diffuse reaction zone, which in turn implies lower NO_x generation as a result of reduced temperatures and lower residence times in high-temperature regions. Ultimately, this observation suggests that operability and NO_x emissions targets may be in direct competition, requiring conscious design tradeoffs for practical LDI applications.

4.3.3 Oscillations in flow fields

While lean-dome combustion technologies have the potential to solve challenging environmental problems, as mentioned in the introduction this lean-dome strategy is inherently susceptible to thermo-acoustic interactions, which can lead to severe structural damage or reduced system lifetime. Therefore, it is important to test and analyze the flow field oscillations for the airblast mixers of interest in this study. Since thermo-acoustic interactions inherently involve coupling between combustion heat release and coherent, periodic fluid movement, a characteristic flow boundary fluctuation derived from TR-PIV snapshots is introduced here to represent the overall flow oscillations in the swirling flows. At an axial station of x=1.5 D_t, the U=0 boundary – delineating the outer edge of the CRZ – is selected for the LDI-60-CW configuration, while for the swirling jet flow cases, a U=0.3 U_t boundary is used. Figure 4-14 demonstrates the boundary fluctuations in two flow field types – CRZ dominant flow and swirling jet flow. From the streamlines in each snapshot, the boundary location fluctuations can reflect the expanding/shrinking/swing oscillations from characteristic flow's motions.

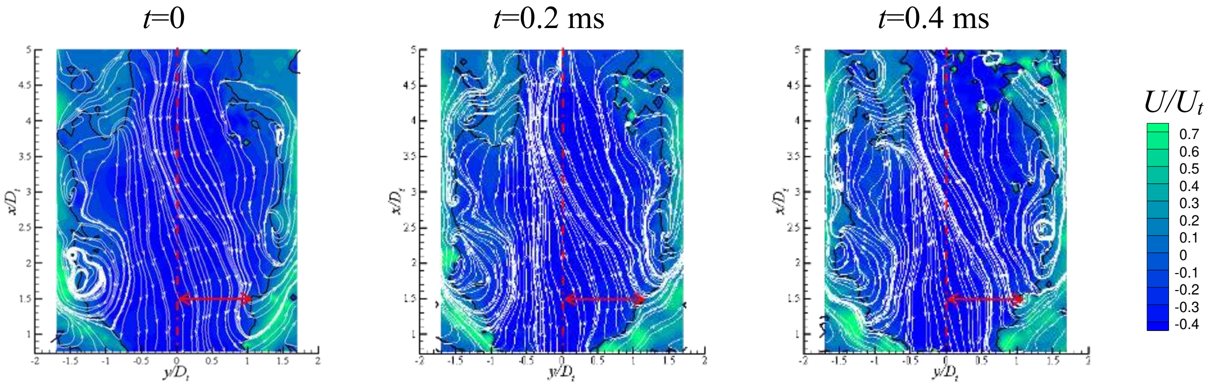

LDI-60-CW, ϕ=0.65

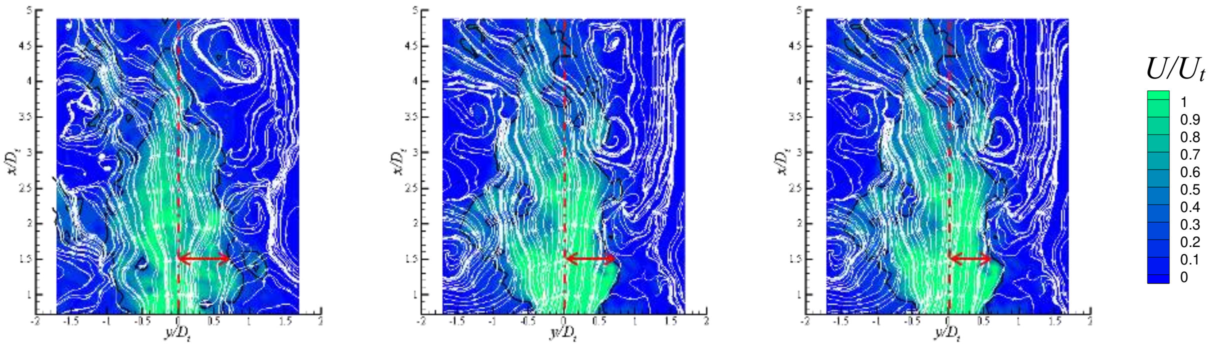

Airblast-60-CW, ϕ=0.65

Figure 4-14. Demonstration of characteristic boundary fluctuations by axial velocity contours overlapped with axial-radial velocity streamlinesfor LDI-60-CW, ϕ=0.65 (top) and Airblast-60-CW, ϕ=0.65 (bottom). Solid black lines are U=0 and 0.3 U_t contours, representing characteristic boundaries of CRZ and swirling jet, respectively. Red arrows denote boundary distances of CRZ and swirling jet at the station of x=1.5 D_t.

In order to compare the magnitudes of flow oscillations amongst the various cases, snapshot-to-snapshot location changes of the characteristic boundary are extracted from the image set. The standard deviation of the boundary location at the x=1.5 D_t station for each configuration is plotted in Figure 4-15. For the swirling jet flows, the standard deviations of boundary location would seem to largely follow the trend in swirl number; specifically, as the degree of swirl increases in the order of Airblast-45-CW → LDI-45-CW → Airblast-60-CW, the magnitude of boundary fluctuations increases. For these cases, the addition of heat release (ϕ=0.65 cases) slightly increases the degree of unsteadiness as compared to the cold conditions. In contrast to these trends, when a CRZ is present – as in the LDI-60-CW configuration – the boundary fluctuation drops, with its cold flow fluctuation becoming roughly similar to that of the LDI-45-CW case. Moreover, the addition of heat release has a larger and opposite effect for the LDI-60-CW case; when observed for reacting flows the standard deviation of boundary location drops substantially, suggesting that the heat release reinforces the stabilizing effect of the CRZ.

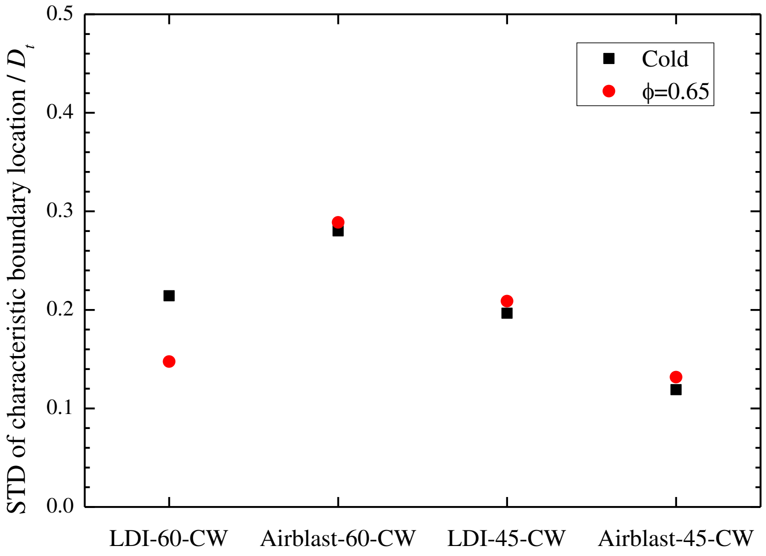

Figure 4-15. Standard deviations of characteristic boundary location at the station of x=1.5 D_t, under 3% pressure drop conditions of cold and ϕ=0.65.

Additional spectral analysis of the time-resolved boundary locations is performed using the fast Fourier transform (FFT) technique. As all interesting frequency features occur in the 0–1000 Hz range, all plots included in Figure 4-16 are restricted to this range for clarity. It is immediately apparent comparing the results from the Airblast and LDI configurations that the Airblast configurations have discernable frequency peaks, whereas – with the exception of a <10 Hz peak in the LDI-45-CW case – there is little to discern from noise in the LDI configurations.

Considering that all other geometry features and operating conditions are kept constant, this would seem to suggest that the addition of the flare section eliminates an instability mechanism present for both Airblast cases. Between the Airblast-60-CW and Airblast-45-CW cases, the former configuration results in up to double the peak magnitude of the latter in the 225–325 Hz range. It is also interesting to note that while the peak locations do not change substantially between the cold and reacting cases for the Airblast-60-CW configuration, instead becoming overall less distinct, for the Airblast-45-CW case the three apparent peaks at 110, 180, and 280 Hz in the non-reacting flow collapse to two at 40 and 190 Hz in the reacting flow. Taken together, the above results suggest that the suddenness of the expansion from the venturi throat may contribute to instabilities in the resulting flow; referring to Figure 4-9, the expansion angle of the jet is dramatically greater for the Airblast-60-CW configuration than the Airblast-45-CW configuration, which could lead to local flow separation and commensurate instability. Additional detailed study of the nature of the shear layer immediately following the venturi exit will be required to corroborate this hypothesis, as the present spectral analysis is qualitative in nature.

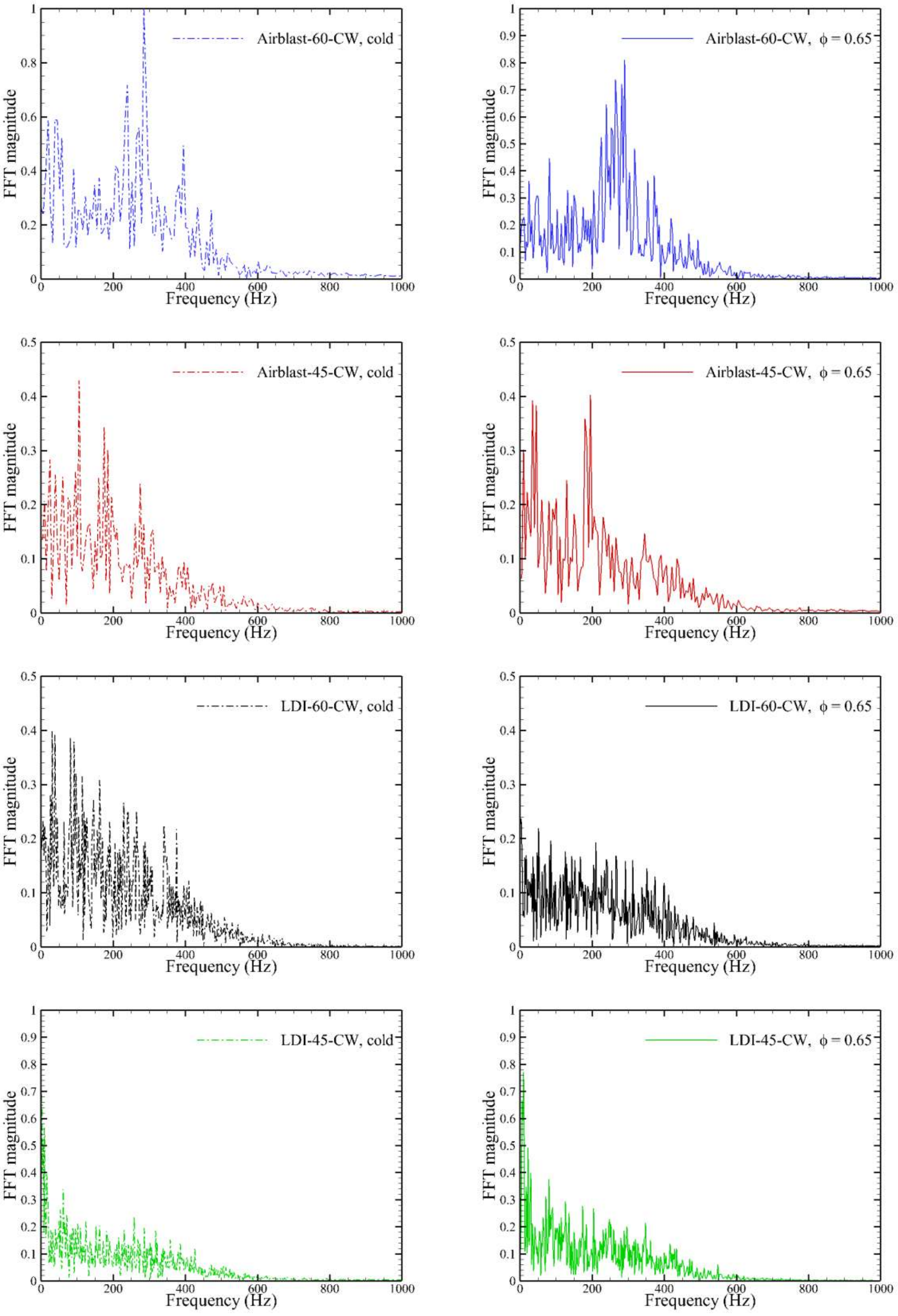

Figure 4-16. FFT analysis on characteristic boundary location fluctuations of Airblast and LDI configurations.

4.4 Concluding Remarks

In this study, velocity and radical fields have been investigated using a variety of diagnostic techniques to provide insights into the impact of a flare feature on the flame responses, LBO limits, flow oscillations, and NO_x emission levels for four LDI-based configurations. The results clearly demonstrate that removing the flare reduces swirl strength which in turn leads to the loss of a CRZ between the LDI-60-CW and Airblast-60-CW configurations, and increases the length of the swirling jet flow from the LDI-45-CW configuration to the Airblast-45-CW configuration. Furthermore, reducing the swirl strength via either flare removal or OAS vane angle reduction for lifted cases tends to increase flame liftoff height, diffuse the reaction zone, and decrease the size and intensity of high temperature regions within the flametube. As a direct result, LBO limits are higher in the Airblast configurations than in the corresponding LDI counterparts, particularly for the 60° OAS cases where the configuration differences result in a transition from an anchored to lifted flame. Conversely, while reducing swirl strength has an adverse effect on LBO performance, flame liftoff height, and flame length, the more diffuse reaction zones and commensurately smaller high-temperature regions reduce the generation of NO_x, as reflected here by an NO_2^* proxy. Taken as a whole, the results presented herein suggest that while the inclusion of a venturi flare serves as a method for increasing swirl strength which tends to improve operability, for a single swirler operability and NO_x emissions targets appear to be in inherent tension; reducing NO_x can be achieved by lowering swirl strength, but at the cost of LBO, flame liftoff height, and other operability metrics.

CHAPTER 5 AN EXPERIMENTAL AND CFD STUDY ON NON-REACTING FLOWS AND THE IMPACT OF OAS/IAS ROTATING DIRECTION IN LDI

5.1 Introduction

Recent LDI research has largely entailed replacing relatively large swirl assemblies with a series of much smaller, independently-fueled swirl injectors in a patterned array. This difference, while adding significant complexity to the fuel control systems, facilitates tailoring the specific design for good emissions performance throughout the flight profile, from low-power ground idle to full-power take-off conditions. Such multi-point designs have been explored by a number of studies [27,30,31,33,83,84].

While significant efforts have gone into the investigation of injector-to-injector interactions for multiplex fuel injectors, it remains unclear about the understanding of the fundamental behavior of the individual swirl injectors by experiments and CFD simulations, which is critical to predict the performance of the system as a whole. Although there are few studies regarding the CFD research on single-element LDI, numerical simulations of LDI validated by high-fidelity data are quite limited. Li et al. [41] used a RKE RANS model to simulate a hydrogen-fueled LDI injector with a 23-step finite rate chemical mechanism, in which the pressure drops, total temperatures, and NO emissions indices for a variety of operating conditions were discussed. Patel et al. [42,43] examined an LDI-type fuel injector with LES, finding that the inclusion of a droplet breakup model primarily impacted the fuel evaporation near the injector exit, while time-averaged results with and without a breakup model were similar further downstream. Furthermore, Patel et al. [42] were able to capture unsteady features such as the precessing vortex core.

This chapter represents a continuing effort to explore these individual impacts, using both experimental and computational tools to develop a robust understanding of geometric design effects on LDI swirl injector performance. Here, we investigate the axial-axial LDI swirler concept with 60° OAS and IAS vanes, forming counter- or co-swirling configurations. The objectives of this study are four-fold. First, these serve as baseline geometries for future studies which will investigate the impact of various LDI-relevant swirler geometry features. To this end, key non-reacting flow field features measured by using time-resolved PIV are identified and characterized. Second, a self-consistent and robust CFD mesh generation strategy is developed to create notionally grid-independent CFD meshes for iso-thermal flow simulations, using the present geometries as validation cases. Third, the effects of turbulence modeling, including RANS and LES, and the sub-grid scale (SGS) models in LES predictions on flow field are explored. Finally, the impact of relative OAS/IAS rotating directions on the flow characteristics and practical LDI applications is investigated and discussed.

5.2 Experimental and Numerical Description

5.2.1 Experimental setup

Figure 5-1 shows the geometric structure of the single-element SV-LDI configurations studied in present work. Helical 60° OAS vanes are installed with clockwise (CW) or counter-clockwise (CCW) rotation direction (looking from the upstream side), while the IAS vanes are fixed at a 60° counter-clockwise (CCW) rotation, forming a counter- or co-swirling flow between the IAS and OAS. The counter-swirling configuration is referred to hereafter as the LDI-60-CW configuration, and the co-swirling configuration is referred to hereafter as LDI-60-CCW configuration. Details about the swirlers in each configuration are included in Figure 5-2.

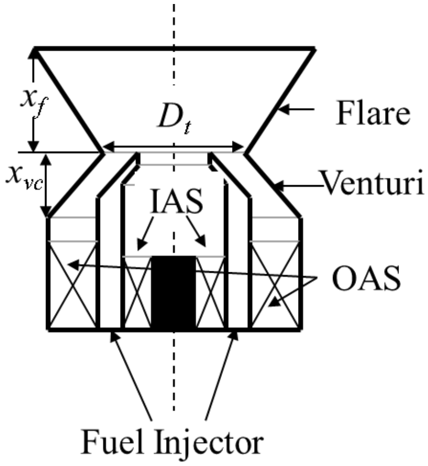

Figure 5-1. Detailed schematic of the LDI mixer.

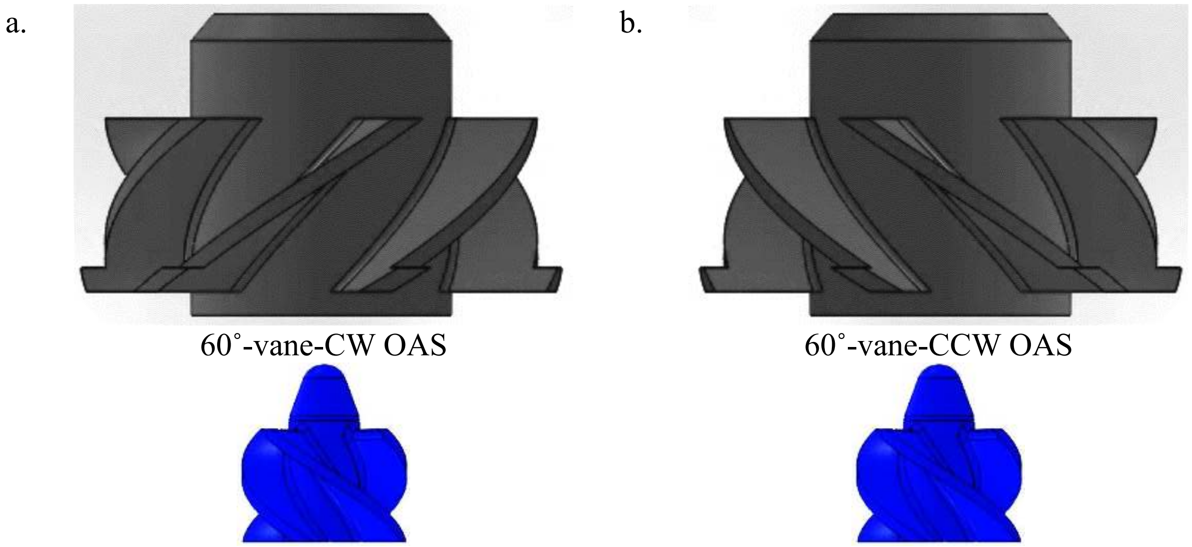

a. 60˚-vane-CW OAS, 60˚-vane-CCW IAS, LDI-60-CW

b. 60˚-vane-CCW OAS, 60˚-vane-CCW IAS, LDI-60-CCW

Figure 5-2. Swirlers used for configurations: a. LDI-60-CW (counter-swirling) and b. LDI-60-CCW (co-swirling).

The non-reacting flow field measurements are performed using TR-PIV at a 3% pressure drop (ΔP) across the LDI injector and combustor chamber. The Reynolds number (Re) based on the mass flux and the venturi throat diameter is ~ 35,000. The capture area for the mean velocity map is 50 mm × 60 mm, focused at the area from the injector dump plane to 60 mm downstream. Mean axial-radial (U-V) velocity maps are processed from the full 1-second collection period, at repetition rate of 5 kHz.

5.2.2 Computational approach and modeling

5.2.2.1 Turbulence modeling and boundary conditions

RANS and LES are used to investigate the impact of turbulence model on the non-reacting LDI flow simulations. In the case of RANS, SKE turbulence closure model is utilized since it exhibits the best data match amongst RANS models in predicting recirculation bubble of the swirl cup modeling [54]. The effect of SGS models in LES on predicting LDI turbulent flows is explored by comparing between the simulation results of Dynamic Smagorinsky [55–57] and Dynamic Structure [58] SGS models. It is noteworthy to mention that the Dynamic Smagorinsky SGS is only used to study the SGS effect in Section 5.3.4; all the other LES simulations utilize the Dynamic Structure SGS model. In RANS, standard wall function [59] predicts the near-wall turbulence, while in LES the near-wall turbulence is simulated by the Werner and Wengle wall model [60], which is less expensive in computational cost.

The inlet boundary conditions for the LDI combustor calculations are chosen to be placed at the inlet of the air manifold. The mass flow velocity boundary condition is used as the inlet boundary condition, which is a special case of the Dirichlet velocity boundary condition. The mass flow rate used in simulations is the same as that used in the experiments, which is measured by calibrated choked nozzles. For LES, the fluctuating inflow boundary are imposed at the inlet. It uses the concept of digital filtering to generate turbulent fluctuations, which are then superimposed on the inflow velocity profile. The fluctuation intensity, 13%, is determined from TR-PIV measurement on the manifold inlet under typical mass flow rates. Input of fluctuation length scale is determined by the dimensions of fine-mesh inserts, which are used to uniformize air flow in the air manifold. The outlet is placed at the physical exit of combustor. At the outlet boundary, zero-gradient boundary condition is applied for the velocity components, along with a prescribed constant atmospheric pressure condition.

5.2.2.2 Computational domain and mesh generation

The three-dimensional computational domain for LDI configurations consists of air inlet manifold, swirler-venturi assembly, and combustion chamber, as shown in Figure 5-3. The grids are generated by cut-cell Cartesian grid method [51]. Two sets of meshes, Mesh-1 and Mesh-2, are generated to perform grid independence study. The base grid size of Δ_0 = 1 mm for Mesh-1, and Δ_0 = 0.8 mm for Mesh-2 is applied to regions of air manifold or downstream of combustor, as outlined in Figure 5-3. To balance the computational cost and the need to resolve sufficient scales of turbulence, the fixed embedding is applied to better resolve the flows within swirlers and venturi (Δ_2 = 0.25 mm for Mesh-1 and Δ_2 = 0.2 mm for Mesh-2) and near-dome region (Δ_1 = 0.5 mm for Mesh-1 and Δ_1 = 0.4 mm for Mesh-2), as also shown by the close-up look in Figure 5-3. Note that in Δ_n, n represents the level of mesh refinement with respect to the base grid size Δ_0. The total cell counts are 5.2 million for Mesh-1 and 10.2 million for Mesh-2.

5.2.2.3 Numerical Setup

The governing conservation equations are discretized by a second-order-accurate spatial discretization scheme. PISO method are used to solve the transport equations [63]. A fully-implicit first-order-accurate time integration scheme is employed to maintain numerical stability in the cases of LES. The time-step is not fixed but automatically calculated in the range of 10^{-8} s to 10^{-5} s, which is guided by the maximum convection CFL number, the speed of sound CFL number and the diffusive CFL number. Turbulence statistics collected over more than three flow-through time in LES cases.

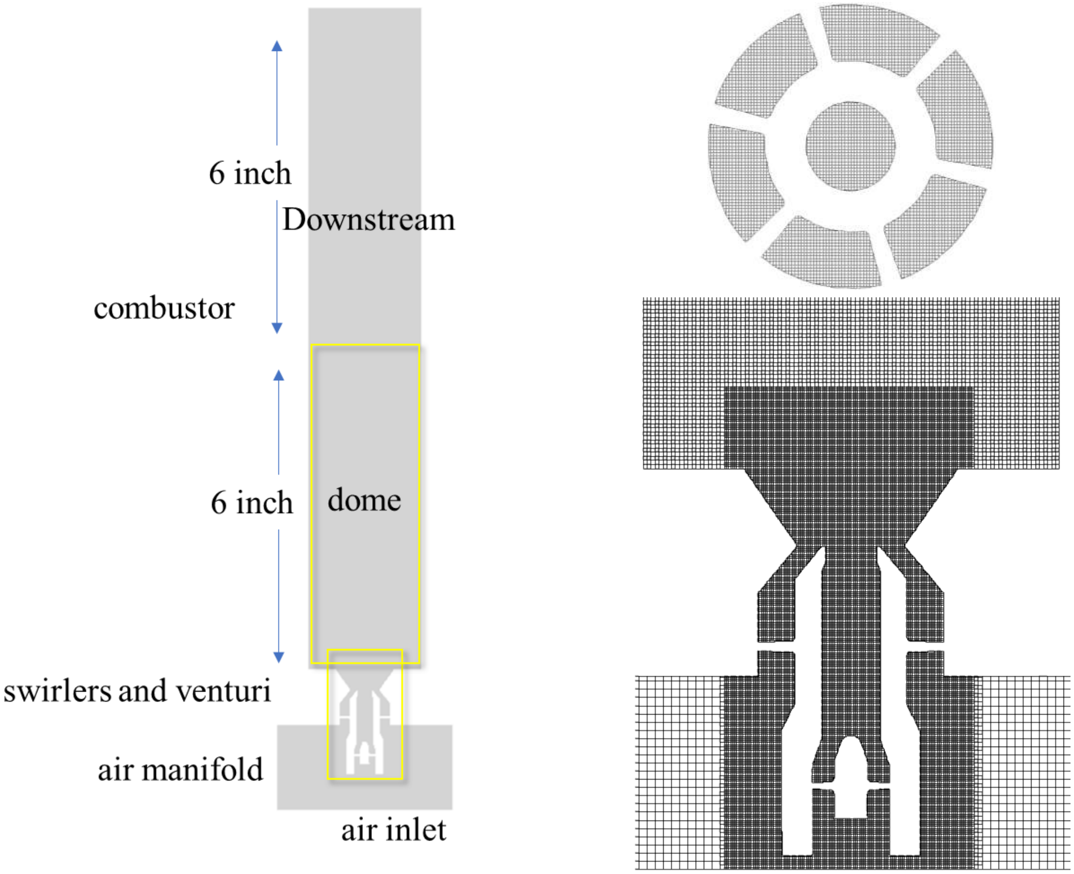

Figure 5-3. Computational domain (left) and grid distribution in horizontal cut of swirler (right top) and close-up look of swirler-venturi assemble (right bottom).

5.3 Results and Discussion

5.3.1 Main flow field characteristics

As mentioned previously in the introduction, the CFD simulation can provide insights into understanding the LDI flow. The main flow features of LDI-60-CW, obtained by LES based on Mesh-2, are displayed in Figure 5-4, where the contours of time-averaged axial (U), radial (V), and tangential (W) velocity components are presented in the x-y (axial-radial) plane (z=0) through the combustor. From the distributions of time-averaged axial velocities, it can be recognized that a vortex breakdown occurs near the exit of venturi, which forms a center recirculation zone (CRZ). Figure 5-5 shows the three-dimensional streamlines in the time-averaged flow field of LDI-60-CW configuration. The iso-surfaces of zero axial velocity clearly indicate the existence of the center and corner recirculation zones. As presented in Figure 5-5, a representative streamline exhibits that the flow injected near the center of throat rotates along axial axis, and reverses back into CRZ several times before exiting downstream. Since the entire flow field exhibits a complex structure, further investigations on the flow details are necessary.

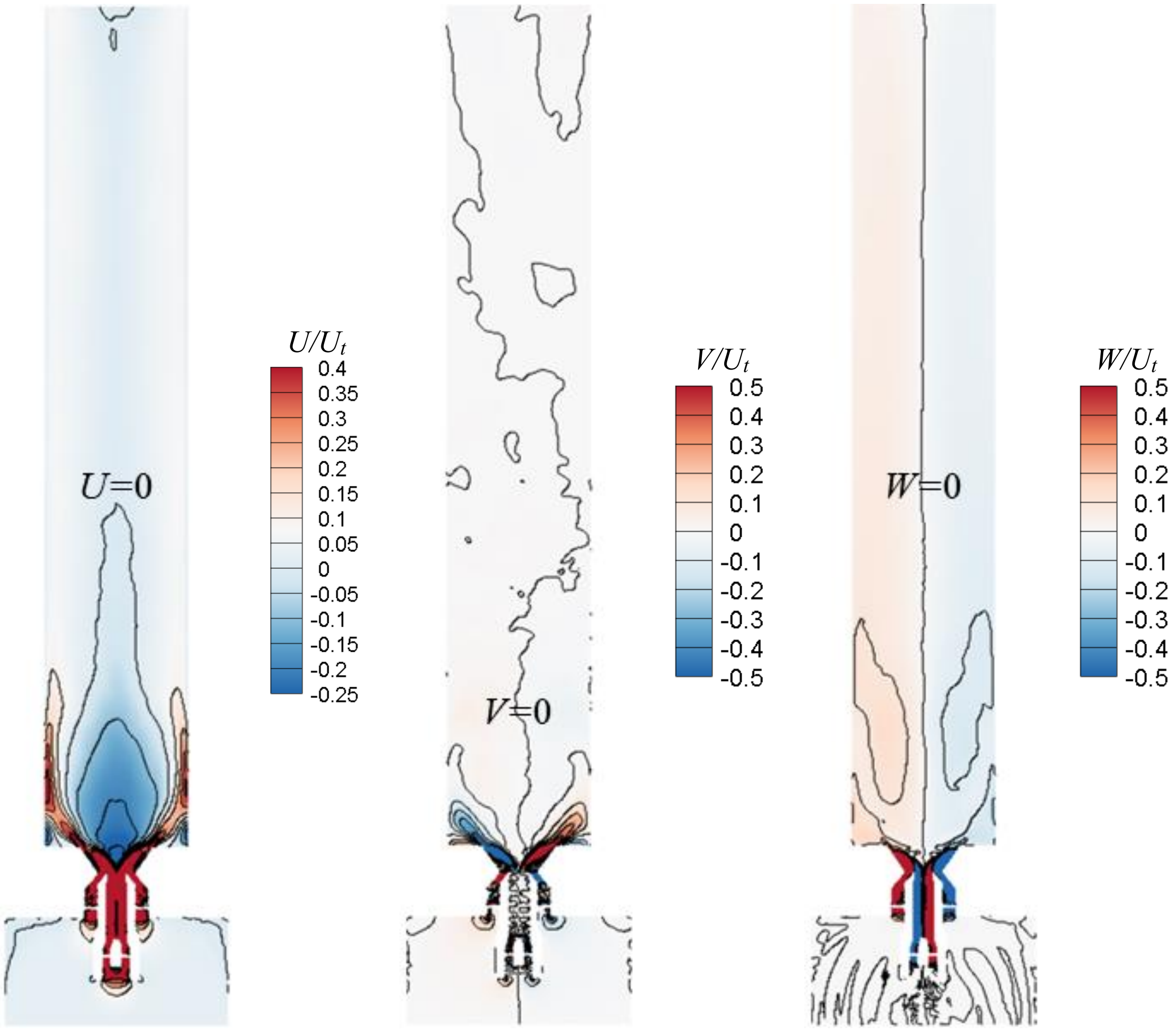

(a) (b) (c)

Figure 5-4. Time-averaged velocity components of LDI-60-CW (counter-swirling) configuration on *x*-*y* plane through the combustor, (a) axial velocity, *U*, (b) radial velocity, *V*, and (c) tangential velocity, *W*, for LES using Mesh-2. The increment between velocity contour-lines is 0.1 U_t.

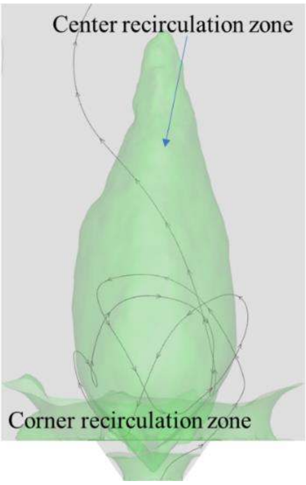

Figure 5-5. Streamline in time-averaged flow field of LDI-60-CW (counter-swirling) configuration. The iso-surface denotes zero time-averaged axial velocity, i.e. $U = 0$.

Figure 5-6 shows snapshots of the vorticity magnitude fields on a single longitudinal (x-y)- and three latitudinal (x-z)-planes for LDI-60-CW configuration. Because of the strong shear between the incoming flow from venturi and the reverse flow from CRZ, a strong vorticity layer is produced along the boundary of the CRZ, which subsequently rolls, stretches and breaks up into small vorticity cores. Just after the venturi throat at the *A-A* cross-section, a strong shear layer develops between the IAS and OAS, observable by the circular region of high vorticity. Also, the flow pattern on the *A-A* plane clearly illustrates the structures associated with the six passages and the four passages from OAS and IAS, respectively. Such flow patterns diminish as the flow moves downstream, as shown at the *B-B* cross-section. As one moves downstream to *C-C* plane, the entire flow path experiences high and variable-direction vorticity, suggestive of significant velocity gradients and therefore significant shear. As a result, one could expect that these conditions would be highly conducive to primary droplet breakup, vaporization, and mixing for practical spray combustion application, which are arguably the most critical features of a successful LDI concept.

The simulated time-averaged axial velocity comparisons with the corresponding PIV experimental results are provided in Figure 5-7 for the LDI-60-CW and LDI-60-CCW configurations, respectively. The measured and predicted distributions of the time-averaged axial velocity in *x-y* plane through the combustor are displayed in detailed view for the near-dome field. As indicated by the iso-contours of U/U_t = -0.1, the locations of center recirculation zones are predicted precisely for both configurations. It should be mentioned that due to the tiny sizes and being close to the chamber corners, the corner recirculation zones (CNRZs) exist but are not clearly captured in the current PIV results.

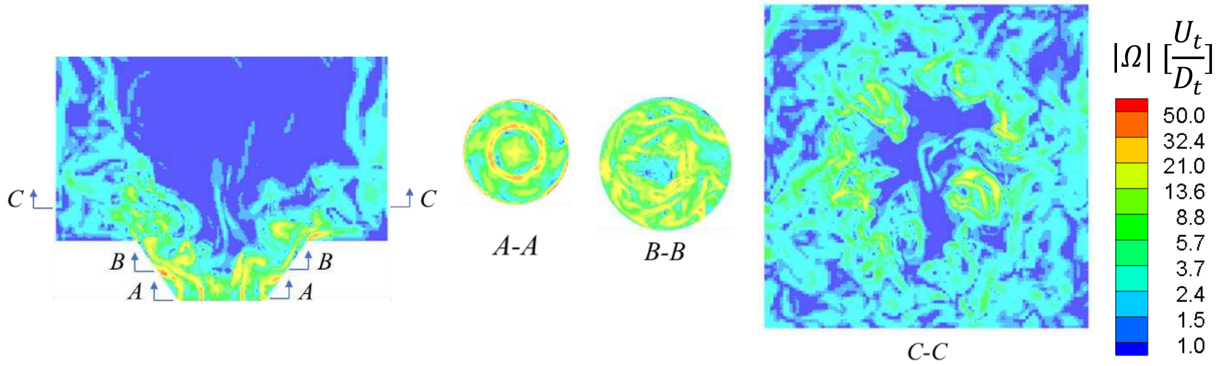

Figure 5-6. Snapshots of normalized vorticity-magnitude ($|\Omega|$) fields on *x-y* (first one from left) and *x-z* (rightmost) cross-sections of LDI-60-CW (counter-swirling) configuration.

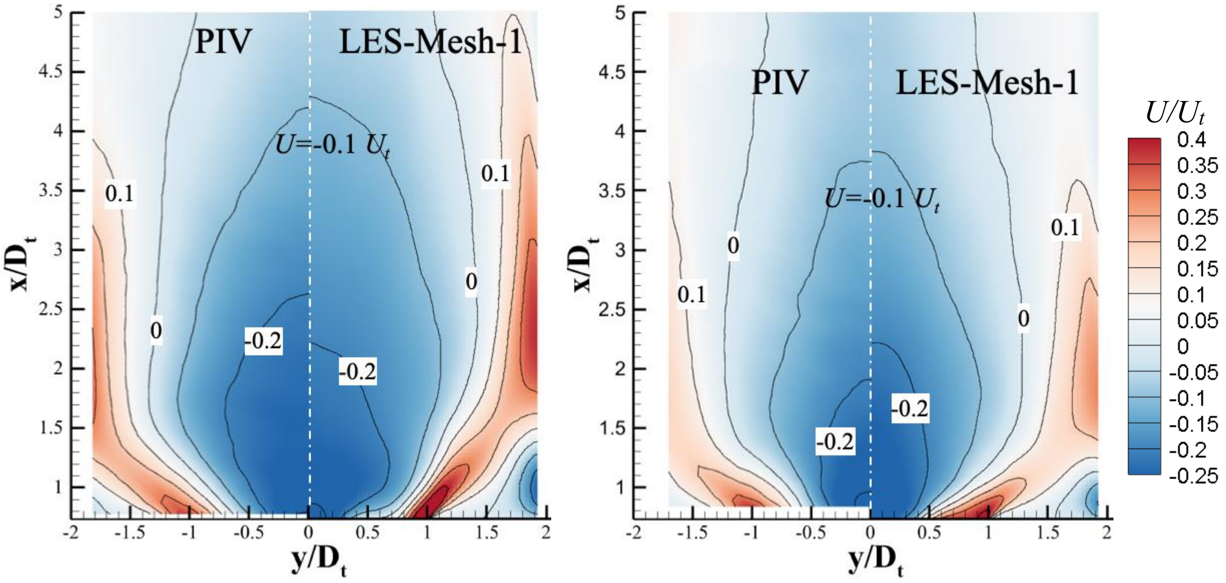

LDI-60-CW LDI-60-CCW

Figure 5-7. Detailed views of time-averaged axial velocity distributions on *x-y* plane (*z*=0) in the near-dome region of LDI-60-CW (counter-swirling) and LDI-60-CCW (co-swirling) configurations. The increment between velocity contour-lines is 0.1 U_t.

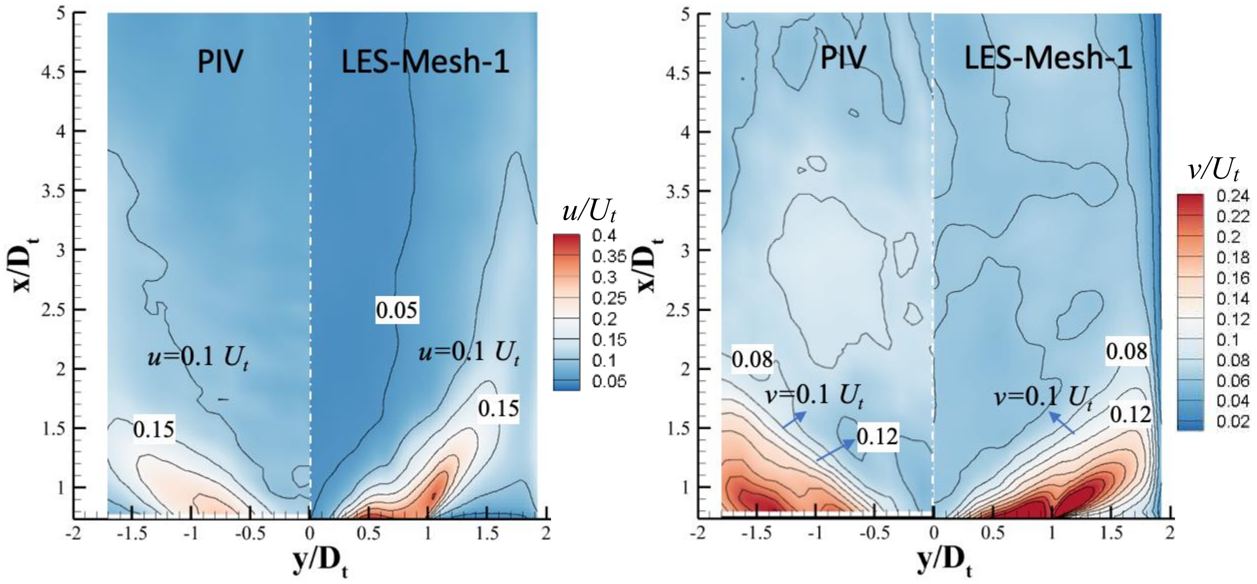

RMS axial velocity

RMS radial velocity

Figure 5-8. Detailed views of RMS axial (left) and radial (right) velocity distributions on *x*-*y* plane (*z*=0) in the near-dome region of LDI-60-CW (counter-swirling) configuration. The increment between RMS axial velocity contour-lines is 0.05 U_t; the increment between RMS radial velocity contour-lines is 0.02 U_t.

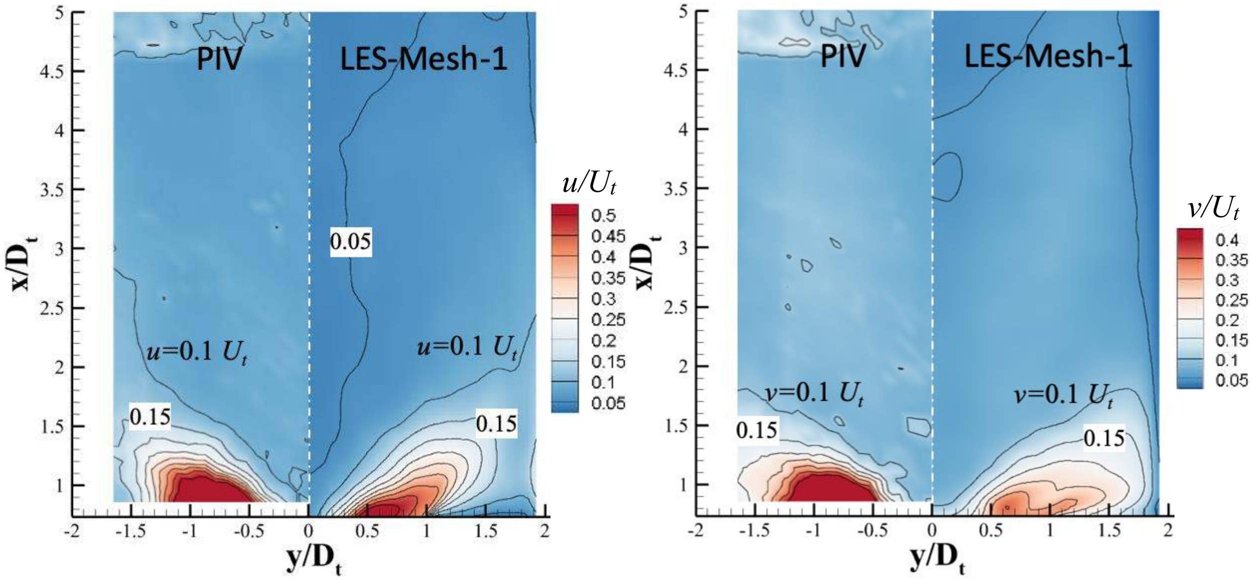

RMS axial velocity

RMS radial velocity

Figure 5-9. Detailed views of RMS axial (left) and radial (right) velocity distributions on *x*-*y* plane (*z*=0) in the near-dome region of LDI-60-CCW (co-swirling) configuration. The increment between RMS velocity contour-lines is 0.05 U_t.

In addition to the time-averaged flow validations, the fluctuations of axial and radial velocities are compared against experimental data for the LDI-60-CW and LDI-60-CCW configurations in Figures 5-8 and 9, respectively. In the regions with highly fluctuating velocity, root-mean-square (RMS) results from LES are greater than those from PIV in LDI-60-CW, but smaller in LDI-60-CCW. The simulations of both configurations predict the locations of strongly fluctuating velocity accurately, showing that LDI flow is highly fluctuating in the shear layer region near the dump plate. To summarize, a fair qualitative overall agreement is observed for the time-averaged and RMS velocity fields between the simulated results and experimental data.

5.3.2 Grid convergence check

Performing grid independence studies is difficult but necessary in three-dimensional unsteady turbulence simulations, whereas it becomes even more complex for LES. Two meshes, Mesh-1 and Mesh-2, with different gird sizes as described in the numerical setup, are simulated using identical LES (Dynamic-Structure SGS) model and boundary conditions for the counter-swirling configuration, LDI-60-CW. The results from two different meshes of LDI-60-CW are compared in terms of detailed profiles of time-averaged and RMS axial/radial velocities at various stations, as well as global parameters, like the effective area and the CRZ bubble size.

The overall effect of grid size on axial velocity distribution is illustrated via the time-averaged axial velocity distributions along the centerline (y=0), as exhibited in Figure 5-10. With either Mesh-1 or Mesh-2, the LES-predicted axial velocity distribution along the axis centerline is similar. The largest difference is about 0.3 U_t near the flare exit. Both LES cases predict the time-averaged axial velocity becomes less negative downstream of the venturi exit.

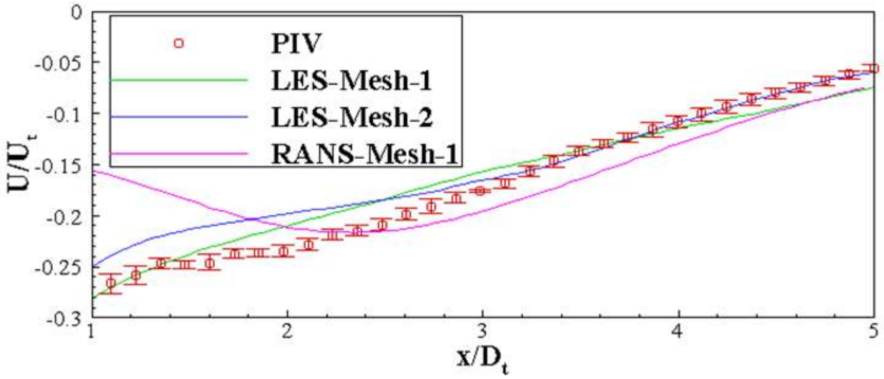

Figure 5-10. Comparisons of time-averaged axial velocity profiles along the centerline (*y*=0) for LDI-60-CW (counter-swirling) configuration.

In addition to axial velocity distributions along the centerline, profiles of time-averaged axial and radial velocities along the radial directions are compared between two meshes at six axial stations, i.e., x = 0.5, 1, 2, 3, 4, and 5 D_t, as shown in Figure 5-11 for LDI-60-CW. The predictions of both U and V profiles at x = 1, 2, 3, 4, and 5 D_t are close between LES-Mesh-1 and LES-Mesh-1 cases. As presented by the profiles at x = 0.5 D_t, some discrepancy between the results from these two cases exists within the left side of the flare. The profiles of RMS axial and radial velocities at the same axial location are displayed in Figure 5-12 for LDI-60-CW. The predictions of LDI-60-CW show a satisfactory overall agreement with the experimental values, though at x = 1 and 2 D_t, large deviations are observed for the peak value of the axial RMS velocity. Both Mesh-1 and Mesh-2 predict quite similar RMS axial and radial velocity results except for the flare region, as illustrated by axial station at x = 0.5 D_t. When considering the impact of meshes on time-mean and RMS axial/radial velocity profiles, although there are some differences between LES-Mesh-1 and LES-Mesh-2 cases within the flare (x = 0.5 D_t), the two mesh cases give very close predictions at all the dome stations for the LDI-60-CW configuration.

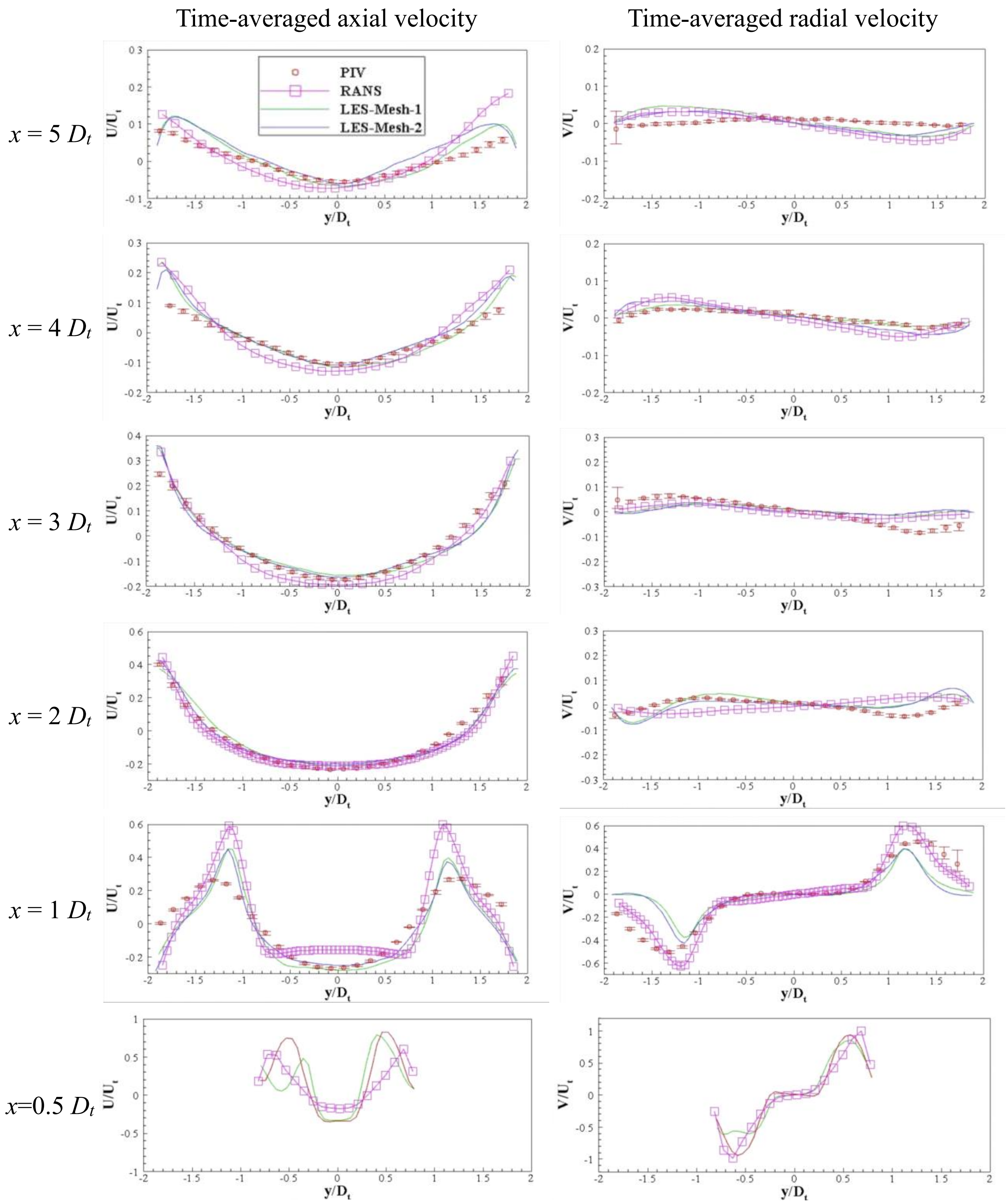

Figure 5-11. Comparison of measured (PIV), RANS using Mesh-1, LES-Mesh-1 and LES-Mesh-2 results of$U$ (left) and V (right) profiles along the radial direction at x = 0.5, 1, 2, 3, 4, and 5 D_t in LDI-60-CW (counter-swirling). Error bars of PIV results are from min/max variations of different tests.

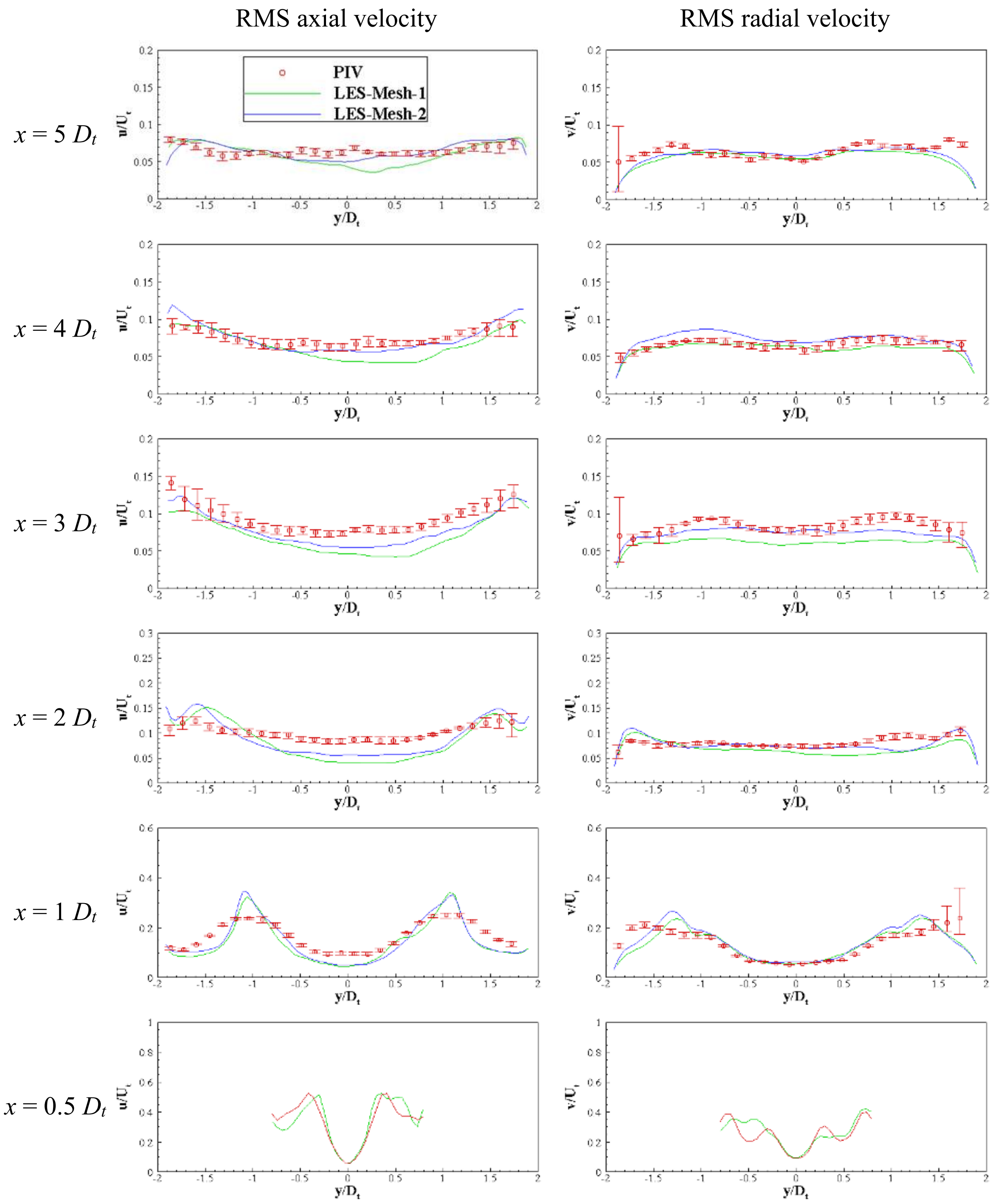

Figure 5-12. Comparison of measured (PIV) and LES predicted fluctuating axial and radial velocity profiles, *u* (left) and *v* (right), on two different grids (Mesh-1 and Mesh-2) along the radial direction at $x = 0.5$, 1, 2, 3, 4, and 5 D_t for LDI-60-CW (counter-swirling). Error bars of PIV results are from min/max variations of different tests.

As a validation to simulate the experimental hardware, a computational estimation of the effective area (A_e) is computed based on Eqns. 5-7 and 8 for each of the simulation cases and compared to the measured value.

$$A_e = \frac{\dot{m}}{\rho_{air} U_P} \tag{5-7}$$

$$U_P = \sqrt{\frac{2\Delta P}{\rho_{air}}} \tag{5-8}$$

For LDI-60-CW, the measured A_e is 76.69 ± 0.15 mm^2. The LES-Mesh-1 case predicts 74.96 mm^2, and the LES-Mesh-2 case predicts 74.48 mm^2. The computed effective areas by LES using the Mesh-1 and Mesh-2 are both under-predicted, but within 3% differences to the measured A_e. In addition, the relative difference of LES predicted effective areas from Mesh-1 and Mesh-2 is just 0.6%.

Table 5-1. Effective area comparison between measurements and predictions.

Configuration	Measurements (mm^2)	RANS-Mesh-1 (mm^2)	LES-Mesh-1 (mm^2)	LES-Mesh-2 (mm^2)
LDI-60-CW	76.69 ± 0.15	79.57	74.96	74.48
LDI-60-CCW	77.10 ± 0.20		76.22	

Since CRZ has great influence on LDI performance, the differences in terms of the CRZ bubble dimensions are checked for grid independence, as depicted in Figure 5-13. To ease the comparison between simulations and PIV in the following discussion, the CRZ dimensions are represented by the -0.1 U_t contours. The LES-Mesh-1 of LDI-60-CW sees this contour closing at 4.28 D_t, a feature which is captured reasonable in LES-Mesh-2 (closing at 4.17 D_t). Besides the CRZ closure location, the spatial distributions of -0.1 U_t contours are almost indistinguishable. Thus, the LES cases of two meshes not only qualitatively predict the CRZ bubbles, but also quantitatively simulate the bubble dimensions.

For an optimal grid resolution in LES, Pope [85] suggested that at least 80% of the turbulent kinetic energy should be resolved rather than modelled by the grid. Meanwhile the portions of resolved TKE over total TKE from LES-Mesh-1 and LES-Mesh-2 of the counter-swirling configuration are 96.6% and 97.3%, respectively. Thus, the well-matched predictions of the dome-region mean and RMS velocity profiles, effective area, CRZ bubble dimensions, and resolved turbulent TKE portion from the two mesh sets indicate that Mesh-1 (5.2 million cell counts) provides an adequate gird resolution for the simulations.

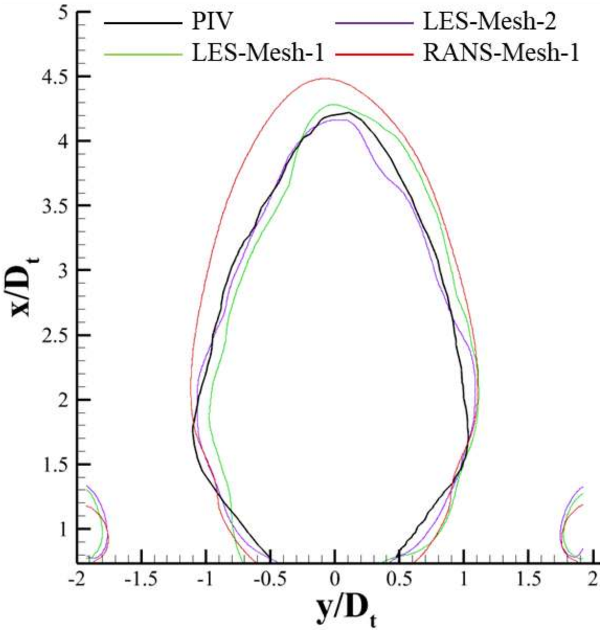

Figure 5-13. Comparison of -0.1 U_t contours on x-y plane between experimental data and simulation results for LDI-60-CW (counter-swirling) configuration.

5.3.3 Comparison between RANS and LES on non-reacting flow predictions

In this section, the effect of turbulence modeling (RANS and LES) is explored for the LDI-60-CW (counter-swirling) configuration, using Mesh-1. Overall time-averaged axial velocity comparisons between RANS and PIV results are provided in Figure 5-14. With the existence of CRZ and CNRZs, RANS is able to predict the main flow pattern in LDI-60-CW. To elucidate the difference of RANS and LES in LDI simulations, the predictions are further validated against experimental data via foregoing comparison criteria for grid convergence, i.e. detailed profiles of time-averaged axial and radial velocities at various stations, as well as global parameters, like the effective area and CRZ bubble dimensions.

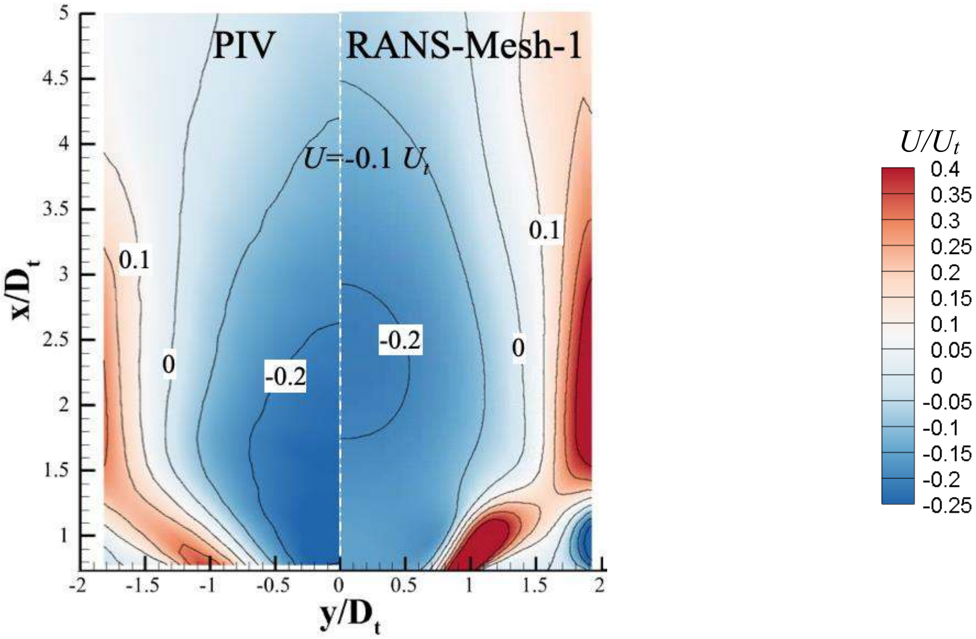

Figure 5-14. Detailed views of time-averaged axial velocity distributions on *x-y* plane from PIV and RANS in the near-dome region of LDI-60-CW (counter-swirling). The increment between velocity contour-lines is 0.1 U_t.

For a comparison over the overall impact of turbulence model on axial velocity through the dome region, the time-averaged axial velocity distributions along the centerline (y=0) from the results of PIV, RANS, and LES are collated in Figure 5-10. With Mesh-1, the prediction of the axial velocity distribution along the axis centerline using LES is more accurate than RANS. Also, the trend of time-averaged axial velocity is only correctly simulated by the two LES cases. While both LES and PIV results show that the time-averaged axial velocity magnitude decreases along the centerline, RANS predicts a largest negative axial velocity at x=2.4 D_t.

In addition to axial velocity distributions along the centerline, the profiles of time-averaged axial and radial velocities along the radial directions are compared with TR-PIV measured data at five axial stations, i.e. x = 1, 2, 3, 4, and 5 D_t, as shown in Figure 5-11. It should be noted that, for the LDI-60-CW configuration, with three repeated sets of PIV data, the error bars are given as the min/max variations from the representative values. The LES predictions for the time-averaged axial and radial velocity show a better agreement with the experiments than RANS. For axial velocity, compared to LES, RANS model under-predicts minimum axial velocities by 0.1 – 0.2 U_t and maximum axial velocities by 0.2 U_t around the flare exit (at x = 0.5 and 1 D_t). At the stations of the dome region (x = 2, 3, 4, and 5 D_t), RANS simulates slightly stronger reverse flow than LES that gives larger error as compared to by PIV data. Meanwhile, for all time-averaged radial velocity profiles in both LES and RANS, the agreement is generally acceptable in the central region, i.e. in the CRZ core, but is generally worse than time-averaged axial velocity predictions, especially for the LDI-60-CW configuration. Since the radial velocities have smaller magnitudes compared with the axial velocities, the small discrepancies of CRZ bubble predictions could cause relatively larger variations in time-averaged radial velocity predictions.

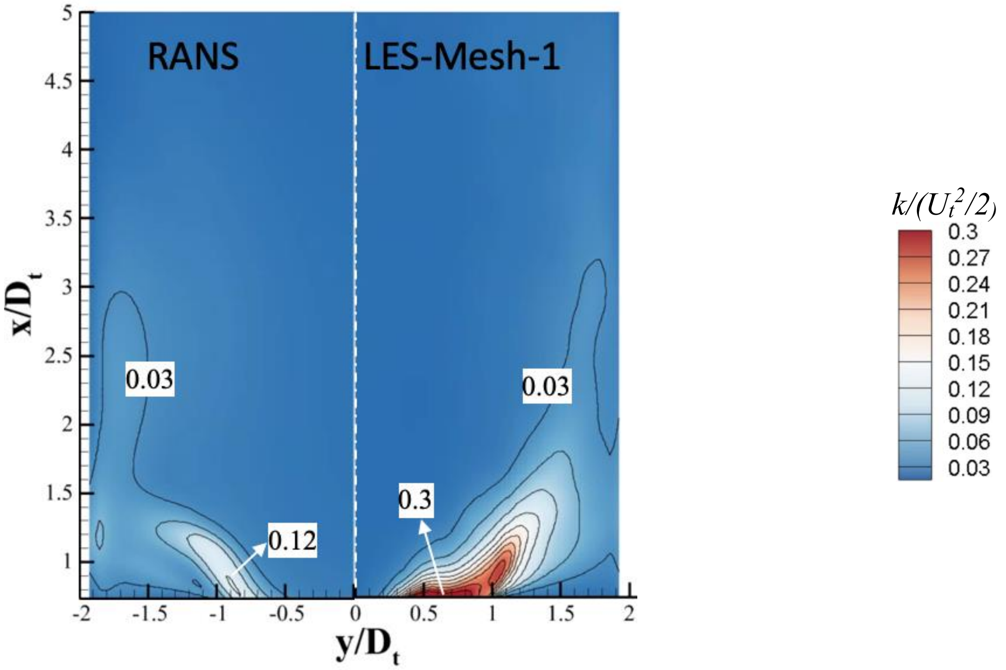

Figure 5-15. Contours of scaled three-dimensional turbulent kinetic energy on x-y plane from RANS and LES in the near-dome region of LDI-60-CW (counter-swirling).

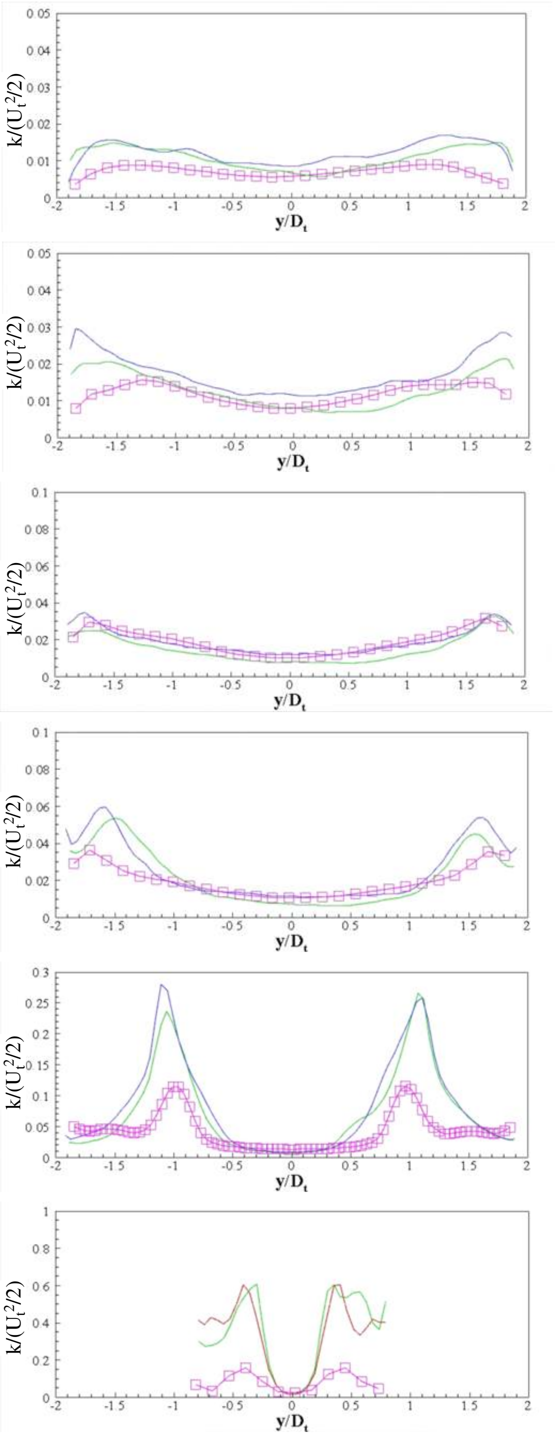

$x = 5\ D_t$

$x = 4\ D_t$

$x = 3\ D_t$

$x = 2\ D_t$

$x = 1\ D_t$

$x = 0.5\ D_t$

Figure 5-16. RANS and LES predicted three-dimensional turbulent kinetic energy distributions along radial direction at $x = 0.5$, 1, 2, 3, 4, and 5 D_t, for LDI-60-CW (counter-swirling).

Turbulent kinetic energy (three-dimensional), k, is quite important in determining flow and flame performance of LDI. The k contours of RANS and LES cases are plotted in Figure 5-15.

Near the flare exit, RANS predicts much lower *k* values than LES. Additionally, the highly turbulent region denoted by $k/(U_t^2/2)$=0.09 in RANS gives a smaller expansion angle from the axis centerline (y=0) than that of LES, which is similar to the expansion angle denoted by contours of measured RMS axial and radial velocities in Figure 5-8. More detailed comparisons of k values are plotted in Figure 5-16 as radial profiles at various axial stations. At the stations of x = 0.5 and 1 D_t, where flow is highly turbulent, RANS under-predicts greatly compared to LES, which might contribute to large inaccuracy in mean flow predictions.

The RANS-Mesh-1 case predicts the effective area of the counter-swirling configuration as 79.57 mm^2. Although the RANS case over-predicts the effective area, with a larger relative difference 3.8%, compared to less than 3% in the LES cases, the levels of agreement of effective area for all the RANS and LES cases are considered adequate (less than 10% [86]) to capture the experimental rig geometry. For the comparisons of CRZ bubble dimensions as shown in Figure 5-13, the experimental data of LDI-60-CW sees this contour closing at 4.23 D_t, a feature which is captured well by both LES-Mesh-1 (closing at 4.28 D_t) and LES-Mesh-2 (closing at 4.17 D_t). However, the RANS-Mesh-1 case simulates a larger CRZ and predicts the closure location at 4.49 D_t, much worse than the LES predictions.

In summary, both LES and RANS models are able to predict CRZ flow pattern in LDI-60-CW configuration. However, the obvious inaccuracy of CRZ bubble size, incorrect axial velocity trend along the centerline, and low turbulent kinetic energy from the RANS modeling might not be acceptable for LDI flame simulations that are more sensitive to flow predictions.

5.3.4 Effect of different sub-grid scale (SGS) models in LES

The SGS models predict the effect of sub-grid scale (SGS) motion on the bulk flows. This section investigates the impact of different SGS models on turbulent flow simulations of the LDI-

60-CW configuration. Figures 5-17 and 18 exhibit a comparison of the LES results using Dynamic-Structure or Dynamic-Smagorinsky SGS model, where *U, V, u,* and *v* profiles are displayed at the axial stations $x = 0.5$, 1, 2 and 4 D_t and validated against PIV data. The simulations were performed on Mesh-1, where SGS model contributes higher portion of sub-grid modelled TKE than the case using Mesh-2. From these comparisons, all velocity components are predicted almost identically for all the four axial stations. The gross features of the flow in the LDI-60-CW configuration appear independent of the SGS models, which might be due to the highly resolved portion of turbulent TKE such that the SGS only contributes a very little portion (less than 4%).

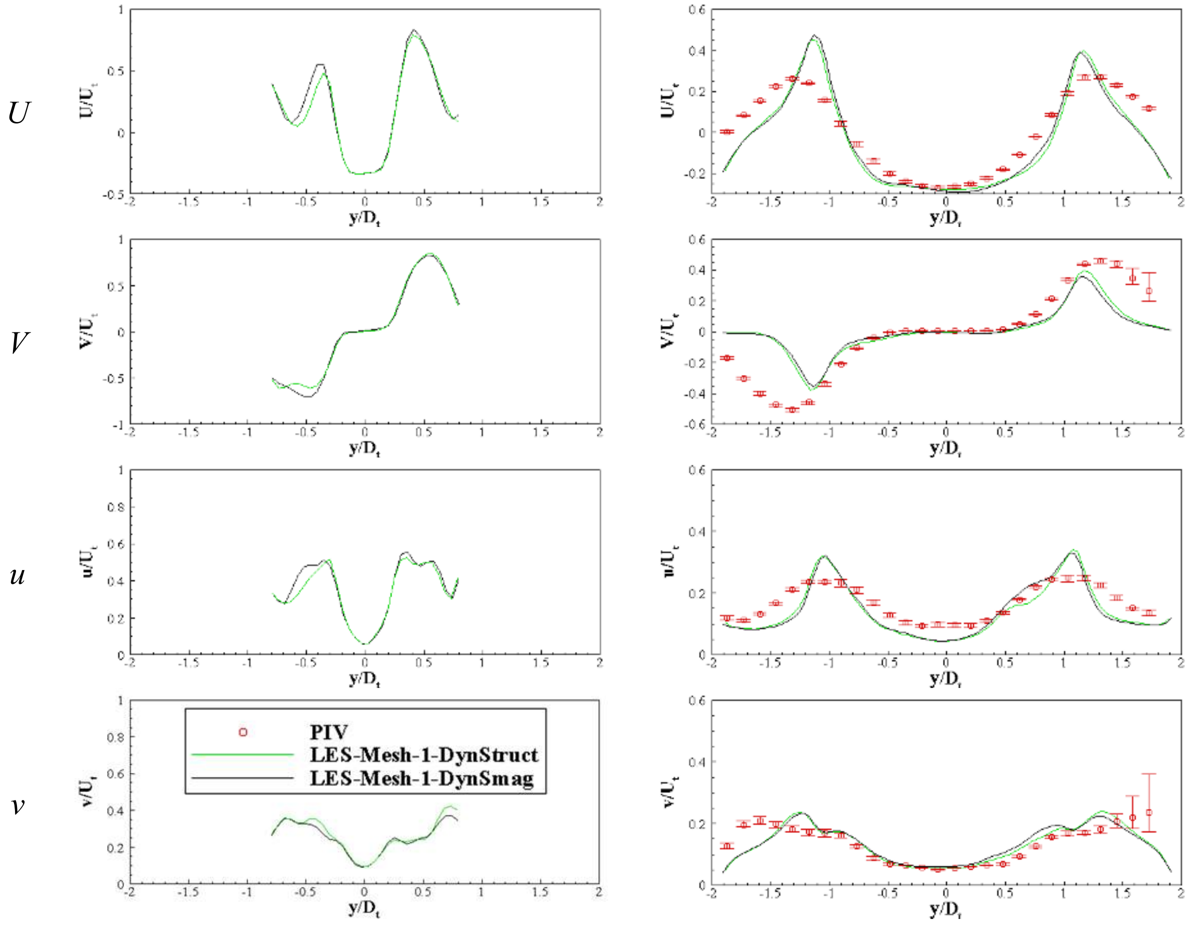

$x = 0.5\ D_t$ $x = 1\ D_t$

Figure 5-17. Comparisons of Dynamic-Structure and Dynamic-Smagorinsky SGS models using velocity components along radial direction at $x = 0.5$ and 1 D_t for LDI-60-CW. “DynStruct” presents the results of LES using Dynamic-Structure SGS; “DynSmag” presents the results of LES using Dynamic-Smagorinsky SGS. Error bars of PIV results are from min/max variations of repeated tests.

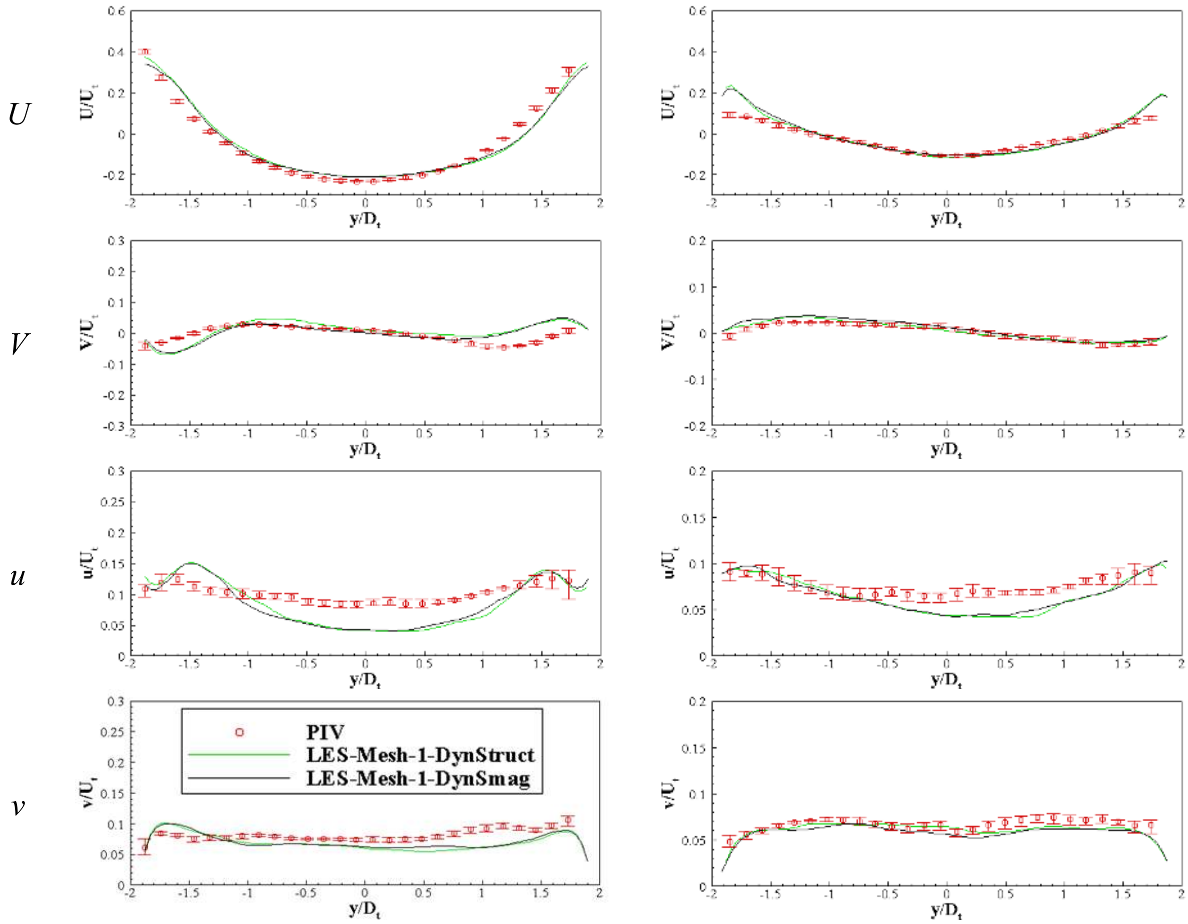

$x = 2\ D_t$ $x = 4\ D_t$

Figure 5-18. Comparisons of Dynamic-Structure and Dynamic-Smagorinsky SGS models using velocity components along radial direction at x = 2 and 4 D_t for LDI-60-CW.

5.3.5 LES for co-swirling configuration and effect of relative swirling direction on flow field

The effect of the relative swirling directions of OAS and IAS swirling flows on the mixer dynamics is explored by switching the orientation of the OAS vane-direction from CW to CCW, while the IAS vane always orientates CCW, such that the OAS and IAS air flows generate counter- and co-swirling flows, respectively. Besides the overall comparisons of mean and RMS velocity contours shown in Figures 5-7 and 9, more analysis based on experimental data and LES results of co-swirling is made for both understanding flow characteristics and validating the CFD performance.

For the co-swirling configuration, i.e. LDI-60-CCW, the measured A_e is 77.10 ± 0.20 mm^2. LES-Mesh-1 of LDI-60-CCW predicts 76.22 mm^2, which under-predicts marginally by 1.1% from the experimental measured value. For the CRZ bubble shown in Figure 5-19, the PIV measurement show that -0.1 U_t contour closes at 3.75 D_t, which is accurately predicted by LES-Mesh-1 of LDI-60-CCW (3.83 D_t). Thus, the co-swirling LES case not only qualitatively predicts the CRZ bubble shape, but also accurately simulates the closure location of -0.1 U_t CRZ bubbles. As shown in Figure 5-20 for the LDI-60-CCW configuration, the LES predicts the time-averaged axial velocity very closely to the PIV measurements.

In addition to the recirculation zone metrics and axial velocity distributions along the centerline, the profiles of time-averaged and RMS axial and radial velocities along the radial directions are compared with TR-PIV measured data at five axial stations, i.e. x = 1, 2, 3, 4, and 5 D_t, as shown in Figures 5-21 and 22 for the co-swirling flow. In general, the mean velocities are simulated in good accuracy by LES. In addition, the trend of RMS velocities are generally captured, but the magnitudes are under-predicted by LES. Taken the validations of counter- and co-swirling flows, the LES prediction for co-swirling flow seems to be more accurate than that for the counter-swirling case discussed previously. The reason could be due to a stronger shear layer existed in the counter-swirling case, which has a larger axial velocity gradient as shown in Figure 5-23. Since LES is able to satisfactorily capture flows in both co- and counter-swirling configurations, the effect of relative swirling direction on LDI performance is analyzed based on the three-dimensional LES results.

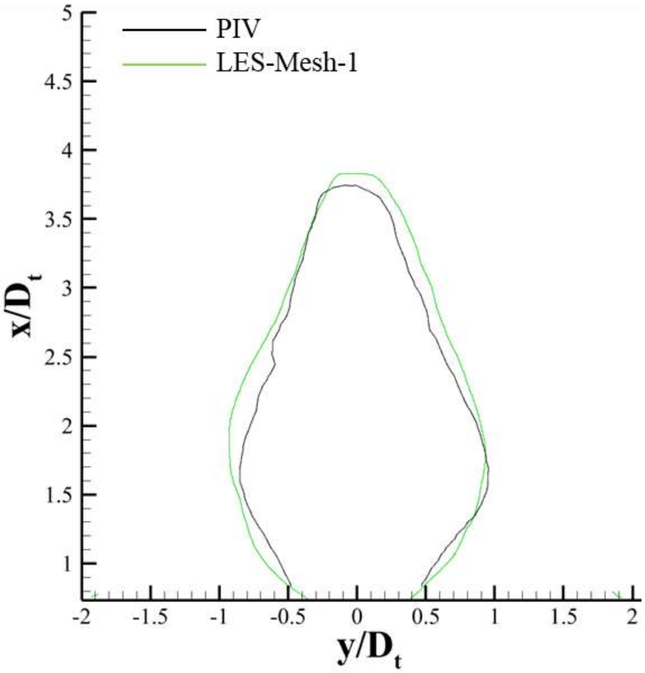

Figure 5-19. Comparison of -0.1 U_t contours on x-y plane between experimental data and simulation results for LDI-60-CCW (co-swirling).

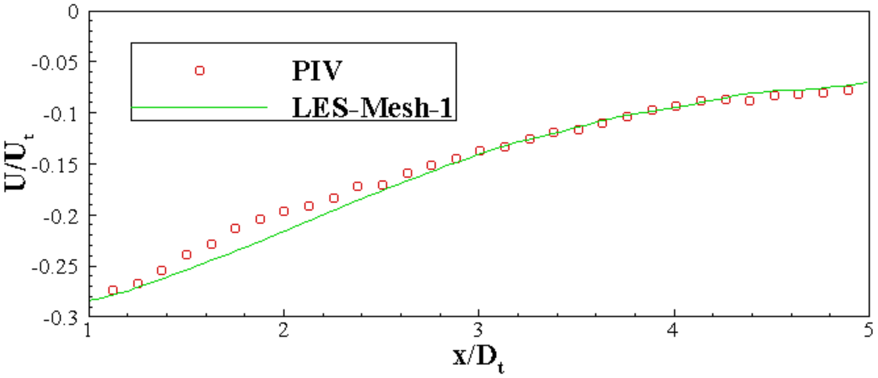

Figure 5-20. Comparison of time-averaged axial velocity profiles along the centerline (*y*=0) for LDI-60-CCW (co-swirling).

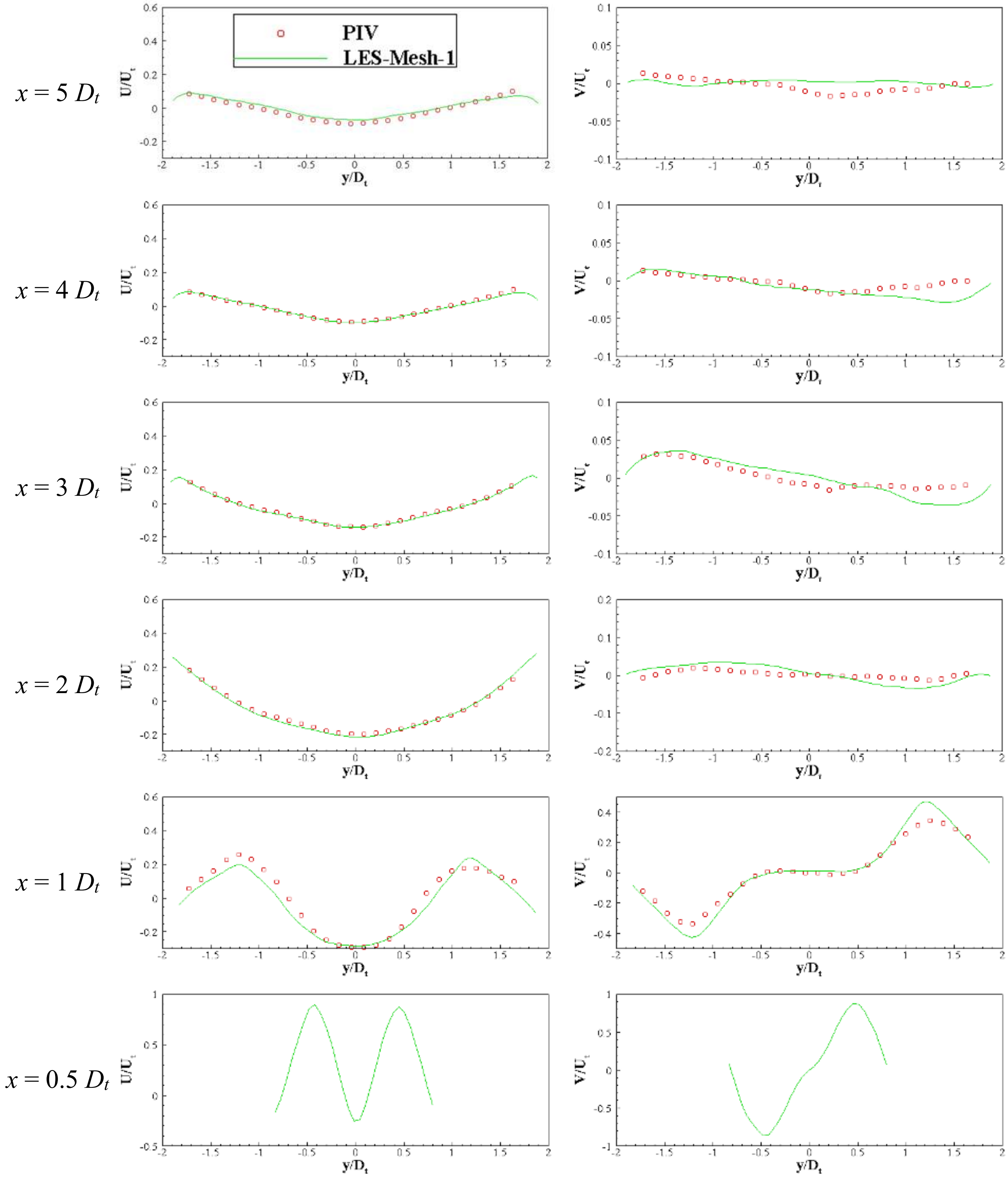

Figure 5-21. Measured (PIV) and LES predicted *U* (left) and *V* (right) profiles using Mesh-1 along radial direction at $x = 0.5$, 1, 2, 3, 4, and 5 D_t in LDI-60-CCW.

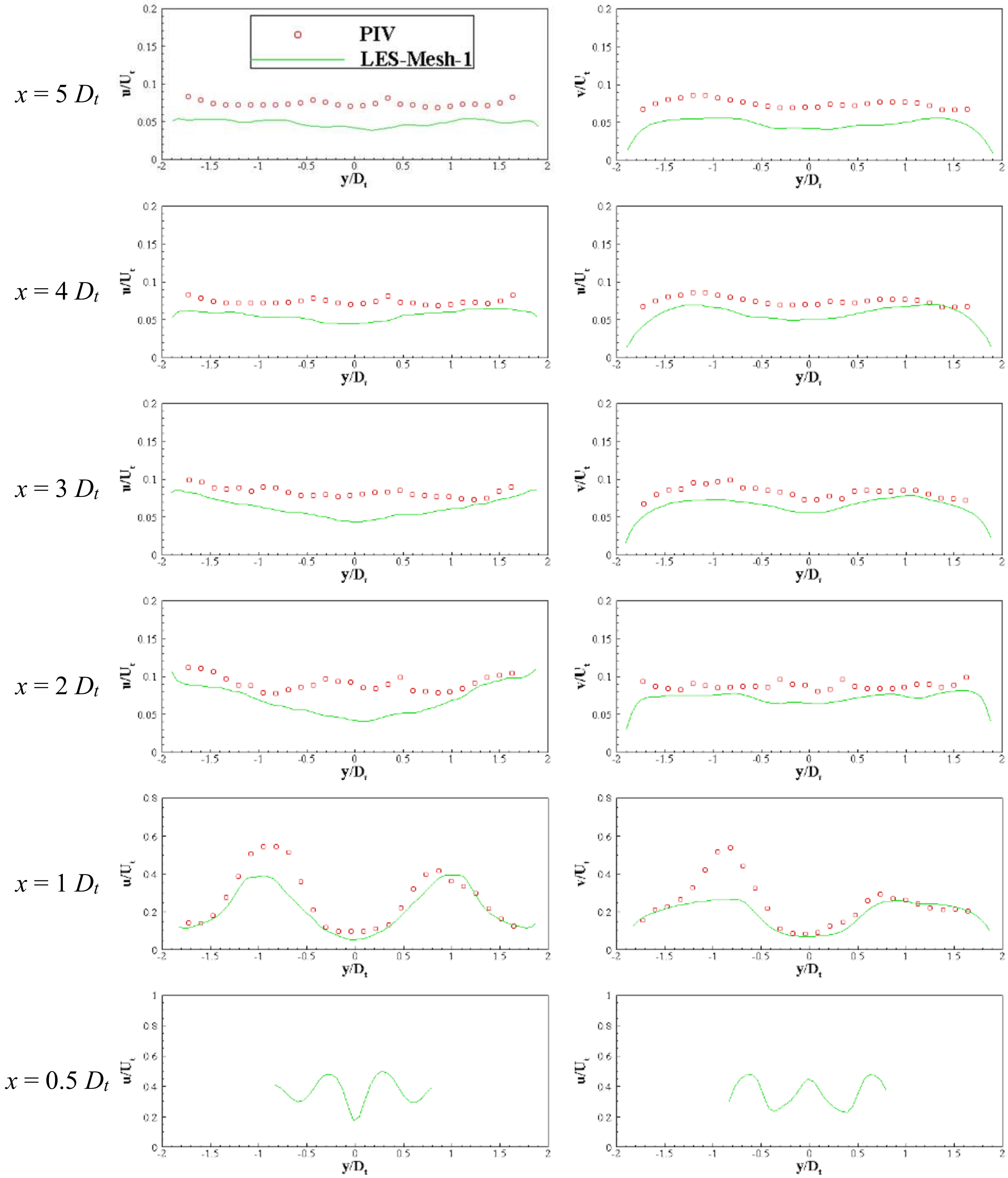

Figure 5-22. Measured (PIV) and LES predicted fluctuating axial and radial velocity profiles, *u* (left) and *v* (right), profiles using Mesh-1 along radial direction at *x* = 0.5, 1, 2, 3, 4, and 5 D_t, for LDI-60-CCW (co-swirling).

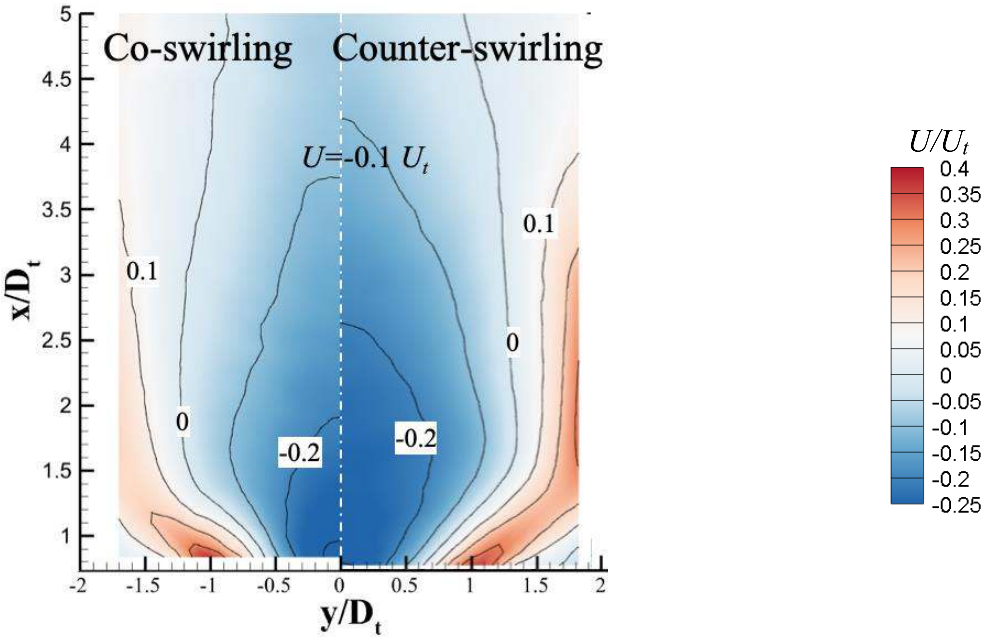

Figure 5-23. Comparison of PIV measured time-averaged axial velocity contours between LDI-60-CCW (co-swirling) and LDI-60-CW (counter-swirling). The increment between velocity contour-lines is 0.1 U_t.

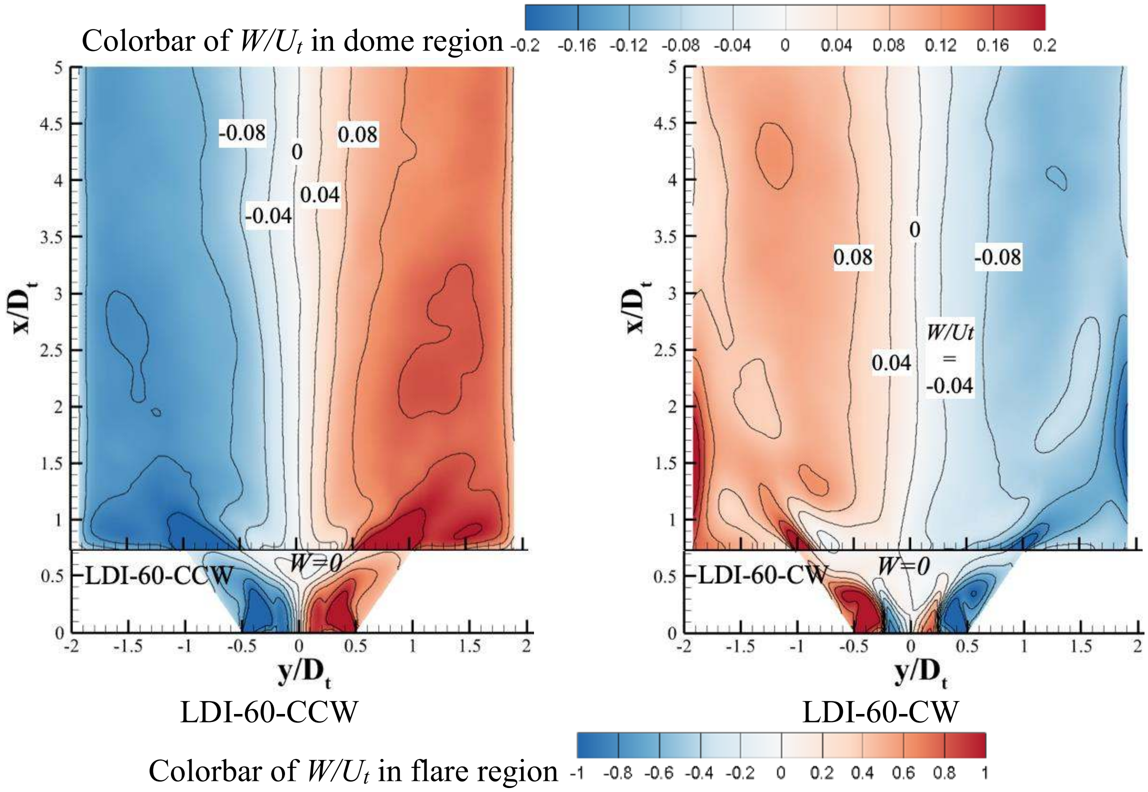

Figure 5-24. Comparison of time-averaged tangential velocity in the flare region on *x-y* plane between LES results of LDI-60-CCW (co-swirling) and LDI-60-CW (counter-swirling), using Mesh-1. For the flare region, the increment between velocity contour-lines is 0.2 U_t; for the dome region, the increment between velocity contour-lines is 0.04 U_t.

As shown in Figure 5-24, the distributions of the time-averaged tangential velocity (W) in the flare and dome regions are compared between co- and counter-swirling configurations, from LES using Mesh-1. To clearly illustrate the tangential velocity distributions, two different colorbars are used in the flare and dome regions, respectively. In the dome region, the directions of tangential velocities are determined by the OAS flow direction, which is due to higher tangential velocity momentum from the OAS flow than that from the IAS flow. Near the throat ($x = 0$), the swirling flows from IAS and OAS just start to merge together. As the time-averaged tangential velocity is determined by the rotating orientation of the swirler vanes, the co-swirling configuration has the same tangential velocity direction, while the counter-swirling configuration has opposite swirling flow directions. For this reason, besides the strong shear between the inflow from venturi and the reverse flow from CRZ, counter-swirling flow has another strong shear layer between the IAS and OAS swirling flows near the fuel injector tip, which further facilitates the liquid film/droplet breakup for practical spray applications. Meanwhile, the co-swirling flow creates a longer CRZ as shown in Figure 5-25, which is more susceptible to flame oscillation [87]. Fu et al. [34] pointed out that stronger swirling flow creates longer CRZ. Swirl number is routinely used to characterize swirl strength as shown in Eq. 3-2. The distributions of swirl numbers and axial fluxes of tangential and axial momenta of LDI-60-CW and LDI-60-CCW inside flare region are presented by Figure 5-26. To compare the magnitudes of these values, the absolute values of swirl number and momentum fluxes are taken and plotted here. The co-swirling flow has slightly higher swirl numbers than counter-swirling configuration within the flare, which is majorly contributed by the higher axial flux of tangential momentum as presented by green lines in Figure 5-26. Therefore, LDI-60-CW has the advantages over LDI-60-CCW that the counter-swirling flow creates an extra strong shear layer near throat to facilitate liquid fuel mixing; the lower swirl strength and more compact CRZ in LDI-60-CW could reduce flame oscillations.

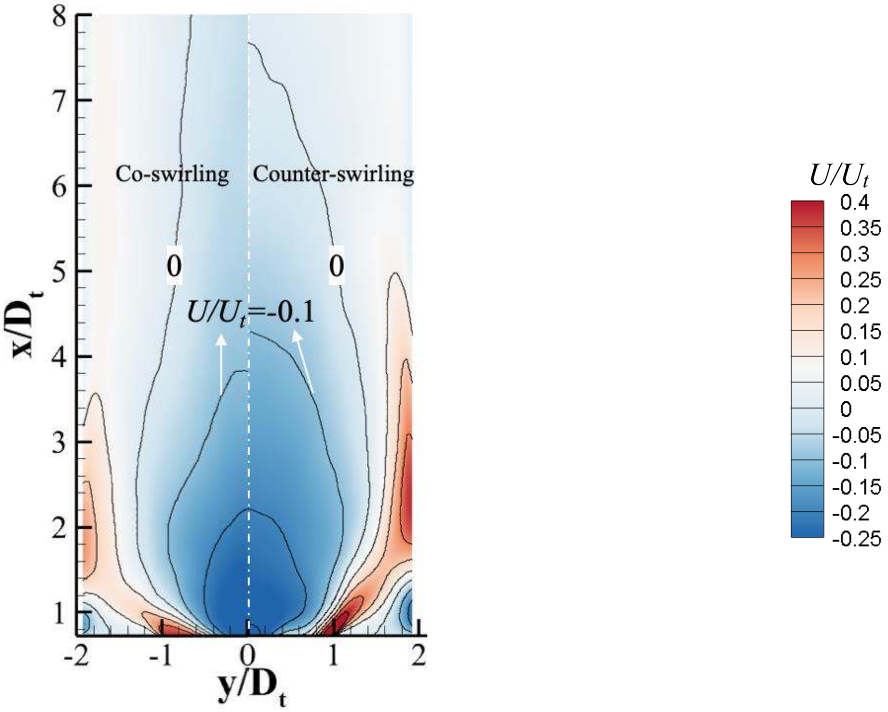

Figure 5-25. Comparison of time-averaged axial velocity on x-y plane between LES results of LDI-60-CCW (left) and LDI-60-CW (right), using Mesh-1. The increment between velocity contour-lines is 0.1 U_t.

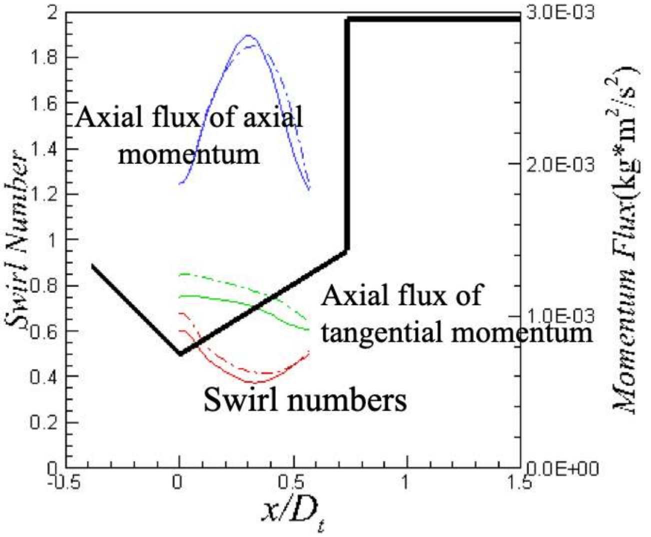

Figure 5-26. Distributions of swirl numbers and axial fluxes of axial and tangential momenta of the LDI-60-CCW (co-swirling) and LDI-60-CW (counter-swirling) configurations from LES results, using Mesh-1. Solid lines: counter-swirling; dashed lines: co-swirling; bold solid lines: schematic of half venturi-flare-dome.

5.4 Concluding Remarks

In this chapter, isothermal turbulent swirling flows in the single-element LDI concept combustors are investigated numerically and experimentally to understand the flow dynamics and identify the best practice in simulating the characteristic turbulent swirling flows. The main flow structures in the LDI-60˚ OAS configurations include center and corner recirculation zones, which are successfully predicted by both RANS and LES models. LES can predict the effective area, the center recirculation zone size, and the time-averaged velocity distributions more accurately than RANS. Additionally, the mean and RMS velocity profiles along various axial stations are matched well between LES results and PIV data. A grid independence study is also conducted to find adequate grids in LDI flow simulation. The present resolution of computation grids results in a very high percentage of resolved turbulent kinetic energy, in which the SGS model's impact is negligible in bulk flow simulation. Two LDI configurations are simulated, i.e. counter- and co-rotating axial swirlers with 60˚ OAS and IAS vanes. Due to the higher axial flux of tangential momentum, the co-swirling configuration, LDI-60-CCW, has greater swirl strength and creates a longer CRZ. At the same time, the opposite direction between IAS and OAS swirling flows in LDI-60-CW creates an extra strong shear layer near the throat, facilitating fuel mixing. Future efforts investigating the individual impacts of various features of the LDI swirler geometry will utilize the mesh generation strategy and modeling methodologies introduced herein to describe and evaluate the performance of alternative LDI-relevant swirler geometries.

CHAPTER 6 AN EXPERIMENTAL AND CFD STUDY ON REACTING COUNTER- AND CO-SWIRLING FLOWS IN LDI

6.1 Introduction

Numerical simulations have been foreseen to be capable of tremendously improving the design of gas turbine combustors in the very near future. Recent developments in numerical schemes, turbulence models, as well as the continuous increase of computing resources have enabled Large Eddy Simulation (LES) to be applied to realistic non-reacting flow simulations in industrial applications. However, the full-spectrum simulation of the gas turbine combustion process still remains extremely challenging due to its massive computational cost. Until now, a few combustion models have been developed in order to provide an economic approach of flame simulation and investigate its applicability for engineering applications. The Flamelet Generated Manifold (FGM) model [88] is based on the idea that a multi-dimensional flame can be represented by a set of 1D flamelets [89] and uses the tabulated chemistry method in order to reduce computational time compared. The FGM models have been widely applied to gas turbine combustors [90–92], but rarely utilized to the research of Lean Direct Injection (LDI) combustion. In this chapter, the FGM technique is adopted and fully explored to investigate the combustion characteristics that are typically observed in LDI combustion. The capability of RANS-FGM and LES-FGM models is first validated against experimental measurements of PIV and OH* chemiluminescence. Then the mechanism of flame stabilization in LDI combustion is illustrated with the aid of flow and flame field information from LES-FGM predictions. Additionally, the flame responses, especially the lift-off related process as a function of overall equivalence ratio are researched by LES-FGM modeling. A numerical methodology at affordable computational cost to predict the flame behaviors in LDI combustion is demonstrated.

6.2 Experimental and Numerical Description

6.2.1 Experimental setup

For the present study, helical 60˚ OAS vanes are installed with clockwise (CW) or counter-clockwise (CCW) rotation direction (looking from the upstream side), while the IAS vanes are fixed at a 60˚ counter-clockwise (CCW) rotation, forming a counter- or co-swirling shear flow between the IAS and OAS. The counter-swirling configuration is referred to hereafter as the LDI-60-CW configuration and the co-swirling configuration is referred to hereafter as LDI-60-CCW configuration.

Multiple measurement techniques are employed in this work to compare the flow field and flame structure. A two-dimensional TR-PIV system is used to obtain axial-radial velocity data with the laser sheet aligned with the center plane of the burner. The reacting flow field measurements are performed at a 3% pressure drop (ΔP) across the LDI injector and combustor chamber. The Reynolds number (Re) based on ρ_{air}, U_t, and D_t is estimated at 35,000. The capture area for the mean velocity map is 50 mm × 60 mm, focused on the area from the injector dump plane to 60 mm downstream. Mean axial-radial (U-V) velocity maps are processed from the full 1-second collection period, at repetition rate of 5 kHz. To delineate the reaction regions and qualitatively compare flame structure, OH^* chemiluminescence signals are imaged.

6.2.2 Computational approach and modeling

6.2.2.1 Turbulence modeling, combustion modeling and boundary conditions

RANS and LES models are utilized to explore the turbulence effect on the reacting LDI flow investigations. As best performance amongst RANS turbulence closures in predicting CRZ of swirling cup modeling [54], SKE is selected for RANS cases. In LES, the sub-grid tensor term is modelled using Dynamic Structure SGS. For the near-wall turbulence modeling, RANS and LES use standard wall function [59] and the Werner and Wengle wall model [60], respectively.

For a consideration of saving computational cost, Flamelet Generated Manifold (FGM) is used as combustion model, in which a low-dimensional manifold is formed from solutions of the so-called flamelet equations. In LDI combustion, as the air and fuel streams are injected separately from air swirlers and fuel injector tip, respectively, the flame is considered as a diffusion flame. Full kinetics flamelet solutions are obtained by means of a specialized 1D flame code built in CONVERGE CFD [51], coupled with the GRI-Mech 3.0 mechanism [62], which consists of 325 elementary reactions and 53 species.

The inlet air and fuel boundary conditions for the LDI combustor calculations are chosen to be placed at the inlet of the air manifold and fuel tip, respectively. The mass flow velocity boundary condition is used as the inlet boundary condition, which is a special case of the Dirichlet velocity boundary condition. The mass flow rate used in simulations is the same as that used in the experiments, which is measured by calibrated choked nozzles. For LES, the fluctuating inflow boundary is imposed at the inlet. It uses the concept of digital filtering to generate turbulent fluctuations, which are then superimposed on the inflow velocity profile. The air flow fluctuation intensity, 13%, is determined from the PIV measurement on the manifold inlet under experimentally-relevant mass flow rates. Input of fluctuation length scale is determined by the dimensions of the fine-mesh inserts, which are used to uniformize air flow in the air manifold. The outlet is placed at the physical exit of combustor. At the outlet boundary, zero-gradient boundary condition is applied for the velocity components, along with a prescribed constant atmospheric pressure condition. Adiabatic thermal boundary condition is utilized for all the walls.

6.2.2.2 Computational domain and mesh generation

The three-dimensional computational domain for LDI configurations consists of air inlet manifold, swirler-venturi assembly, and combustion chamber, as shown in Figure 6-1. The grids are generated by cut-cell Cartesian grid method [51,52], which allows the use of orthogonal grids by eliminating the need for the grid to be morphed with the geometry while precisely capturing the boundary shapes. The base grid size, Δ_0, is 1 mm, which is applied to the regions of air manifold and downstream of combustor, as outlined in Figure 6-1. To balance the computational cost and the need to resolve sufficient scales of turbulence, the fixed embedding is applied to better resolve the flows within the swirlers and venturi ($\Delta_2 = 0.25$ mm) and the near-dome region ($\Delta_1 = 0.5$ mm). In addition, to resolve the flow field, extra mesh resolution is included during runtime via an adaptive mesh refinement (AMR) technique on the basis of local temperature and velocity gradients, which can be used to refine the mesh in the steepest gradient regions while coarsen the mesh in shallow gradient regions [51]. For LDI simulations, the mesh is refined in shear layers, flame front, and recirculation regions as shown in Figure 6-1. A minimum cell size of $\Delta_3 = 0.25$ mm is used with AMR, resulting in a total count of 6 million cells for current LDI simulations.

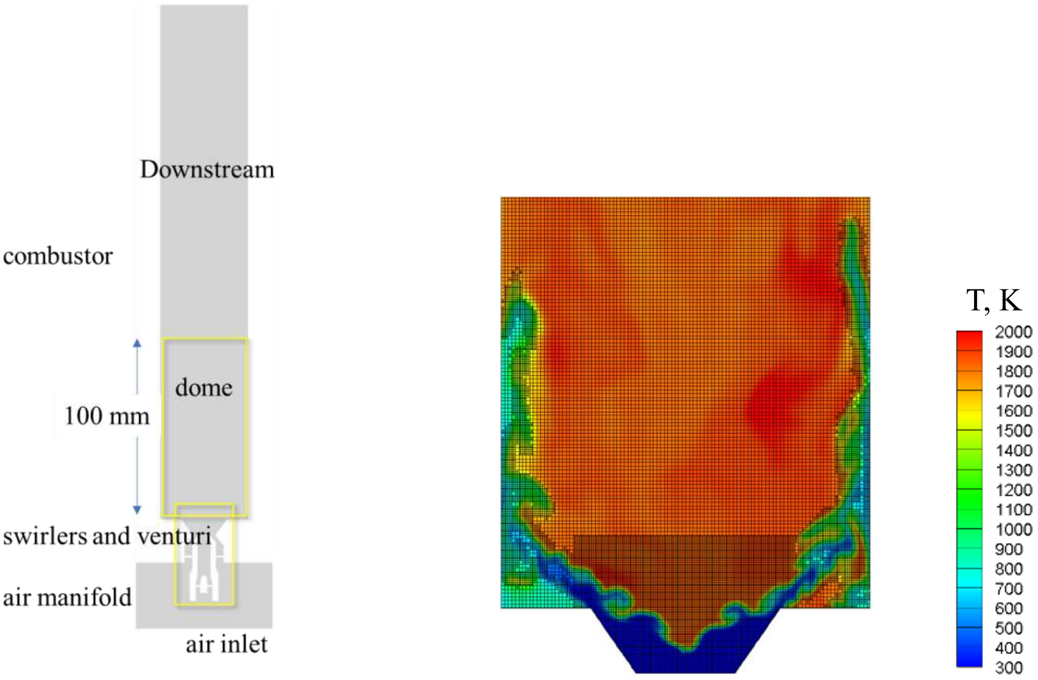

Figure 6-1. Computational domain (left) and close-up look of mesh generation with AMR near the venturi exit (right) colored by instantaneous temperature field.

6.2.2.3 Numerical Setup

In this chapter, the finite volume-based compressible flow solver CONVERGE is adopted, and a second-order-accurate spatial discretization scheme is employed for the governing conservation equations. A fully implicit first-order-accurate time integration scheme is used so as to keep numerical stability in LES cases, and the transport equations are solved with the PISO method. For each time-step, the variable time-step is calculated automatically base on the maximum convection CFL number, the speed of sound CFL number and the diffusive CFL number, in the range of 10^{-8} s to 10^{-5} s. Turbulence statistics is collected over more than three flow-through time in LES cases. The data is collected over more than three flow-through time for LES cases to achieve converged turbulence statistics, and the turbulence statistics collection starts at the second flow-through time after flow field initialization.

6.3 Results and Discussion

6.3.1 Comparison of RANS-FGM and LES-FGM on reacting counter-swirling flow predictions

As the second part of the CFD studies on LDI simulations, the reacting flows are predicted using the FGM model. To check the accuracy of combustion model and turbulence-combustion interaction (TCI), the simulated velocity and species fields using RANS-FGM and LES-FGM in the counter-swirling reacting flows are validated against PIV and chemiluminescence data.

For the LDI-60-CW configuration, the contours of time-averaged axial velocity under overall equivalence ratio of $\phi = 0.65$ are compared between PIV data and simulation results in Figure 6-2. A center recirculation zone (CRZ) exists in both experimental measurement and numerical predictions. Despite of the similarity of flow structures between PIV data and simulation results, using $U = -0.1\ U_t$ as the indicator of the CRZ bubble size, RANS-FGM and LES-FGM both under predict the length of CRZ.

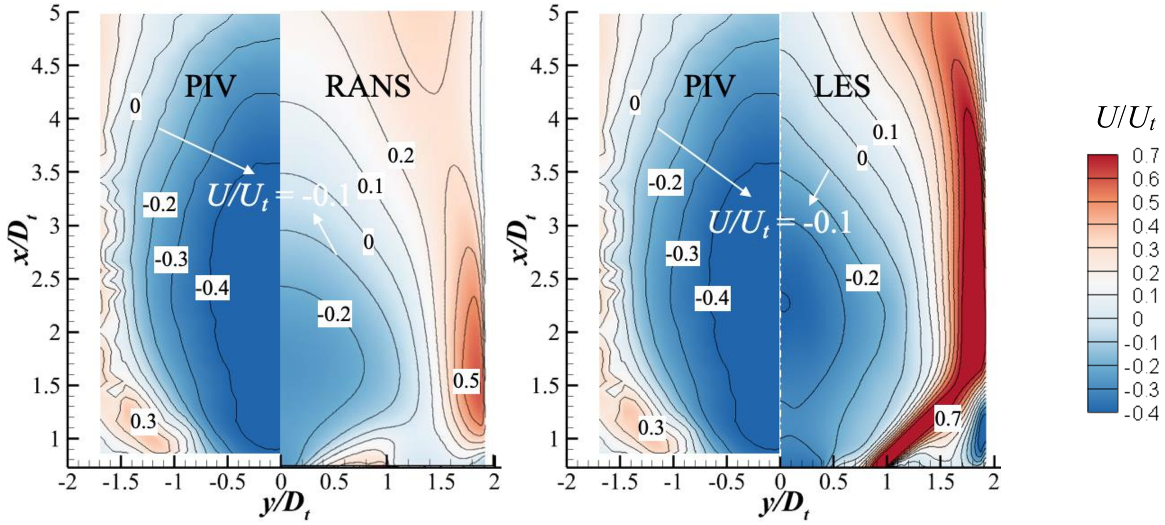

Figure 6-2. Comparison of time-averaged axial velocity between experimental data (PIV) and CFD predictions (left: PIV vs. RANS and right: PIV vs. LES) for reacting flow of counter-swirling at ϕ=0.65.

Further comparison of time-averaged axial velocities in the LDI-60-CW configuration are carried out along the axial centerline (y=0) in Figure 6-3. Near the flare exit, both PIV and FGM simulation exhibit stronger reverse flows at reacting condition than that at non-reacting condition. Unlike the well-matched cold flow prediction, LES-FGM model over-predicts the U profile, as large as 0.1 to 0.2 U_t, compared to the PIV data along y=0. It is likely that the inaccurate TCI or/and tabulated FGM model gives this discrepancy. The RANS-FGM is inadequate to simulate the time-averaged axial velocity along the centerline, where RANS-FGM over-predicts as large as 0.2 - 0.3 U_t in Figure 6-3.

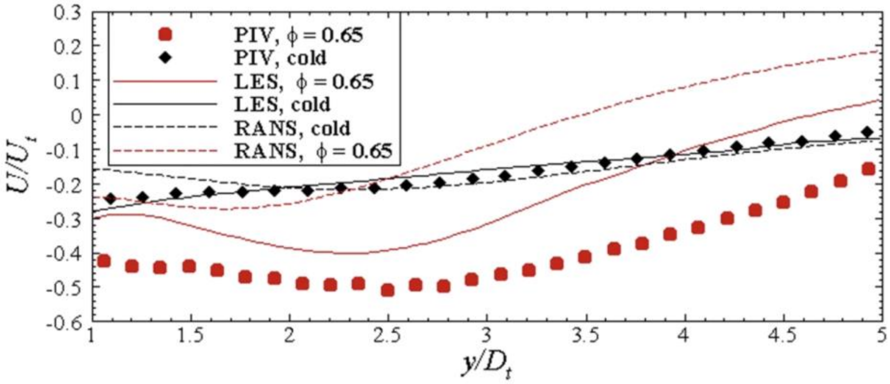

Figure 6-3. Simulated time-averaged axial velocity comparison with PIV data in counter-swirling flow along the centerline.

The advantage of LES-FGM over RANS-FGM is more obvious when comparing the radial profiles of time-averaged axial velocities at the axial stations of $x/D_t = 1, 2, 3, 4$, and 5, as shown in Figure 6-4. First, LES-FGM predicts the correct trends for all axial velocity profiles compared with PIV. Second, at the station near the flare exit, $x/D_t = 1$, LES-FGM accurately captures the locations of minimum and maximum axial velocities. For the time-averaged radial velocity, LES-FGM predicts radial velocity directions the same as PIV measured data, while RANS fails to simulate the radial direction at $x/D_t = 2$. Due to large discrepancies in the CRZ dimensions, the mean radial velocity predictions lack accuracy. Figure 6-8 validates RMS velocity values of LES-FGM by PIV data. LES-FGM generally simulates the fluctuating velocities at the similar magnitude of the PIV data. The radial profiles of three-dimensional turbulent kinetic energy (k) are plotted and compared for RANS-FGM and LES-FGM in Figure 6-6. Similar to the outcome of the non-reacting cases, around the flare exit, i.e. $x/D_t = 0.5$ and 1, RANS simulation under-predicts k compared to the corresponding LES case.

Besides the flow field, the flame structure is also checked against experimental data. OH* chemiluminescence, as an indicator of the flame area and intensity [93,94], is experimentally measured to validate the flame pattern and location obtained based on the OH mass fractions of LES prediction, as exhibited in Figure 6-7. Both results from experiments and simulations are time-averaged to illustrate the mean flame region. It is noticed that as OH* chemiluminescence is a line-of-sight (LOS) measurement, the mass fraction of OH is then accumulated along the z-axis to simulate the direction of camera when gathering OH* signals. Since the AMR generates different mesh sizes in three-dimensional (3D) space, a set of in-house codes integrates the 3D data into the two-dimensional (2D) grids ($1\text{x}1\ \text{mm}^2$), with the mass of each cell being taken into consideration. At the same time, the planar distribution of the OH mass fraction on x-y plane is also plotted to check the effect of LOS accumulation on the shape of OH radial distributions. To ease the comparison between OH* signal and OH mass fraction, the OH/OH* intensity is scaled based on its maximum and minimum values.

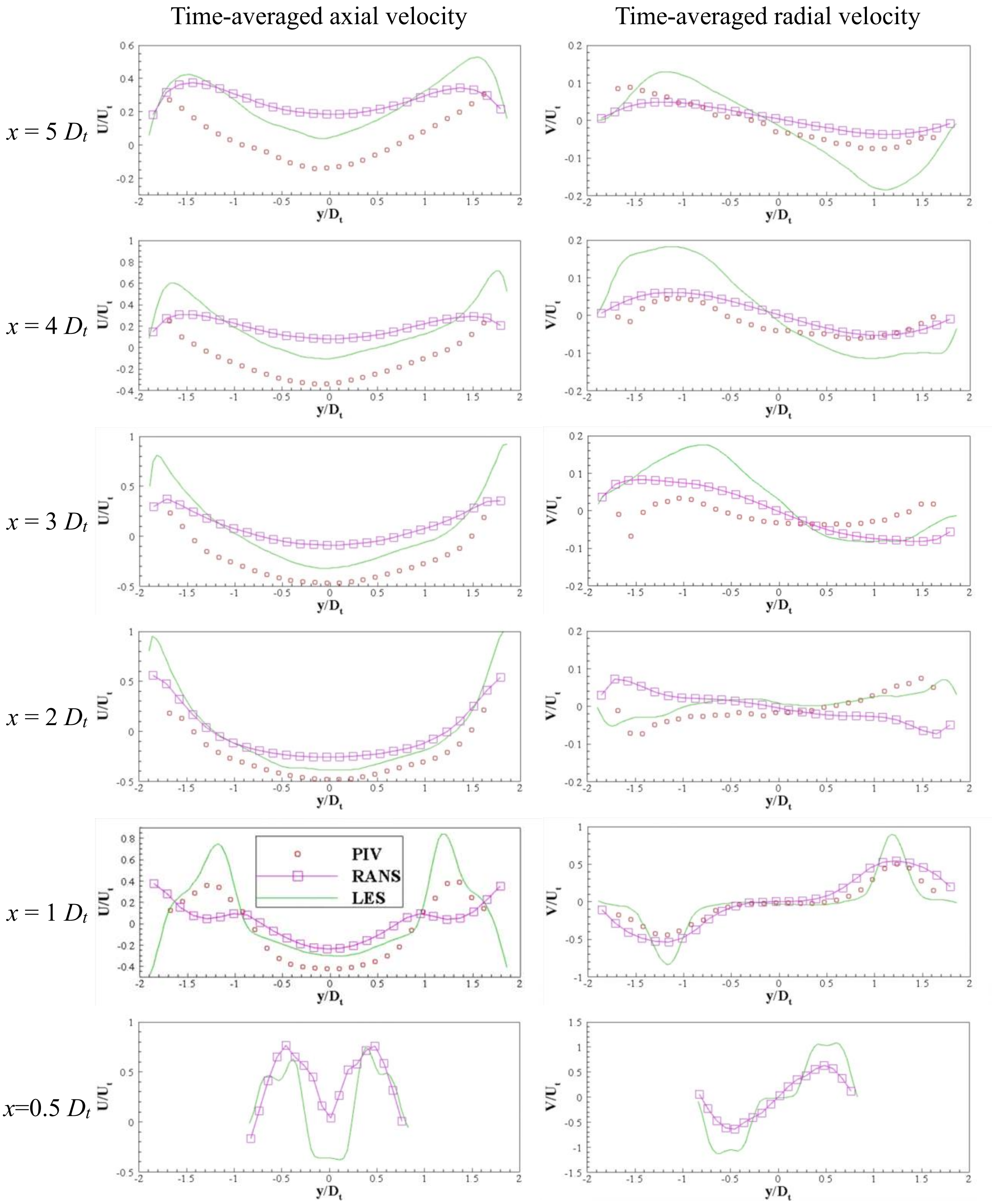

Figure 6-4. Measured (PIV), RANS-FGM, and LES-FGM predicted *U* (left) and *V* (right) profiles along radial direction at x = 0.5, 1, 2, 3, 4, and 5 D_t in LDI-60-CW (counter-swirling).

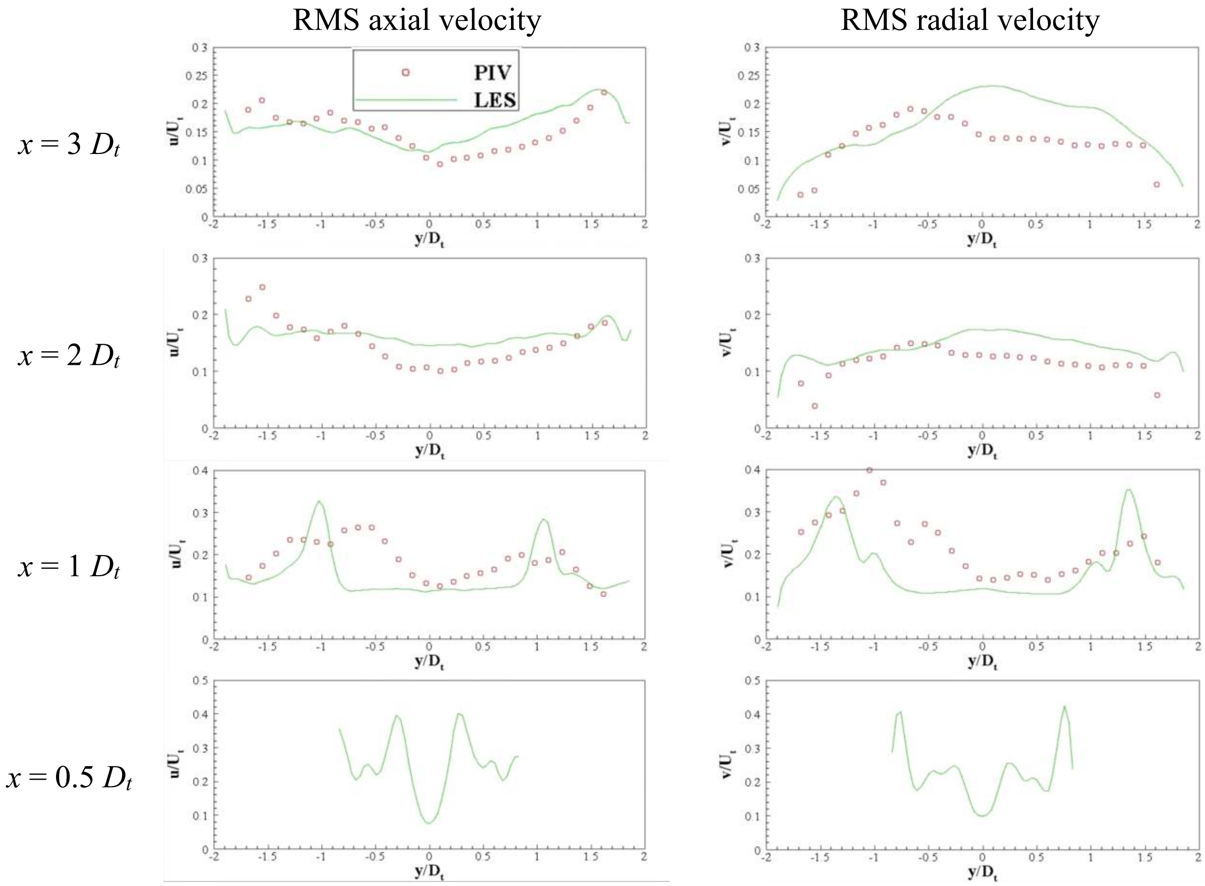

Figure 6-5. Measured (PIV) and LES-FGM predicted fluctuating axial and radial velocity profiles, *u* (left) and *v* (right), along radial direction at $x = 0.5$, 1, 2, and 3 D_t for LDI-60-CW (counter-swirling).

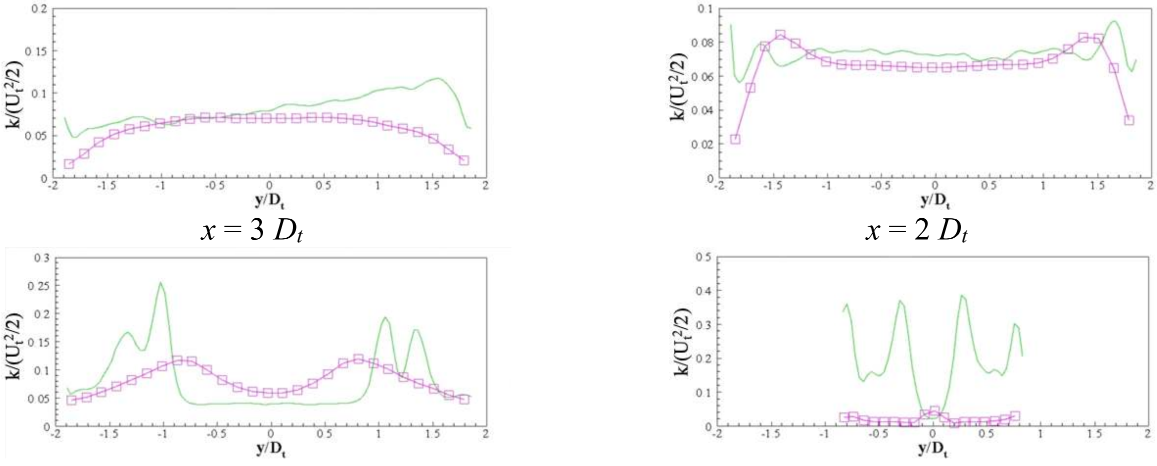
$x = 3\ D_t$ $x = 2\ D_t$

$x = 1\ D_t$ $x = 0.5\ D_t$

Figure 6-6. RANS and LES predicted turbulent kinetic energy distributions along radial direction at $x = 0.5$, 1, 2, and 3 D_t for LDI-60-CW (counter-swirling).

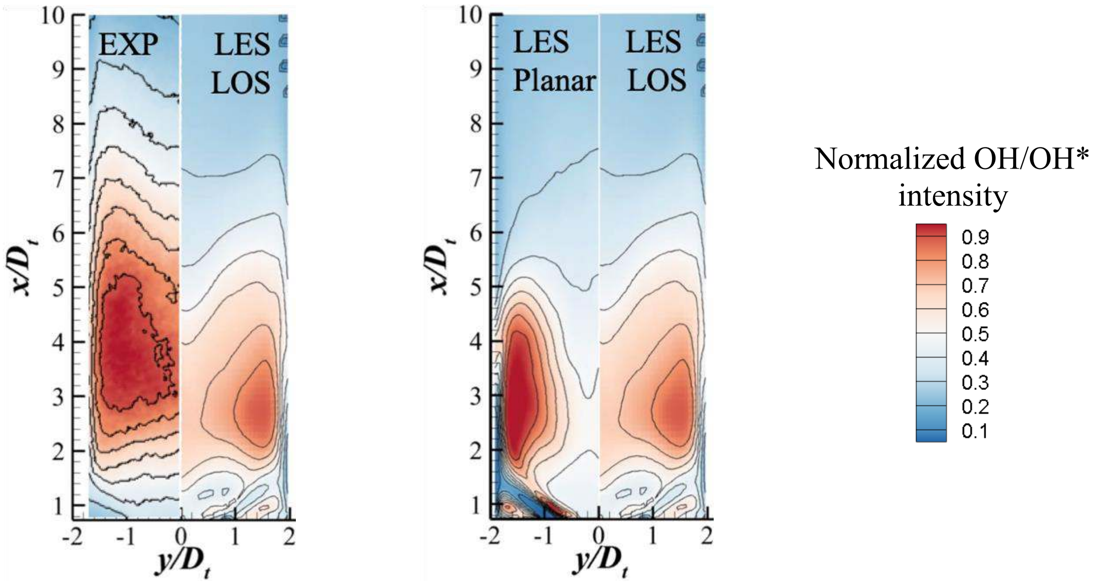

Figure 6-7. Reaction region represented by OH mass fraction or OH* chemiluminescence in LDI-60-CW, at ϕ=0.65. Left: Line-of-Sight averaged mass fraction of OH from LES (LES-LOS) compared with averaged OH* chemiluminescence from experimental measurement (EXP); right: OH distribution on *x-y* plane (LES-Planar) vs. LES-LOS. To compare the results at the same locations, LES-LOS distribution on the right half is mirrored from the simulated values of the left half.

A very similar OH distribution in the axial and radial directions is presented by the LOS results from both experiment and simulation, especially the flame is strongly burning around the CRZ. The mechanism of flame formation can be further explored in the following discussions with more details about flow and flame fields. Here, the difference of experiment and prediction lies in the axial location and corner flames. LES predicts the flame seating closer to the dump plate than the OH* chemiluminescence data. At the same time, obvious corner flame only exists in the LES results. From experimental studies, as overall equivalence ratio increases, flame gets stabilized closer to the dump plate, and corner flames tends to appear as the heat release is stronger. The adiabatic wall condition in LES, which neglects heat loss from flame to environment, could facilitate the flame to sit closer to the dump plate and exist in the corner regions. The OH distribution of LES-Planar has generally the similar shape, but with larger gradients compared to that of LES-LOS contours. In LES-Planar, OH is more concentrated near the CRZ boundary and less distributed in the center of CRZ, which is due to the lack of integration along the "sight" direction. As shown by the similar OH distributions of LES-Planar and LES-LOS, the OH* chemiluminescence, as a LOS measurement, is able to qualitatively reveal the distribution of OH on a cut plane.

The OH* data and LOS OH mass fraction from the RANS-FGM case are compared in Figure 6-8. Unlike LES-FGM, RANS-FGM is not able to simulate the flame shape correctly. In RANS-FGM, the reaction is intensive near the exit of flare, while not so much reaction is indicated by the OH* measurement.

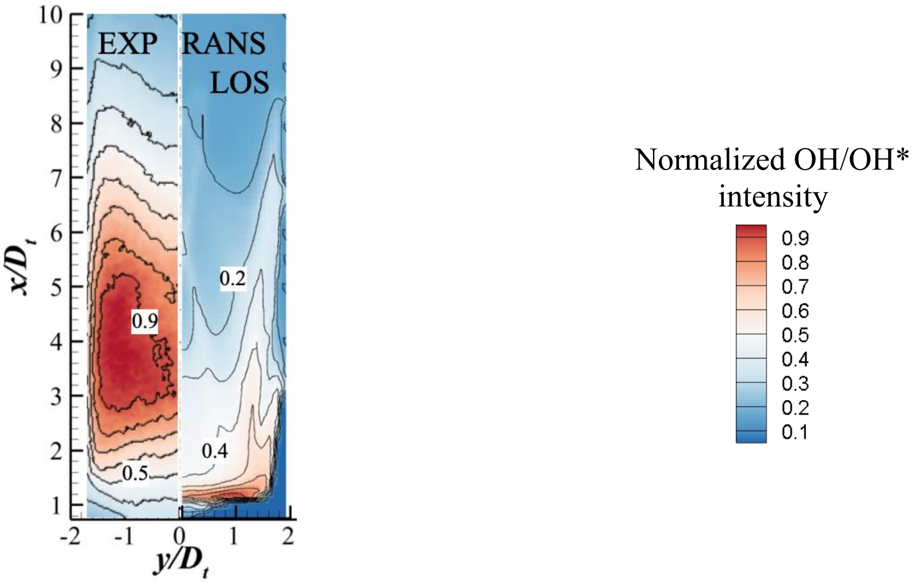

Figure 6-8. Reaction region represented by OH mass fraction and OH* chemiluminescence in LDI-60-CW, at ϕ=0.65. Line-of-Sight averaged mass fraction of OH from RANS (RANS-LOS) is compared with OH* chemiluminescence from experimental measurement (EXP). To compare the results at the same locations, OH distribution on the right half is mirrored from the simulated values of left half.

The contours of averaged axial, radial, and tangential velocities and static pressure are presented in Figures 6-9 and 10 for counter-swirling LES-FGM and RANS-FGM, respectively. The CRZ feature is predicted by both model results. However, RANS-FGM fails to predict a strong shear layer at the flare exit like LES-FGM.

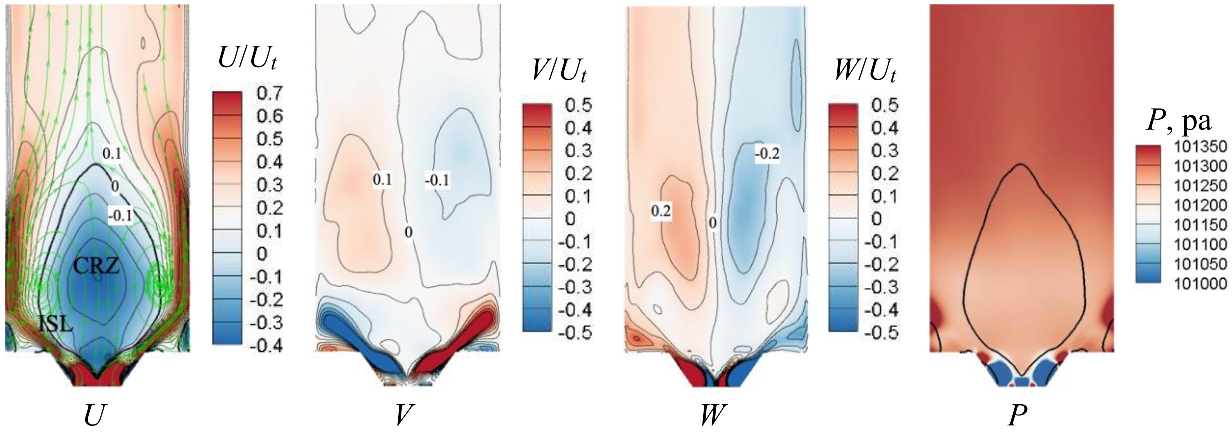

Figure 6-9. Contours of time-averaged axial (U), radial (V), and tangential (W) velocities and static pressure (P) on x-y plane from LES prediction of LDI-60-CW, at ϕ=0.65. "CRZ" and "ISL" stands for center recirculation zone and inner shear layer, respectively. Bold black contours denote the boundary of recirculation zones (U=0). The mean axial velocity contour is overlapped by time-averaged streamtraces (green lines with arrows) derived from mean U-V velocities.

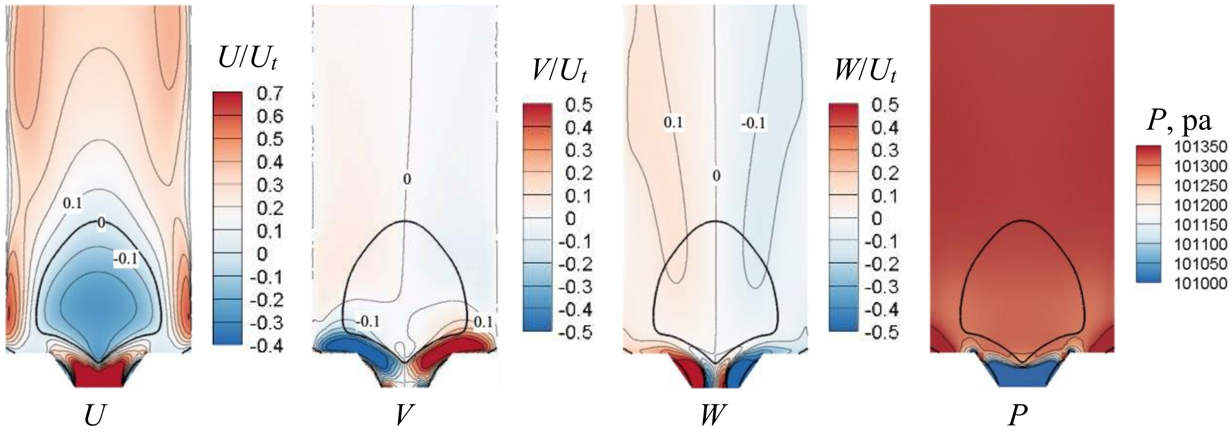

Figure 6-10. Contours of time-averaged axial (U), radial (V), and tangential (W) velocities and static pressure (P) on x-y plane from RANS prediction of LDI-60-CW, at ϕ=0.65. Bold black contours denote the boundary of recirculation zones (U=0).

The contours of time-averaged temperature and mass fractions of OH and CO are presented in Figures 6-11 and 12 for counter-swirling LES-FGM and RANS-FGM, respectively. In LES-FGM, the flame region reflected by these contours lies around the CRZ. The large high temperature region from flare exit towards downstream could lead to high NO_x production. Comparing the RANS-FGM results to OH* data and the LES-FGM results, RANS-FGM predicts incorrect flame pockets distributed along the wall downstream. Thus, RANS-FGM cannot capture the reaction region accurately in counter-swirling configuration.

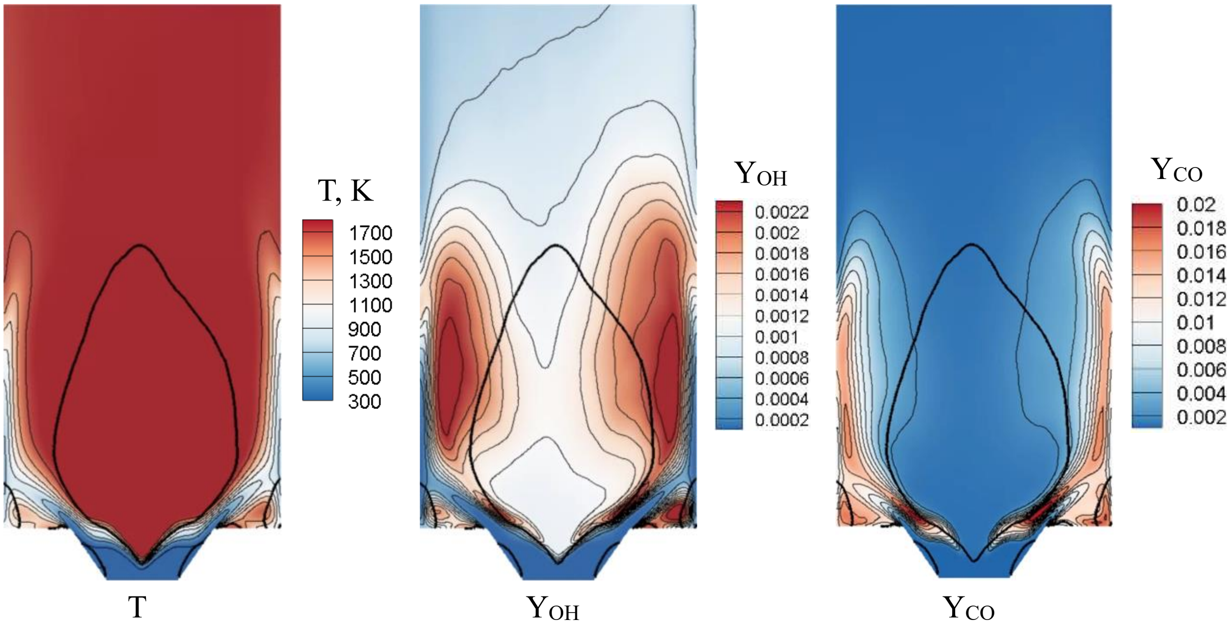

Figure 6-11. Contours of time-averaged temperature and mass fractions of OH and CO distributions on *x-y* plane from LES prediction of LDI-60-CW at ϕ=0.65. Bold black contours denote the boundary of recirculation zones (U=0).

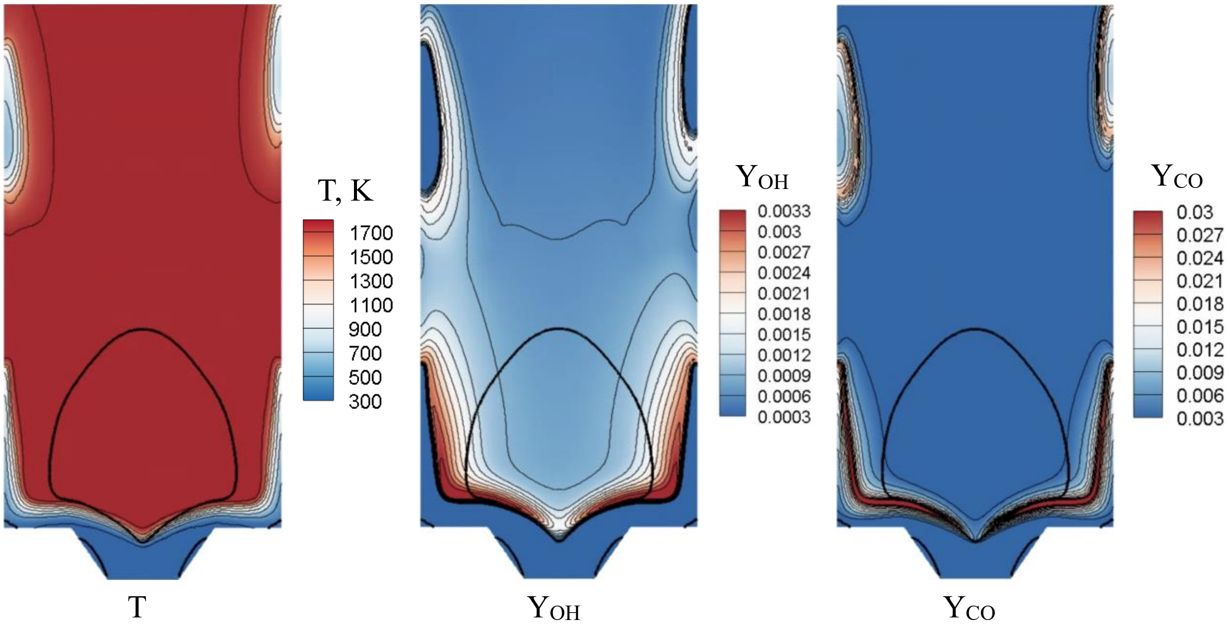

Figure 6-12. Contours of time-averaged temperature and mass fractions of OH and CO distributions on *x-y* plane from RANS prediction of LDI-60-CW at ϕ=0.65. Bold black contours denote the boundary of recirculation zones (U=0).

In summary, both RANS-FGM and LES-FGM can capture the CRZ flow pattern in reacting counter-swirling-flow of LDI. Compared to RANS-FGM, LES-FGM predicts the flow field more accurately and is able to capture the major flame pattern in LDI combustion. Especially, the line-of-sight OH distribution from LES matches well with the OH* chemiluminescence. Meanwhile, RANS-FGM does not simulate the flame region correctly.

6.3.2 Validation of LES-FGM on reacting co-swirling flow prediction

For the LDI-60-CCW configuration, the predictions of axial velocity and OH distribution from the LES-FGM case are compared against PIV and OH* chemiluminescence, respectively. CRZ is observed by both experiment and simulation as shown in Figure 6-13. However, from the time-averaged axial velocity distribution along the centerline (y=0) shown in Figure 6-14, the measured velocity becomes less negative downstream of the venturi exit, while the simulation predicts a local minimum velocity (the most negative) around $x/D_t = 2.6$. The discrepancy between simulated and measured axial velocity is as large as 0.25 U_t at $x/D_t = 1$. Detailed comparisons of time-averaged and RMS axial and radial velocities are plotted in Figures 6-11 and 12. Except for some variances near the flare exit, i.e. $x/D_t = 1$, co-swirling is predicted qualitatively by LES-FGM for mean and RMS velocities. The comparison of measured and LES-FGM predicted OH distributions is depicted in Figure 6-17. The distribution of OH mass fraction from LES-FGM largely captures the reaction region in terms of structure and flame location.

The LES-FGM model can qualitatively predict the flow and flame patterns in the counter- and co-swirling LDI configurations. Considering the unsatisfactory trend prediction of axial velocity trend along the centerline in co-swirling reacting flow, further analysis of reacting flow and flame response is investigated based on the counter-swirling case. It has to be pointed out that the inaccurate thermal boundary conditions [95] and limitations from FGM model influence the accuracy of velocity and species predictions [96].

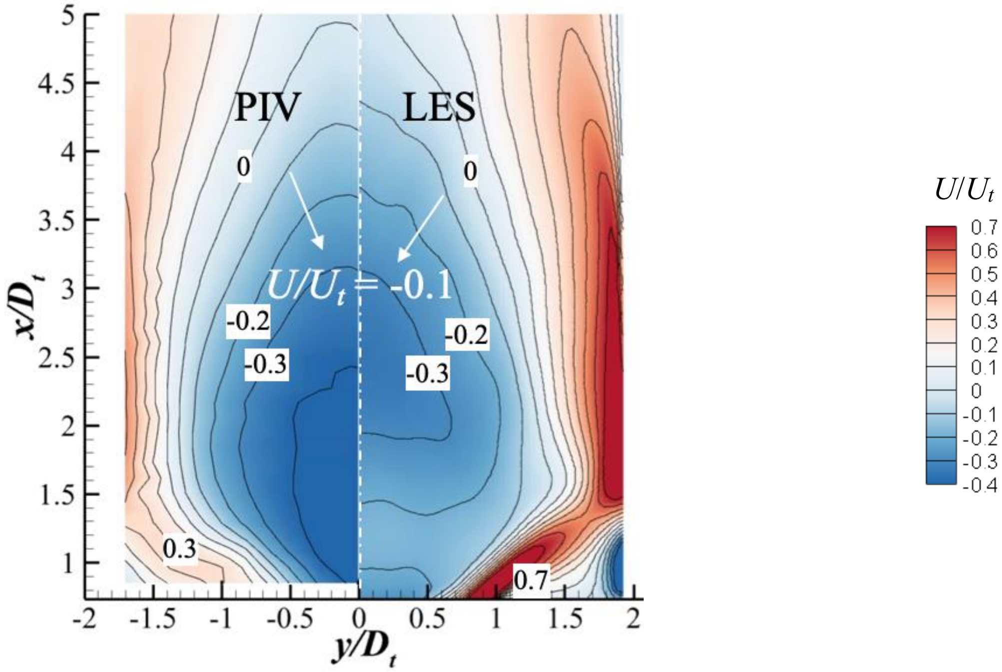

Figure 6-13. Comparison of time-averaged axial velocity between experimental data (PIV) and CFD prediction (LES) for reacting flow of LDI-60-CCW (co-swirling) at ϕ=0.65.

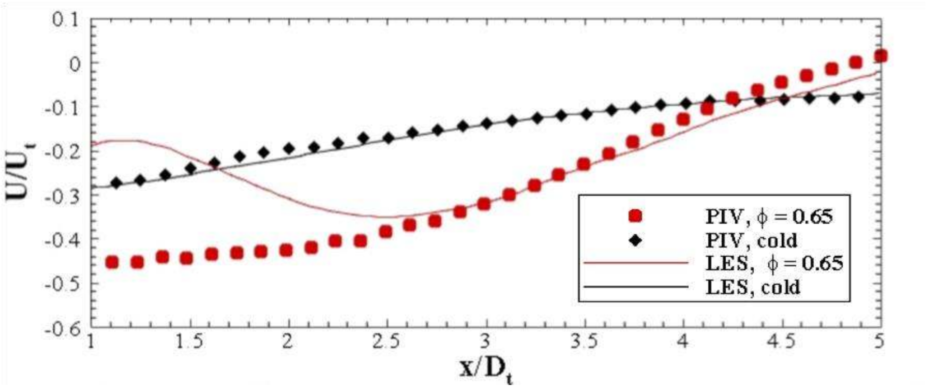

Figure 6-14. Time-averaged flow field comparison between experiments (PIV) and simulations (LES) in LDI-60-CCW (co-swirling).

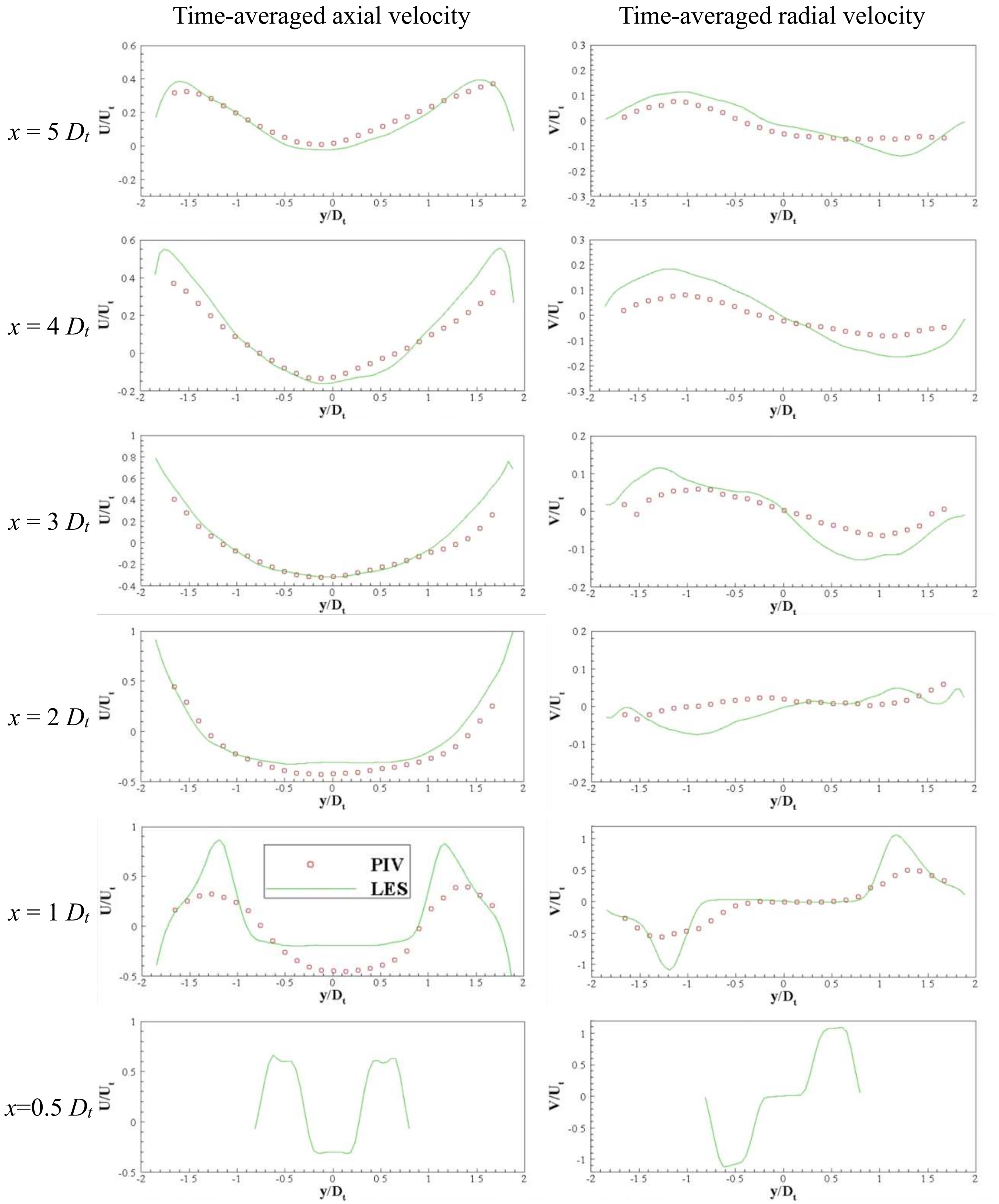

Figure 6-15. Measured (PIV), RANS-FGM, and LES-FGM predicted U (left) and V (right) profiles along radial direction at x = 0.5, 1, 2, 3, 4, and 5 D_t in LDI-60-CCW (co-swirling).

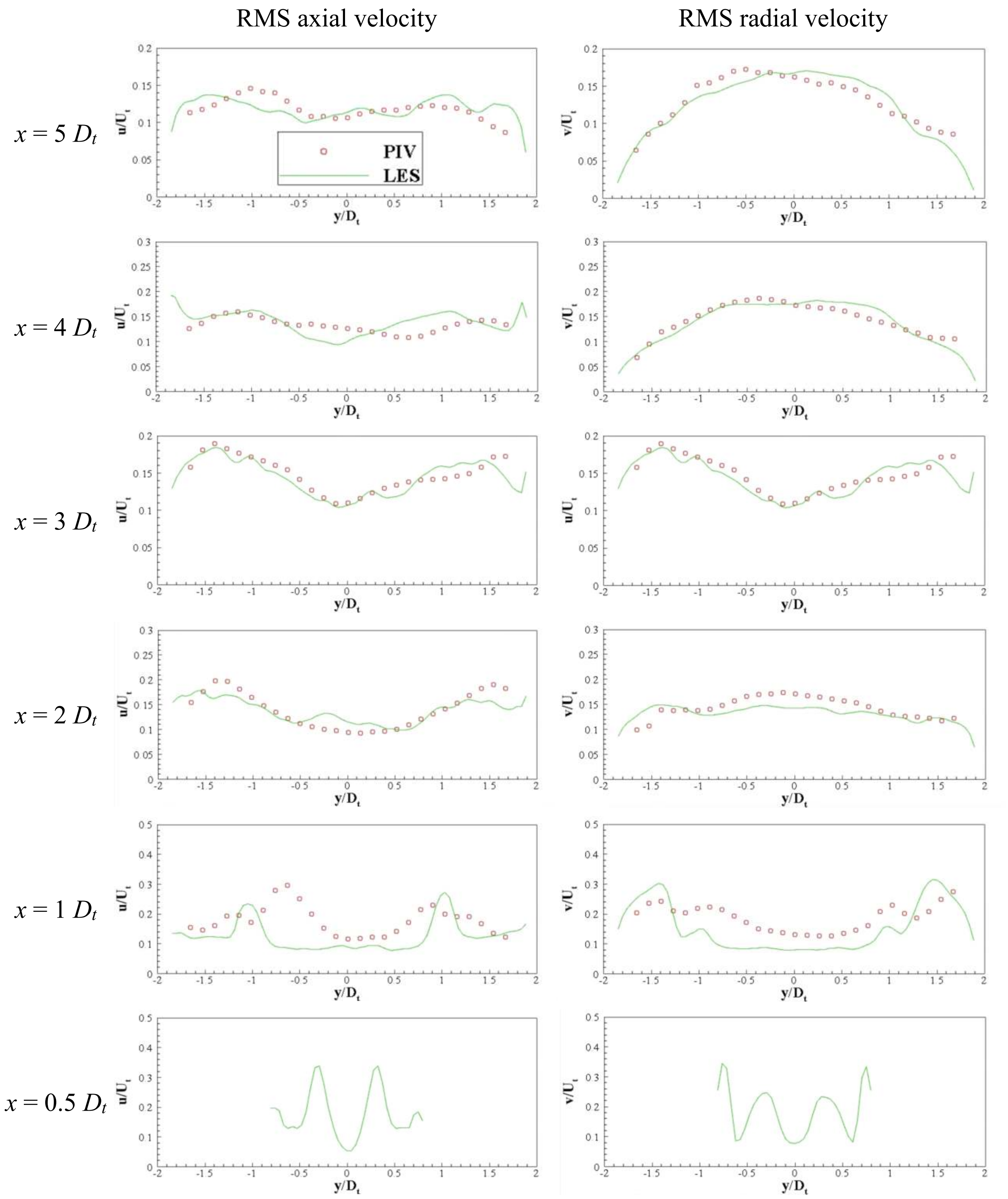

Figure 6-16. Measured (PIV) and LES-FGM predicted fluctuating axial and radial velocity profiles, *u* (left) and *v* (right), along radial direction at $x = 0.5$, 1, 2, 3, 4, and 5 D_t for LDI-60-CCW (co-swirling).

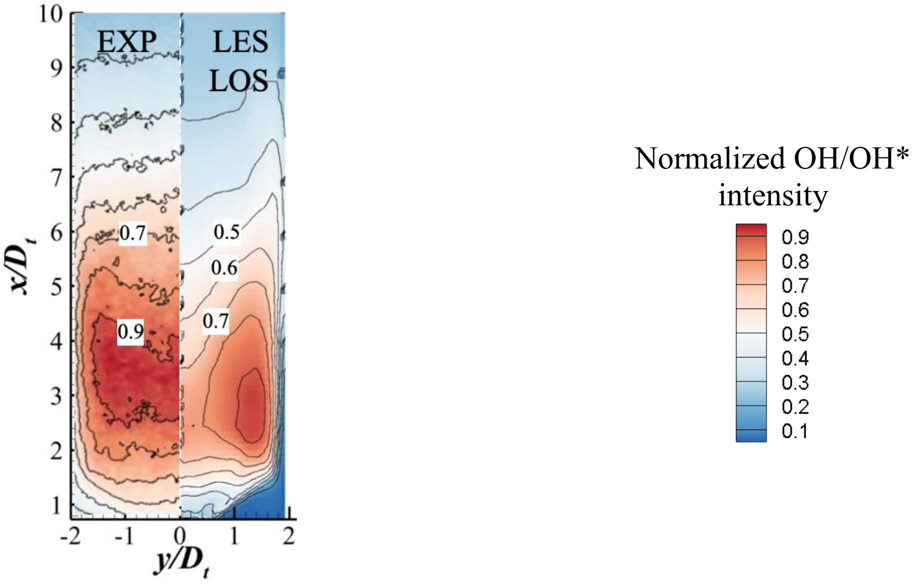

Figure 6-17. Reaction region represented by OH mass fraction and OH* chemiluminescence in LDI-60-CCW (co-swirling). Line-of-Sight averaged mass fraction of OH from LES (LES-LOS) is compared with OH* chemiluminescence measurement (EXP). To compare the results at the same locations, OH distribution on the right half is mirrored from the simulated values of the left half.

6.3.3 Flame structure analysis from LES-FGM results

Since the LES-FGM is able to qualitatively capture major flow and flame structures in the counter-swirling configuration, the flame structure is further analyzed with the information of instantaneous and time-averaged results from simulations. The instantaneous flame structure at ϕ=0.65 is depicted in Figure 6-18, which presents flame surface, and contours of temperature and mass fractions of species, including OH, CH_4, O_2, CO and CO_2, in the central *x*-*y* cut plane. To relate distributions of temperature and species, the right halves of *x*-*y* contours are actually mirrored from the left halves at the same time step. From the three-dimensional iso-surface of 1850 K, the LDI-60-CW configuration contains a complex turbulent flame. By using LES to sufficiently resolve turbulence vortices, the wrinkled flame surfaces of various sizes are revealed.

From the contours of instantaneous temperature distribution, the cold air and fuel streams, as indicated by the low temperature (~300K) region, come along the boundary of flare and penetrate in the chamber towards the side wall. With the confinement of chamber, a large part of cold fuel/air streams moves downstream along wall, and a small portion of cold streams fills the corner region. Combined with the OH mass fraction results, the combustion is intensive at the flare exit, where exist high OH mass fraction and steep temperature gradient. There also exists flame area in corner regions, which is much weaker compared to the flame region around the CRZ. As shown by the OH distribution, the combustion region is broader downstream, in the region between the CRZ and the side wall. From the contours of CH_4 mass fraction (Y_{CH4}), CH_4 is almost fully consumed or decomposed along the wall, while O_2 are excessive in the present globally lean combustion and exists beyond the flame front.

Taken the distributions of radicals and temperature together, it is found that CO largely exists at intermediate temperature range and OH exists mainly at high temperature range. The red pocket in the CO contours shows that flame continues into CRZ when the reaction is not intense enough, which could be the reason that the reaction becomes weaker and further extends into CRZ when the overall equivalence ratio is lower. The distributions of CH_4 and O_2 indicate that air and fuel streams are partially premixed before combustion, which in turn suggests that the diffusion-FGM model might needs some further modifications to predict LDI combustion more precisely.

The time-averaged axial (U), radial (V), and tangential (W) velocities, as well as the static pressure distributions in the *x-y* plane are presented in Figure 6-9. From the distributions of time-averaged axial velocities, it can be recognized that a vortex breakdown occurs near the exit of venturi, forming the CRZ. Between the CRZ and the high velocity streams of fresh air and fuel, a strong shear layer is generated, which is referred to as the inner shear layer (ISL). From the velocity streamtraces, it is demonstrated again that the CRZ helps to stabilize the flame near the flare exit by convecting the hot combustion products back and warming up the fresh mixture. Moreover, as indicated by the mean radial velocity, *V*, the CRZ acts as a cycling system that transfers the combustion products radially into downstream of the CRZ and carries the combustion products within CRZ towards the cold streams at the flare exit. In addition, the flow is highly swirling in the dome region, as shown by the time-averaged tangential velocity, *W*. The large magnitude of swirling velocity creates sufficient pressure drop along the chamber axial direction. Consistent with the previous report by Lefebvre [15], static pressure in the central core just downstream of the swirlers becomes low enough to create flow recirculation.

More detailed time-averaged flame structure is characterized by the mean temperature, OH, and CO distributions in Figure 6-11. As illustrated by these contours, there are three major reaction regions: between the side wall and the wings of the CRZ, ISL region and corner regions. In combination with the CH_4 and CO results, the cold air and CH_4 streams start to mix and react at the exit of the flare, where they are preheated by merging with the hot products from the CRZ reversed flow. Since the velocity is high and the strain rate is large around the ISL, the local oxidation reaction is incomplete as indicated by high concentration of CO and weak OH formation. Then the high velocity flow hits the chamber side wall (the location where static pressure is high in Figure 6-9) and splits into two parts. A major part continues to react downstream along the wings of CRZ; a minor part reverses to fill the chamber corners, and weak reaction continues there. In the region between the side wall and the wings of the CRZ boundary, the fuel is first partially oxidized into CO in the high velocity area. Then near the wings of the CRZ, as velocity magnitude reduces, intensive OH radicals are formed, indicating strong heat release. To summarize, from all the observations in reacting flow simulations, CRZ plays a significant role in stabilizing the flame and determining the flame intensity.

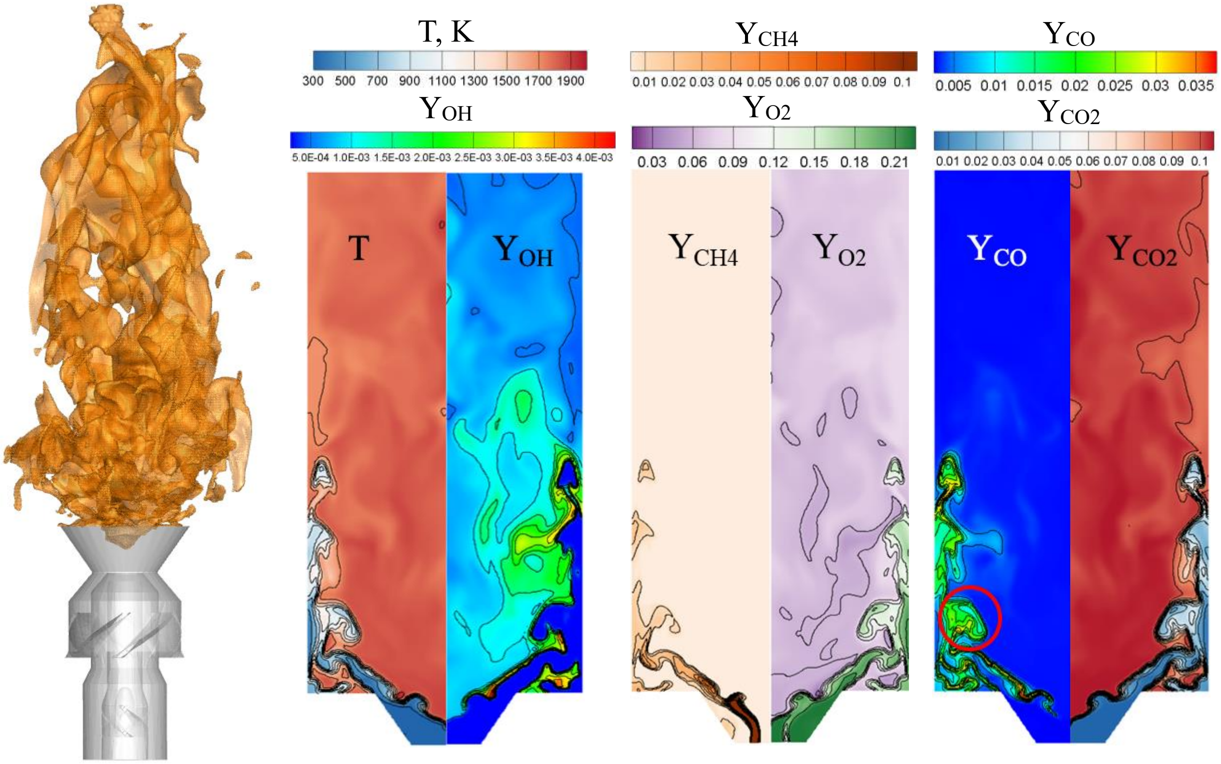

Figure 6-18. Instantaneous LES results on *x-y* plane of LDI-60-CW at ϕ=0.65. From left to right: flame surface (denoted by T=1850 K iso-surface), temperature (T), and mass fractions of OH, CH_4, O_2, CO, and CO_2.

6.3.4 Lift-off process by LES-FGM

From the present experimental investigations, the LDI-60-CW flames exhibit several different flame shapes when decreasing the overall equivalence ratio from high to low, as shown in Figure 6-19. In the view of the importance regarding the operability issue, the following discussion focuses on the life-off process, as demonstrated by the flame images changing from ϕ=0.65 to 0.62 in Figure 6-19. As the overall equivalence ratio decreases, the major flame region moves from CRZ-surrounding region to the center of the CRZ, then fully lifts off before LBO. Here the mechanisms behind the change of flame stabilization during the lift-off process are further explored with the LES predictions at two lower equivalence ratios, i.e. ϕ=0.55 and 0.45. The air mass flow rate is kept constant, but the fuel supply is reduced to decrease the overall equivalence ratio.

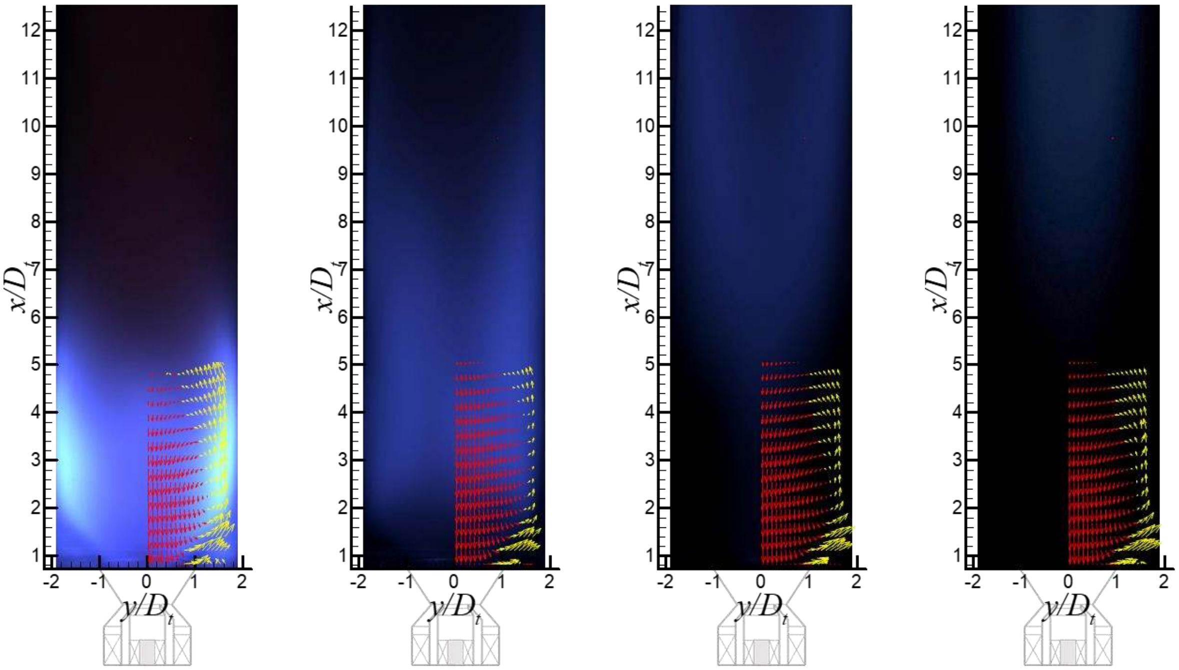

ϕ=0.85 ϕ=0.65 ϕ=0.62 ϕ=0.57

Figure 6-19. Flame structure variations at 3% pressure drop as approaching LBO for LDI-60-CW, represented by averaged direct flame images and mean U-V vector maps. Yellow vectors represent positive mean axial velocities, and red vectors show negative mean axial velocities.

The mean flame regions are indicated by the time-averaged temperature contours in Figure 6-20. Although the predictions did not capture the experimentally-observed flame structure variation when lowering ϕ from 0.65, the flame shape change is qualitatively demonstrated by the current LES-FGM modeling in that the flame boundary moves from the outer layer of the CRZ to the center of CRZ as ϕ decreases.

To decipher the mechanism of flame boundary moving into CRZ as equivalence ratio decreases, the instantaneous distribution of CH_4 and temperature at ϕ=0.45 are illustrated in Figure 6-21 with velocity streamtraces to visualize the flow motions. As the equivalence ratio reduces, the heat release is greatly reduced such that the local temperature is not high enough to consume all CH_4. Following the motions of vortices, unconsumed and partially-oxidized fuel proceed to react continuously into the CRZ region. Although local extinction cannot be predicted here, the present FGM method is still able to qualitatively illustrate the lift-off process in LDI combustion.

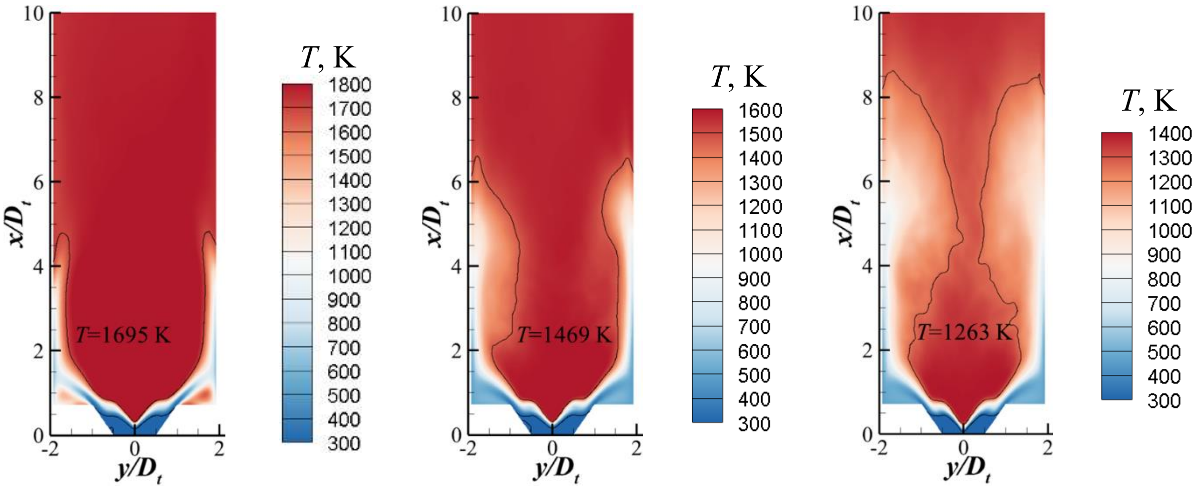

ϕ=0.65 ϕ=0.55 ϕ=0.45

Figure 6-20. Flame responses of LDI-60-CW indicated by time-averaged temperature contours on *x*-*y* plane, from LES predictions at ϕ=0.65, 0.55, and 0.45. Black line in each plot is the contour for T = 85% of maximum flame temperature in each case to outline the flame boundary.

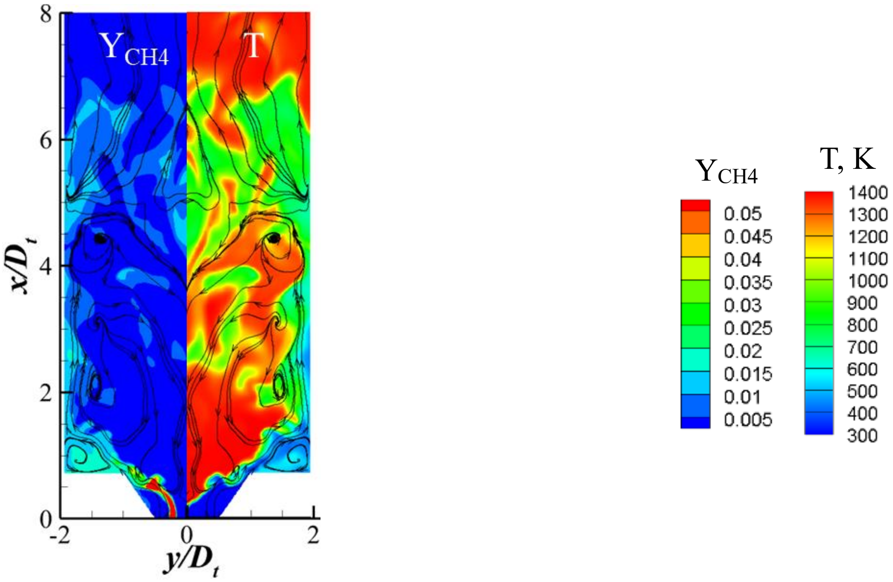

Figure 6-21. Instantaneous distributions of CH_4 mass fraction and temperature (mirrored from the left half results) in *x*-*y* plane from LES at ϕ=0.45, overlapped by streamtraces derived from instantaneous axial-radial velocities.

6.4 Concluding Remarks

The current chapter investigates adopting the FGM method to predict reacting flows in counter- and co-swirling LDI combustors. Validated by the experimental measurements of mean axial velocity and OH* chemiluminescence, LES-FGM is able to capture the major flow and flame patterns in both counter- and co-swirling reacting flows. Especially, the line-of-sight OH distribution from LES matches well with the OH* chemiluminescence data. Meanwhile, RANS-FGM does not simulate the correct flame region. Flame structure of LDI combustion is further analyzed with the simulated results of instantaneous and time-averaged flow, pressure, temperature, and radical distributions. CRZ is found to have significant impact on reversing hot products to cold streams and lowering local flow velocity to stabilize the flame and determine its location. Two additional LES-FGM cases at much lower overall equivalence ratios are investigated, demonstrating that LES-FGM is also able to illustrate the flame lift-off process. In summary, LES-FGM is able to capture basic characteristics of flow and flame in LDI combustion.

CHAPTER 7 SUMMARY AND FUTURE WORK

7.1 Summary

A systematic fundamental research effort has been carried out using advanced diagnostic techniques and state-of-the-art numerical simulation tools to provide insights into the impact of outer air swirler vane angle, flare geometry, and relative rotating direction of swirlers on the flow, flame, and emission characteristics of single-cup LDI combustion.

The outer air swirler vane angle has a direct effect on the swirl strength of LDI flow field. Two OAS vane angles, 60˚ and 45˚, have been experimentally tested for flow and flame fields, flame responses, LBO limits and NO_x emission levels. With a large vane angle (60˚), the increasing tangential velocity facilitates the vortex breakdown and creates a center recirculation zone in the dome region. The reversed flow from the CRZ promotes the flame stabilization near the swirler dump plate and assists the LDI-60-CW configuration in terms of lower LBO limits. With a small vane angle, the swirl strength is weak such that a swirling jet instead of a CRZ flow exists in the LDI-45-CW configuration. With swirling jet flow in LDI-45-CW, the flame is stabilized from the balance of flow velocity and flame propagation speed. The LBO limits in LDI-45-CW are observed to be higher than those of LDI-60-CW. Meanwhile, due to overall longer residence time with CRZ reversed flow, the NO_x emission level in LDI-60-CW is significantly higher than that in LDI-45-CW. Taken together, these observations suggest that a fundamental design tradeoff exists between low NO_x emissions and overall operability. As a result, optimization of the OAS vane angle is likely necessary to maintain sufficient swirl number to generate a CRZ for improved operability, while minimizing overall CRZ residence time for emissions reduction.

Flare is another important factor in LDI mixer design. The impact of the flare feature on LDI combustion has been experimentally investigated using two LDI mixers and two corresponding

Airblast mixers via flow and flame diagnostic techniques. The experimental results clearly demonstrate that removing the flare reduces swirl strength which in turn leads to the loss of a CRZ between the LDI-60-CW and Airblast-60-CW configurations, and increases the length of the swirling jet flow from the LDI-45-CW configuration to the Airblast-45-CW configuration. Moreover, reducing the swirl strength via either flare removal or OAS vane angle reduction for lifted cases tends to increase flame liftoff height, diffuse the reaction zone, and decrease the size and intensity of high temperature regions within the flametube. As a direct result, LBO limits are higher in the Airblast configurations than in the corresponding LDI counterparts, particularly for the 60˚ OAS cases where the configuration differences result in a transition from an anchored to lifted flame. Conversely, while reducing swirl strength has an adverse effect on LBO performance, flame liftoff height, and flame length, the more diffuse reaction zones and commensurately smaller high-temperature regions reduce the generation of NO_x. Taken as a whole, these results suggest that while the inclusion of a venturi flare serves as a method for increasing swirl strength which tends to improve operability, for a single swirler operability and NO_x emissions targets appear to be in inherent tension; reducing NO_x can be achieved by lowering swirl strength, but at the cost of LBO, flame liftoff height, and other operability metrics.

Furthermore, the influence of counter- and co-swirling flow on LDI performance is studied using experimental diagnostics and CFD simulations with the LDI-60-CW and LDI-60-CCW configurations. First, to establish the CFD best practice in LDI flow simulation, numerical setups including meshing and turbulence modeling are validated against measured flow data for iso-thermal flow simulations. The main flow structures in the LDI-60˚ OAS configurations include center and corner recirculation zones, which are successfully predicted by both RANS and LES models. LES can predict the effective area, the center recirculation zone size, and the time-averaged velocity distributions more accurately than RANS. A grid independence study is also conducted to identify adequate grids in LDI flow simulation. The resulting resolution of computation grids yields in a very high percentage of resolved turbulent kinetic energy, and hence the SGS model's impact is negligible in bulk flow simulation. Similarly, the performance of RANS and LES coupling with FGM is tested for LDI combustion simulations. Validated by the experimental measurements of axial velocity and OH* chemiluminescence, LES-FGM is able to capture the major flow and flame patterns in LDI combustion. Especially, the line-of-sight OH distribution from LES matches well with the OH* chemiluminescence data. Meanwhile, RANS-FGM does not simulate the correct flame region. Additionally, two LES-FGM cases at lower overall equivalence ratios are investigated, showing that LES-FGM is also able to describe the flame lift-off process.

With the present experimental and CFD results, the impact of relative direction between swirling flows on the characteristics of LDI flow and flame fields are also better understood. Due to the higher axial flux of tangential momentum, the co-swirling configuration, LDI-60-CCW, has greater swirl strength and creates a longer CRZ. On the other hand, the opposite direction between IAS and OAS swirling flows in LDI-60-CW creates an extra strong shear layer near the throat, facilitating fuel mixing in LDI combustion.

7.2 Future Work

The work presented in this dissertation illustrates the impact of design parameters on LDI combustion by using experimental measurements and CFD simulations. Future work regarding further improvement of the LDI performance of NO_x emissions and operability should focus on further optimization of the design parameters, such as using OAS vane angle between 45° and 60° with various flare expansion angles. In experimental measurements, utilizing an emission bench to measure combustion products at the combustor exit could help illustrate the influence of design parameters on LDI combustion efficiency and emission indices like $EINO_x$. Moreover, to capture the reacting flow more accurately, simulation utilizing the FGM model should take the condition of partially premixed combustion into account.

References

[1] B. Owen, D.S. Lee, L. Lim, Flying into the future: Aviation emissions scenarios to 2050, Environ. Sci. Technol. 44 (2010) pp. 2255-2260.

[2] Y.Z. Liu, X.X. Sun, V. Sethi, D. Nalianda, Y.G. Li, L. Wang, Review of modern low emissions combustion technologies for aero gas turbine engines, Prog. Aerosp. Sci. 94 (2017) pp. 12-45.

[3] G.D. Roy, Propulsion combustion: fuels to emissions, Taylor & Francis, 1998.

[4] H.S. Johnston, D.E. Kinnison, D.J. Wuebbles, Nitrogen oxides from high-altitude aircraft: an update of potential effects on ozone, J. Geophys. Res. 94 (1989) pp. 16351-16363.

[5] D.S. Lee, G. Pitari, V. Grewe, K. Gierens, J.E. Penner, A. Petzold, M.J. Prather, U. Schumann, A. Bais, T. Berntsen, D. Iachetti, Transport impacts on atmosphere and climate: Aviation, Atmos. Environ. 44 (2010) pp. 4678-4734.

[6] L. Li, Y. Lin, Z. Fu, C. Zhang, Emission characteristics of a model combustor for aero gas turbine application, Exp. Therm Fluid Sci. 72 (2016) pp. 235-248.

[7] ICAO. ICAO Environment Report 2010. 2010.

[8] ICAO. ICAO Environmental Report 2013. 2013.

[9] ICAO. Independent experts NO_x review and the establishment of medium and long term technology goals for NO_x. 2006.

[10] G. Poeschl, W. Ruhkamp, H. Pfost, Combustion with low pollutant emissions of liquid fuels in gas turbines by premixing and prevaporization, ASME 1994 Int. Gas Turbine Aeroengine Congr. Expo., The Hague, Netherlands, June 13-16, 1994, 94-GT-443.

[11] G. Leonard, J. Stegmaier, Development of an aeroderivative gas turbine dry low emissions combustion system, ASME 1993 Int. Gas Turbine Aeroengine Congr. Expo., Cincinnati, USA, May 24-27, 1993, 93-GT-288.

[12] M. Shehata, Emissions and wall temperatures for lean prevaporized premixed gas turbine combustor, Fuel 88 (2009) pp. 446-455.

[13] C. Allouis, F. Beretta, A. Amoresano, Experimental study of lean premixed prevaporized combustion fluctuations in a gas turbine burner, Combust. Sci. Technol. 180 (2008) pp. 900-909.

[14] D. Bernier, F. Lacas, S. Candel, Instability mechanisms in a premixed prevaporized combustor, J. Propuls. Power 20 (2004) pp. 648-656.

[15] A. H. Lefebvre, D. R. Ballal, Gas turbine combustion: alternative fuels and emissions. CRC press, 2010.

[16] R.G. McKinney, D. Sepulveda, W. Sowa, A.K. Cheung, The Pratt & Whitney TALON X low emissions combustor: revolutionary results with evolutionary technology, 45th AIAA Aerosp. Sci. Meet., Reno, USA, January 8-11, 2007, AIAA2007-386.

[17] N.K. Rizk, H.C. Mongia, Ultra-low NO_x rich-lean combustion. Proc. ASME 1990 Int. Gas Turbine Aeroengine Congr. Expo., Brussels, Belgium, June 11-14, 1990, 90-GT-87.

[18] N.K. Rizk, H.C. Mongia, Low NO_x rich-lean combustion concept application. 27th Jt. Propuls. Conf., Sacramento, USA, June 24-26, 1991, AIAA1991-1962.

[19] H.C. Mongia, Future trends in commercial aviation engines' combustion, Nov. Combust. Concepts Sustain. Energy Dev., Springer (2014) pp. 113-176.

[20] D.R. Reddy, C.M. Lee, An overview of low-emission combustion research at NASA Glenn, ASME Turbo Expo: Turbomachinery Technical Conference and Exposition, Seoul, Korea, June 13-17, 2016, GT2016-56100.

[21] S.K. Dhanuka, J.E. Temme, J.F. Driscoll, Lean-limit combustion instabilities of a lean premixed prevaporized gas turbine combustor, Proc. Combust. Inst. 33 (2011) pp. 2961-2966.

[22] J.E. Temme, P.M. Allison, J.F. Driscoll, Combustion instability of a lean premixed prevaporized gas turbine combustor studied using phase-averaged PIV, Combust. Flame 161 (2014) pp. 958-970.

[23] A. Amoresano, C. Allouis, M. Di Santo, P. Iodice, G. Quaremba, V. Niola, Experimental characterization of a pressure swirl spray by analyzing the half cone angle fluctuation, Exp. Therm. Fluid Sci. 94 (2018) pp. 122-133.

[24] S.K. Dhanuka, J.E. Temme, J.F. Driscoll, H.C. Mongia, Vortex-shedding and mixing layer effects on periodic flashback in a lean premixed prevaporized gas turbine combustor, Proc. Combust. Inst. 32 (2009) pp. 2901-2908.

[25] R. Smith, Advanced low emissions subsonic combustor study, NASA/CR−1998-207931.

[26] R. Tacina, Low NO_x potential of gas turbine engines, 28th Aerospace Sciences Meeting, Cleveland, USA, January 8-11, 1990, AIAA1990-550.

[27] R. Tacina, P. Lee, C. Wey, A lean-direct-injection combustor using a 9 point swirl-venturi fuel injector, ISABE, Munich, Germany, September 4-9, 2005, ISABE-2005-1106.

[28] R. Tacina, C. Wey, P. Laing, A. Mansour, A low NO_x lean-direct injection, multipoint integrated module combustor concept for advanced aircraft gas turbines, Conf. Technol. Combust. a Clean Environ., Oporto, Portugal, July 9-12, 2001, NASA/TM−2002-211347.

[29] R. Tacina, C. Wey, P. Laing, A. Mansour, Sector tests of a low-NOx, lean-direct-injection, multipoint intergrated module combustor concept, ASME 2002 Int. Gas Turbine Institute Turbo Expo., Amsterdam, Netherlands, June 3-6, 2002, GT2002-30089.

[30] K.M. Tacina, C. Chang, Z.J. He, P. Lee, H.C. Mongia, B.K. Dam, A second generation swirl-venturi lean direct injection combustion concept, 50th AIAA/ASME/SAE/ASEE Jt. Propuls. Conf., Cleveland, USA, AIAA2014-3434.

[31] K.M. Tacina, P. Lee, H. Mongia, B.K. Dam, Z.J. He, D.P. Podboy, A comparison of three second-generation swirl-venturi lean direct injection combustor concepts, 52nd AIAA/SAE/ASEE Jt. Propuls. Conf., Salt Lake City, USA, July 25-27, 2016, AIAA2016-4891.

[32] Y.R. Hicks, C.M. Heath, R.C. Anderson, K.M. Tacina, Investigations of a combustor using a 9-point swirl-venturi fuel injector: recent experimental results, ISABE, Goeteborg, Sweden, September 12-16, 2011, ISABE-2011-1106.

[33] K.M. Tacina, C.T. Chang, P. Lee, H. Mongia, D.P. Podboy, B.K. Dam, An assessment of combustion dynamics in a low-NO_x, second-generation swirl-venturi lean direct injection combustion concept, ISABE, Phoenix, USA, October 26-30, 2015, ISABE-2015-20249.

[34] Y. Fu, S.M. Jeng, R. Tacina, Characteristics of the swirling flow generated by an axial swirler, ASME Turbo Expo: Power for Land, Sea and Air, Reno, USA, June 6-9, 2005, GT2005-68728.

[35] J. Cai, S.M. Jeng, R. Tacina, The structure of a swirl-stabilized reacting spray issued from an axial swirler, 43rd AIAA Aerosp. Sci. Meet. Exhib., Reno, USA, January 10-13, 2005, AIAA2005-1424.

[36] R. Villalva-Gomez, E. Gutmark, A study of lean direct-injection flames through simultaneous PIV and OH* chemiluminescence, 49th AIAA Aerosp. Sci. Meet. New Horizons Forum Aerosp. Expo. Exhib., Orlando, USA, January 4-7, 2011, AIAA2011-516.

[37] R. Villalva-Gomez, B.J. Dolan, D.E. Munday, E.J. Gutmark, OH-PLIF studies in a LDI swirl-stabilized combustor, 52nd AIAA Aerosp. Sci. Meet., National Harbor, USA, January 13-17, 2014, AIAA2014-0656.

[38] J. Li, M. Hamza, A. Kumaran, U. Bhayaraju, S.M. Jeng, Study of development of a novel dual phase airblast injector for gas turbine combustor, ASME 2016 Turbo Expo., Seoul, Korea, June 13-17, 2016, GT2016-56340.

[39] T. Yi, D.A. Santavicca, Combustion instability in a turbulent liquid-fueled swirl-stabilized LDI combustor. 45th AIAA/ASME/SAE/ASEE Jt. Propuls. Conf. Exhib., Denver, USA, August 2-5, 2009, AIAA2009-5014.

[40] H.A. El-Asrag, A.C. Iannetti, S.V. Apte, Large eddy simulations for radiation-spray coupling for a lean direct injector combustor, Combust. Flame 161 (2014) pp. 510-524.

[41] J. Li, L. Yuan, H.C. Mongia, Simulation of combustion characteristics in a hydrogen fuelled lean single-element direct injection combustor, Int. J. Hydrogen Energy 42 (2017) pp. 3536-3548.

[42] N. Patel, M. Kirtaş, V. Sankaran, S. Menon, Simulation of spray combustion in a lean-direct injection combustor, Proc. Combust. Inst. 31 (2007) pp. 2327-2334.

[43] N. Patel, S. Menon, Simulation of spray-turbulence-flame interactions in a lean direct injection combustor, Combust. Flame 153 (2008) pp. 228-257.

[44] E. Kilik, Better swirl generation by using curved vane swirler, 23rd AIAA Aerosp. Sci. Meet., Reno, USA, January 14-17, 1985, AIAA1985-187.

[45] E. Kilik E, The influence of swirler design parameters on the aerodynamics of downstream recirculation region, Cranfield Institute of Technology, Ph.D. thesis, 1976.

[46] M.L. Mathur, N.R. Maccallu, Swirling air jets issuing from vane swirlers. 1. Free jets, J. Inst. Fuel 40 (1967) p. 214.

[47] X. Ren, C.J. Sung, H.C. Mongia, On lean direct injection research, in: A.K. Runchal, A.K. Gupta, A. Kushari, A. De, S.K. Aggarwal (eds.), Energy for propulsion: A sustainable technologies approach, Springer Singapore, Singapore, 2018, pp. 3-26.

[48] A. Melling A, Tracer particles and seeding for particle image velocimetry, Meas. Sci. Technol. 8 (1997) pp. 1406-1416.

[49] M.P. Wernet, A flow field investigation in the diffuser of a high-speed centrifugal compressor using digital particle imaging velocimetry, Meas. Sci. Technol. 7 (2000) pp. 1007-1022.

[50] R.W.B. Pearse, A.G. Gaydon, The identification of molecular spectra, 4th ed., Chapman and Hall, London, 1976.

[51] CONVERGE CFD. Software (Version 2.4. 0), Convergent Science. Inc, Middleton, WI 2017.

[52] P.K. Senecal, K.J. Richards, E. Pomraning, T. Yang, M.Z. Dai, R.M. McDavid, M.A. Patterson, A new parallel cut-cell Cartesian CFD code for rapid grid generation applied to in-cylinder diesel engine simulations, SAE Technical Paper, 2007-01-0159.

[53] B.E. Launder, D.B. Spalding, Lectures in mathematical models of turbulence, 1972.

[54] G. Hsiao, H. Mongia, Swirl Cup Modeling Part 3: Grid independent solution with different turbulence models, 41st AIAA Aerosp. Sci. Meet. Exhib., Reno, USA, January 6-9, AIAA2003-1349.

[55] D.K. Lilly, A proposed modification of the Germano subgrid-scale closure method, Phys. Fluids A Fluid Dyn. 4 (1992) pp. 633-635.

[56] M. Germano, U. Piomelli, P. Moin, W.H. Cabot, A dynamic subgrid-scale eddy viscosity model, Phys. Fluids A Fluid Dyn. 3 (1991) pp. 1760-1765.

[57] C. Meneveau C, Statistics of turbulence subgrid-scale stresses: necessary conditions and experimental tests, Phys. Fluids 6 (1994) pp. 815-833.

[58] E. Pomraning, Development of large eddy simulation turbulence models, University of Wisconsin--Madison, Ph.D. thesis, 2000.

[59] B.E. Launder, D.B. Spalding, The numerical computation of turbulent flows, Comput. Methods Appl. Mech. Eng. 3 (1974) pp. 269-289.

[60] H. Werner, H. Wengle, Large-eddy simulation of turbulent flow over and around a cube in a plate channel, In: Durst F., Friedrich R., Launder B.E., Schmidt F.W., Schumann U. WJH, editor. Turbul. Shear Flows, Springer, Berlin, Heidelberg, 1993, pp. 155-168.

[61] L.P.H. De Goey, J.H.M. ten Thije Boonkkamp, A flamelet description of premixed laminar flames and the relation with flame stretch, Combust. Flame 119 (1999) pp. 253-271.

[62] G.P. Smith, D.M. Golden, M. Frenklach, N.W. Moriarty, B. Eiteneer, M. Goldenberg, et al, GRI-MECH 3.0 1999, http://www.me.berkeley.edu/gri_mech/.

[63] R.I. Issa, Solution of the implicitly discretised fluid flow equations by operator-splitting, J. Comput. Phys. 62 (1986) pp. 40-65.

[64] H.S. Alkabie HS, G.E. Andrews, AS, ASME 1991 Turbo Expo., Orlando, USA, June 3-6, 1991, 91-GT-363.

[65] R.T.K. Raj, Ganesan V. Study on the effect of various parameters on flow development behind vane swirlers, Int. J. Therm. Sci. 47 (2008) pp. 1204-1225.

[66] S.H. Pourhoseini, R. Asadi, An experimental study of optimum angle of air swirler vanes in liquid fuel burners, J. Energy Resour. Technol. 139 (2017) pp. 032202-032206.

[67] B. Wang, C. Zhang, Y. Lin, X. Hui, J. Li, Influence of main swirler vane angle on the ignition performance of Teless-II combustor, J. Eng. Gas Turbines Power 139 (2017) pp. 011501-011508.

[68] L.Y.M. Gicquel, G. Staffelbach, T. Poinsot, Large eddy simulations of gaseous flames in gas turbine combustion chambers, Prog. Energy Combust. Sci. 6 (2012) pp. 782-817.

[69] S.M. Johnson, Venturi nozzle effects on fuel drop size and nitrogen oxide emissions, NASA Rep., 1982, NASA-TP-2028.

[70] K.S. Im, M.C. Lai, R. Tacina, A parametric spray study of the swirler/venturi injectors, 34th AIAA/ASME/SAE/ASEE Jt. Propuls. Conf. Exhib., Cleveland, USA, July 13-15, 1998, AIAA1998-3269.

[71] X. Wang, Y. Lin, H. Hu, C. Zhang, Y. Kang, Effect of swirl cup's venturi shape on spray structure and ignition process, ASME Turbo Expo 2014 Turbine Tech. Conf. Expo., Dusseldorf, Germany, June 16-20, 2014, GT2014-25216.

[72] H.Y. Wang, V.G. McDonell, S. Samuelsen, Influence of hardware design on the flow field structures and the patterns of droplet dispersion: part I — mean quantities, J. Eng. Gas Turbines Power 117 (1995) pp. 282-289.

[73] W. Estefanos, S. Tambe, S.M. Jeng, Effect of the flare expansion angle on the mean and dynamic behavior of swirling flow generated by a counter rotating radial-radial swirler using a water test rig, ASME Turbo Expo 2015 Turbine Tech. Conf. Expo., Montreal, Canada, June 15-19, 2015, GT2015-43470.

[74] Y. Huang, V. Yang, Dynamics and stability of lean-premixed swirl-stabilized combustion, Prog. Energy Combust. Sci. 35 (2009) pp. 293-364.

[75] H.C. Mongia, T.J. Held, G.C. Hsiao, R.P. Pandalai, Incorporation of combustion instability issues into design process: GE aeroderivative and aero engines experience, Combust. Instab. Gas Turbine Engines Oper. Exp. Fundam. Mech. Model., AIAA, 2005, pp. 43-63.

[76] J.B. Sewell, P.A. Sobieski, Monitoring of combustion instabilities: Calpine's experience, Combust. Instab. Gas Turbine Engines Oper. Exp. Fundam. Mech. Model. 210 (2005) pp. 147-162.

[77] I. Boxx, M. Stöhr, C. Carter, W. Meier, Temporally resolved planar measurements of transient phenomena in a partially pre-mixed swirl flame in a gas turbine model combustor, Combust. Flame 157 (2010) pp. 1510-1525.

[78] T. Yi, D.A. Santavicca, Forced flame response of turbulent liquid-fueled lean-direct-injection combustion to fuel modulations, J. Propuls. Power 25 (2009) pp. 1259-1271.

[79] D.J. Tritton, Physical fluid dynamics, Springer Science & Business Media, 2012.

[80] N.K. Singh, K. Ramamurthi, Formation of Coanda jet from sharp-edged swirl nozzle with base plate, Exp. Therm. Fluid Sci. 33 (2009) pp. 675-682.

[81] N. Syred, J.M. Beer, Combustion in swirling flows: a review, Combust, Flame 23 (1974) pp. 143-201.

[82] A.K. Gupta, D.G. Lilley, N. Syred, Swirl flows, Abacus Press, 1984.

[83] K. Ajmani, H.C. Mongia, P. Lee, Assessment of CFD approaches for next-generation combustor design. ASME 2014 Gas Turbine India Conf., New Delhi, India, December 15-17, 2014, GTINDIA2014-8361.

[84] K. Ajmani, H. Mongia, P. Lee, CFD computations of emissions for LDI-2 combustors with simplex and airblast injectors, 50th AIAA/ASME/SAE/ASEE Jt. Propuls. Conf., Cleveland, USA, July 28-30, 2014, AIAA2014-3529.

[85] S.B. Pope, Turbulent flows, Cambridge University Press, 2001.

[86] K. Ajmani, H. Mongia, P. Lee, CFD evaluation of a 3rd generation LDI combustor, 53rd AIAA/SAE/ASEE Jt. Propuls. Conf., Atlanta, USA, July 10-12, 2017, AIAA2017-5017.

[87] Y. Huang, V. Yang, Effect of swirl on combustion dynamics in a lean-premixed swirl-stabilized combustor, Proc. Combust. Inst. 30 (2005) pp. 1775-1782.

[88] J.A. van Oijen, L.P.H. de Goey, Modelling of premixed laminar flames using flamelet-generated manifolds, Combust. Sci. Technol. 161 (2000) pp. 113-137.

[89] N. Peters, G. Paczko, R. Seiser, K. Seshadri, Temperature cross-over and non-thermal runaway at two-stage ignition of n-heptane, Combust. Flame 128 (2002) pp. 38-59.

[90] A. Donini, R.J.M. Bastiaans, J.A. van Oijen, L.P.H. de Goey, A 5-D implementation of FGM for the large eddy simulation of a stratified swirled flame with heat loss in a gas turbine combustor, Flow, Turbul. Combust. 98 (2017) pp. 887-922.

[91] M. Ihme, L. Shunn, J. Zhang, Regularization of reaction progress variable for application to flamelet-based combustion models, J. Comput. Phys. 23 (2012) pp. 7715-7721.

[92] A. Donini, S.M. Martin, R.J.M. Bastiaans, J.A. van Oijen, L.P.H. de Goey, Numerical simulations of a premixed turbulent confined jet flame using the flamelet generated manifold approach with heat loss inclusion, ASME Turbo Expo 2013 Turbine Tech. Conf. Expo., San Antonio, USA, June 3-7, 2013, GT2013-94363.

[93] B.D. Stojkovic, T. D. Fansler, M.C. Drake, V. Sick, High-speed imaging of OH* and soot temperature and concentration in a stratified-charge direct-injection gasoline engine, Proc. Combust. Inst. 30 (2005) pp. 2657-2665.

[94] V.N. Nori, Modeling and analysis of chemiluminescence sensing for syngas, methane and Jet-A combustion, Georgia Institute of Technology, Ph.D. thesis, 2008.

[95] R. Mercier, T.F. Guiberti, A. Chatelier, D. Durox, O. Gicquel, N. Darabiha, T. Schuller, B. Fiorina, Experimental and numerical investigation of the influence of thermal boundary conditions on premixed swirling flame stabilization, Combust. Flame 171 (2016) pp. 42-58.

[96] P.D. Nguyen, L. Vervisch, V. Subramanian, P. Domingo, Multidimensional flamelet-generated manifolds for partially premixed combustion, Combust. Flame 157 (2010) pp. 43-61.